

REPORT DOCUMENTATION PAGE			Form Approved OMB No. 0704-0188	
Public reporting burden for this collection of information is estimated to average 1 hour per response, including the time for reviewing instructions, searching existing data sources, gathering and maintaining the data needed, and completing and reviewing the collection of information. Send comments regarding this burden estimate or any other aspect of this collection of information, including suggestions for reducing this burden, to Washington Headquarters Services, Directorate for Information Operations and Reports, 1215 Jefferson Davis Highway, Suite 1204, Arlington, VA 22202-4302, and to the Office of Management and Budget, Paperwork Reduction Project (0704-0188), Washington, DC 20503.				
1. AGENCY USE ONLY (Leave blank)		2. REPORT DATE 30 December 1998	3. REPORT TYPE AND DATES COVERED FINAL ⁰¹ March 1997 - 31 August 2000	
4. TITLE AND SUBTITLE Phonons on Quantum Epitaxial Structures Based on Wide Band Gap Materials			5. FUNDING NUMBERS DAAH04-93-D-0003	
6. AUTHOR(S) Mitra Dutta				
7. PERFORMING ORGANIZATION NAME(S) AND ADDRESS(ES) North Carolina State University, Raleigh, NC 27695-8202			8. PERFORMING ORGANIZATION REPORT NUMBER	
9. SPONSORING/MONITORING AGENCY NAME(S) AND ADDRESS(ES) U. S. Army Research Office P. O. Box 12211 Research Triangle Park, NC 27709-2211			10. SPONSORING/MONITORING AGENCY REPORT NUMBER ARO 37205-EL -2-	
11. SUPPLEMENTARY NOTES The views, opinions and/or finding contained in this report are those of the author(s) and should not be construed as an official Department of Army position, policy of decision, unless so designated buy other documentation.				
12a. DISTRIBUTION AVAILABILITY STATEMENT Approved for public release; distribution unlimited.			12b. DISTRIBUTION CODE	
13. ABSTRACT (Maximum 200 words) Raman scattering studies were performed on III-V Nitride materials including binary crystals, ternary alloys, and superlattices of GaN/AlN and GaN/AlGaIn. Our results show that in AlGaIn alloys the asymmetric behavior of the E2 lineshape arises from random disorder; the E2 phonon does not follow a one mode behavior and the AlGaIn films on SiC are under small tensile stress. In the InGaIn too the A1 mode shows a one mode behavior while two mode behavior may be possible for E2. Possible mode mixing takes place. Evidence of inhomogeneities and spinodal decomposition is seen in these films. Phonon lifetime measurements are made in the binary crystals and in every case we see evidence of two lifetime regions. In the superlattices we see anomalous low temperature behavior that is consistent with a density of states of spectral distribution that is due to the roughness of the interfaces and which agrees with TEM measurements. Finally preliminary measurements demonstrate strong interface phonons in the GaN/AlN superlattices which give good agreement with theory.				
14. SUBJECT TERMS Wide band gap semiconductors, phonons and their lifetimes.			15. NUMBER OF PAGES 162	
			16. PRICE CODE	
17. SECURITY CLASSIFICATION OF REPORT UNCLASSIFIED	18. SECURITY CLASSIFICATION OF THIS PAGE UNCLASSIFIED	19. SECURITY CLASSIFICATION OF ABSTRACT UNCLASSIFIED	20. LIMITATION OF ABSTRACT UL	

Table of Contents

- i) Preface
- 1) List of Publications
- 2) Photoluminescence and recombination mechanisms in GaN/Al_{0.2}Ga_{0.8}N superlattice
- 3) Raman Analysis of the Configurational Disorder in Al_xGa_{1-x}N films
- 4) UV Raman Study of A₁(LO) and E₂ Phonons in In_xGa_{1-x}N Alloys
- 5) Raman Analysis of the E₁ and A₁ Quasi-LO and -TO Modes in Wurtzite AlN
- 6) Raman Analysis of Phonon Lifetimes in AlN and GaN of Wurtzite Structure
- 7) Raman Scattering Spectroscopy and Analysis of III-V Nitride-Based Materials

20010412 087

Phonons on Quantum Epitaxial Structures Based on Wide Band Gap Materials

Preface

Raman scattering studies were performed on III-V Nitride materials including binary crystals, ternary alloys, and superlattices of GaN/AlN and GaN/AlGaN. Our results show that in AlGaN alloys the asymmetric behavior of the E2 lineshape arises from random disorder; the E2 phonon does not follow a one mode behavior and the AlGaN films on SiC are under small tensile stress. In the InGaN too the A1 mode shows a one mode behavior while two mode behavior may be possible for E2. Possible mode mixing takes place. Evidence of inhomogeneities and spinodal decomposition is seen in these films. Phonon lifetime measurements are made in the binary crystals and in every case we see evidence of two lifetime regions. In the superlattices we see anomalous low temperature behavior that is consistent with a density of states of spectral distribution that is due to the roughness of the interfaces and which agrees with TEM measurements. Finally preliminary measurements demonstrate strong interface phonons in the GaN/AlN superlattices which give good agreement with theory.

Publications

1. "Raman Analysis of the Configurational Disorder in $\text{Al}_x\text{Ga}_{1-x}\text{N}$ films," Leah Bergman, Michael D. Bremser, William G. Perry, Robert F. Davis, Mitra Dutta and Robert J. Nemanich. *Appl. Phys. Lett.* **71**, (15), 2157-2159 (1997).
2. "Raman Analysis of $\text{Al}_x\text{Ga}_{1-x}\text{N}$ Films," Leah Bergman, Mitra Dutta, Michael D. Bremser, Ok-Hyun Nam, William G. Perry, Dimitri Alexson, Robert F. Davis, Cengiz M. Balkas and Robert J. Nemanich. *Nitride Semiconductors*, edited by F. A. Ponce, S. P. DenBaars, B. K. Meyer, S. Nakamura and S. Strite. (Mater. Res. Soc. Symp. Proc., Vol. **482**, Boston, Massachusetts) p. 543-548.
3. "Raman Analysis of the E1 and A1 Quasi-LO and -TO Modes in Wurtzite AlN," Leah Bergman, Mitra Dutta, Cengiz Balkas, Robert F. Davis, James A. Christman, Dimitir Alexson and R. J. Nemanich, *J. Appl. Phys* **85**, (7), 3535-3539 (1999).
4. "Confined phonons and phonon-mode properties of III-V nitrides with wurtzite crystal structure," D. Alexson, Leah Bergman, Mitra Dutta, K. W. Kim, S. Komirenko, Robert J. Nemanich, B. C. Lee, Michael A. Stroscio, and SeGi Yu. *Physica B* 263-264, 510-513, (1999).
5. "Raman Analysis of Phonon Lifetimes in AlN and GaN of Wurtzite Structure," Leah Bergman, Dimitri Alexson, Patrick L. Murphy, Mitra Dutta, Michael A. Stroscio, Cengiz Balkas, Hyumin Shin, Robert F. Davis and Robert J. Nemanich. *Phys. Rev. B*, **59**, (20), p. 12977-12982 (1999).
6. "Phonon Dynamics and Lifetimes of AlN GAN Crystallites," Leah Bergman, Dimitir Alexson, Robert J. Nemanich, Mitra Dutta, Michael A. Stroscio, Cengiz Balkas and Robert F. Davis. *GaN and Related Alloys*, edited by Stephen J. Pearton, Chihping Kuo, Alan F. Wright and Takeshi Uenoyama (Mat. Res. Soc. Symp Proc. Vol. **537**, Spring, San Francisco, CA) p G 6.65, (1999).
7. "Photoluminescence and recombination mechanisms in $\text{GaN}/\text{Al}_{0.2}\text{Ga}_{0.8}\text{N}$ superlattice," Leah Bergman, Mitra Dutta, M. A. Stroscio, S. M. Komirenko, C. J. Eiting, D. J. H. Lambert, H. K. Kwon, R. D. Dupuis and R. J. Nemanich. *Appl. Phys Lett.* **76** (15) 1969-1971, (2000).
8. "UV Raman Study of $A_1(\text{LO})$ and E_2 Phonons in $\text{In}_x\text{Ga}_{1-x}\text{N}$ Alloys," Dimitri Alexson, Leah Bergman, Mitra Dutta, Michael A. Stroscio, C. A. Parker, S. M. Bedair, N. A. El-Masry, Fran Adar and R. J. Nemanich. Submitted to *J. Appl. Phys.*, 2000.
9. "Raman Scattering Spectroscopy and Analysis of III-V Nitride-Based Materials," Leah Bergman, Mitra Dutta and Robert J. Nemanich. Edited by W. Weber and R. Merlin. To be published in Springer, 2000.

PHOTOLUMINESCENCE AND RECOMBINATION MECHANISMS IN GaN/Al_{0.2}Ga_{0.8}N SUPERLATTICE

Leah Bergman⁽¹⁾, Mitra Dutta⁽²⁾, M.A. Stroscio⁽²⁾, S.M. Komirenko⁽³⁾, Robert J. Nemanich⁽¹⁾, C. J. Eiting⁽⁴⁾, D. J. H. Lambert⁽⁴⁾, H. K. Kwon⁽⁴⁾, and R. D. Dupuis⁽⁴⁾

1) Department of Physics, North Carolina State University, Raleigh, North Carolina 27695-8202

*2) U.S. Army Research Office, P.O. Box 12211, Research Triangle Park, North Carolina
27709-2211*

*3) Department of Electrical and Computer Engineering, North Carolina State University, Raleigh
North Carolina 27695-7911*

*4) The University of Texas at Austin, Microelectronics Research Center, Austin, Texas
78721-1100*

ABSTRACT

A detailed study of photoluminescence (PL) of GaN(1nm)/Al₂₀Ga₈₀N(3.3nm) twenty periods superlattice grown via metalorganic chemical vapor deposition is presented. The dependence of the PL emission energy, linewidth, and intensity on temperature, in the low temperature regime, is consistent with recombination mechanisms involving bandtail states attributed to a small degree of interfacial disorder. The activation energy of the non-radiative centers in our superlattice agrees well with the value we derive for the width of the tail-state distribution. Moreover, we find that the average phonon energy of the phonons that control the interband PL energy at high temperatures is larger for the superlattice than for a high quality GaN film. This observation is consistent with model calculations predicting the phonon mode properties of GaN-AlN – based wurtzite heterostructures.

Anomalous temperature dependence of the photoluminescence (PL) emission energy from InGaN quantum wells that does not follow at low temperatures, the accepted Varshni [1] or Bose-Einstein [2-3] type behavior of a semiconductor band-gap has been reported [4]. Such behavior has been observed as well in quantum wells and superlattices of the zincblende structure [5-8]. The PL energy, instead of being approximately constant at low temperatures, exhibits a red shift followed by a blue shift. In the above studies the anomalous dependence was attributed to the effect of the interface defect density of states (DOS), on the PL energy.

The presence of defect density in an heterostructure device is crucial to the device performance, especially in structures where multiple interfaces exist. In this letter, we present a detailed study of the photoluminescence from a GaN/Al_{0.2}Ga_{0.8}N superlattice of wurtzite structure. We establish the presence of a defect density of states, which controls the PL energy at low temperatures and acts as a non-radiative channel to the PL at higher temperatures. Moreover, the electron-phonon interaction that affects the PL at higher temperatures is stronger in the superlattice than in a GaN film indicating the contributions of phonons of higher energies.

The luminescence measurements were acquired utilizing the 244 nm (5.08 eV) line from the second harmonic generation of the 488 nm line of Ar ion Coherent laser and the Tripletmate ISA monochromator in conjunction with a liquid nitrogen-cooled CCD detector. The cold stage consists of a closed-cycle cryostat, which enables measurements from 10K up to room temperature. The superlattice consists of twenty periods of (1nm)GaN/(3.3nm)Al_{0.2}Ga_{0.8}N grown on 2 μ m GaN with a 25nm GaN buffer layer on a (0001) sapphire substrate. The nitride materials described in this work are grown by metalorganic chemical vapor deposition (MOCVD) in an EMCORE D125 UTM rotating-disk reactor. The growth temperature is \sim 1050 $^{\circ}$ C for the thick undoped GaN layer and the Al_{0.2}Ga_{0.8}N superlattice layers.

In the following we present our study focusing on the photoluminescence behavior as a function of temperature of the GaN/Al_{0.2}Ga_{0.8}N superlattice. Figure 1 depicts the PL spectrum of the SL acquired at 10K. The peak at 3.795 eV with a full width at half maximum of 32 meV is attributed to the PL emission from the GaN wells. The additional PL peaks observed in the spectrum are at \sim 3.488 eV, due to excitonic emission of the underlying GaN buffer layer, as well as a weak peak at \sim 3.7 eV, the origin of which will be addressed in a later study. The inset to Figure 1 depicts the intensity of the luminescence from the superlattice as a function of excitation intensity at 10 K. A linear relation between the two intensities was ascertained which

is indicative that the PL emission of the SL at 10 K is due to excitonic recombination [9]. Figure 2 shows the luminescence peak position as a function of temperature of the superlattice compared to that of a high quality GaN thin film. The inset in fig. 2 plots the PL linewidths of from the superlattice sample.

It has been established that the temperature dependence of an interband transition energy, $E(T)$, in semiconductors can be approximated via the relation [2-3, 10-12]:

$$E(T) = E(0) - \frac{2\alpha}{\exp(\Theta/T) - 1} \quad (1)$$

This relation represents the modification of a band-gap of a semiconductor due to the electron-phonon interaction at thermal equilibrium, and may be derived from the Bose-Einstein approximation for the lattice vibration energy: $\langle E \rangle = (1/2 + \langle n \rangle) \hbar \omega$ where $\langle n \rangle$ is the average phonon occupation number [12]. In Equation 1, $E(0)$ is the transition energy at 0 K, α is a measure of the strength of the electron-average phonon interaction, and Θ corresponds to a mean temperature value of the longitudinal acoustic as well as of optical phonons taking place in the interaction [2-3, 10-12]. The average phonon temperature Θ is related to the average phonon energy E_P via the Boltzmann constant k_B : $\Theta = E_P / k_B$. The model presented in Equation (1) exhibits a good fit to our PL experimental data of the GaN film, as can be seen in Figure 2. The fit resulted in the following values: $E(0)=3.4866$ eV, $\alpha=55$ meV, and $\Theta=309$ K and thus $E_P=27$ meV. These values agree with the ones obtained previously for GaN films via the same model utilizing optical absorption [13] and contactless electoreflectance [10].

As can be observed in Figure 2 the temperature dependence of the PL emission of the GaN/Al_{0.2}Ga_{0.8}N superlattice does not follow the monotonic variation of Equation 1 for the band edge to lower energies with increasing temperature. Similar behavior has previously been observed in the quantum well structures of AlGaIn/InGaIn/GaN [4], InGaAs-InP [5], and GaInAs/AlInAs [6] as well as in superlattices of ZnSe/MgS [7] and GaAs/AlAs [8]. This anomalous emission characteristic has been attributed to the presence of density of states (DOS) which is due to a certain degree of disorder occurring mainly at interfaces, which may be of compositional and/or structural origin [5]. An explanation of the anomalous behavior of the excitonic luminescence was given in [5] in terms of this disorder; we apply this explanation to our results presented in Figure 2. As the temperature rises from 10K to 50 K, the excitons gain just enough thermal energy to become trapped at the lower energy levels of the DOS, which

results in the red shift of the PL emission. From 50K, a thermal equilibrium is achieved and the excitons populate the higher levels of the DOS (blue shift) up to a maximum energy level, in this case $\sim 130\text{K}$ corresponding to an emission energy of 3.8 eV. From that point on, a “normal” band gap emission takes over which can be described in terms of Equation 1.

A model has been recently proposed to explain the blue temperature-induced shift in InGa_N-based quantum well luminescence [4]. The model is based on band-tail- filling of a Gaussian DOS with a parameter σ which describes the dispersion of the DOS (i.e. its width). The model calculation is given by [4]

$$E(T) = E_D - \frac{\sigma^2}{k_B T} \quad (2)$$

where E_D is attributed to the energy range between the center of the Gaussian DOS of the electrons and that of the holes. In addition, the model assumes that E_D depends on temperature in the same manner as the gap-energy, and thus E_D can be described via Equation 1. This model is valid in the temperature range where thermal equilibrium has been established: in our case $\sim 50\text{K}$ and above. We use this model to analyze our data in order to estimate the extent of the DOS in the superlattice; the fit is presented in Figure 2. We obtain the value for σ to be $\sim 11\text{ meV}$, which is a relatively small compared to the value of the superlattice emission ($\sim 3.8\text{ eV}$) indicating the high quality of the SL interfaces. Additionally, the inset to Figure 2 shows the PL linewidth as a function of temperature. The linewidth characteristic can also be separated into three different temperature regimes similar to those observed for the PL emission; the broadening mechanisms will be addressed at a later study. Equation 2 yields the values of the average electron-phonon interaction strength $\alpha = 135\text{ meV}$ and of the mean phonon temperature $\Theta = 573\text{ K}$, the latter which corresponds to a mean phonon energy $E_P = 50\text{ meV}$. This higher value of E_P obtained for the SL relative to that of GaN ($E_P = 27\text{ meV}$) may be explained in view of the model calculations developed for polar-optical phonons in GaN/AlGa_N-based quantum wells of wurtzite structure [14-15]. In that study, Komirenko et al. have shown that phonon modes in the heterolayers of GaN-AlGa_N based wurtzite heterostructures can exhibit the higher energies of the modes of the AlGa_N material [14, 15]. In light of the above model, the higher average phonon energy, E_P , found in our GaN wells are expected based on the predicted phonon mode structure in GaN/Al_{0.2}Ga_{0.8}N barriers.

In order to gain further insight into the mechanisms determining the recombination dynamics of the superlattice, the luminescence intensity, $I(T)$, as a function of temperature was investigated. Figure 3 presents the experimental data of that study and the curve fit to the data obtained from the relation which describes the PL intensity in the presence of a non-radiative channel with thermal activation energy E_A [16]:

$$\frac{I(T)}{I_0} = \frac{I}{1 + C \exp(-E_A / k_B T)} \quad (3)$$

In this relation C is a constant and I_0 is the PL intensity at zero absolute temperature. An activation energy $E_A=16$ meV was ascertained from the fit. This value is in the same order of magnitude and agrees with that obtained for the energy width of the DOS (11 meV), the small difference being attributed to an experimental error and the approximate nature of the above models. Thus at higher temperatures the tail states, due to interface disorder, are the non-radiative centers in the superlattice emission.

The temperature dependence of the luminescence blue shift in InGaN based quantum wells has been discussed in terms of the screening of the piezoelectric field [17]. In that model, as the temperature increases free carriers are thermally activated which in turn causes the screening of the field. As a result, modification of the band-gap takes place that manifests itself in the blue shift of the emission. Although this effect may be a possible additional mechanism causing the temperature dependent blue shift of the luminescence, it does not explain the initial red shift of the emission energy. As mentioned previously, similar luminescence behavior has been observed in the zincblende III-V quantum wells [5-8] which have considerably smaller piezoelectric fields [18]. We do not however preclude the screening effect of the PEF as an additional mechanism for the blue shift of the PL

In conclusion, the temperature behavior of the luminescence in a GaN/Al_{0.2}Ga_{0.8}N superlattice was investigated. Our analysis verifies the existence of a defect density of states, in the recombination of excitons at low temperatures. We also find that at high temperatures, the density of states acts as a non-radiative channel for the luminescence. The higher value of the average energy of the phonons involved in the superlattice scattering is consistent with the predictions for the phonon modes of GaN/AlGa_{0.8}N heterolayers.

ACKNOWLEDGMENTS

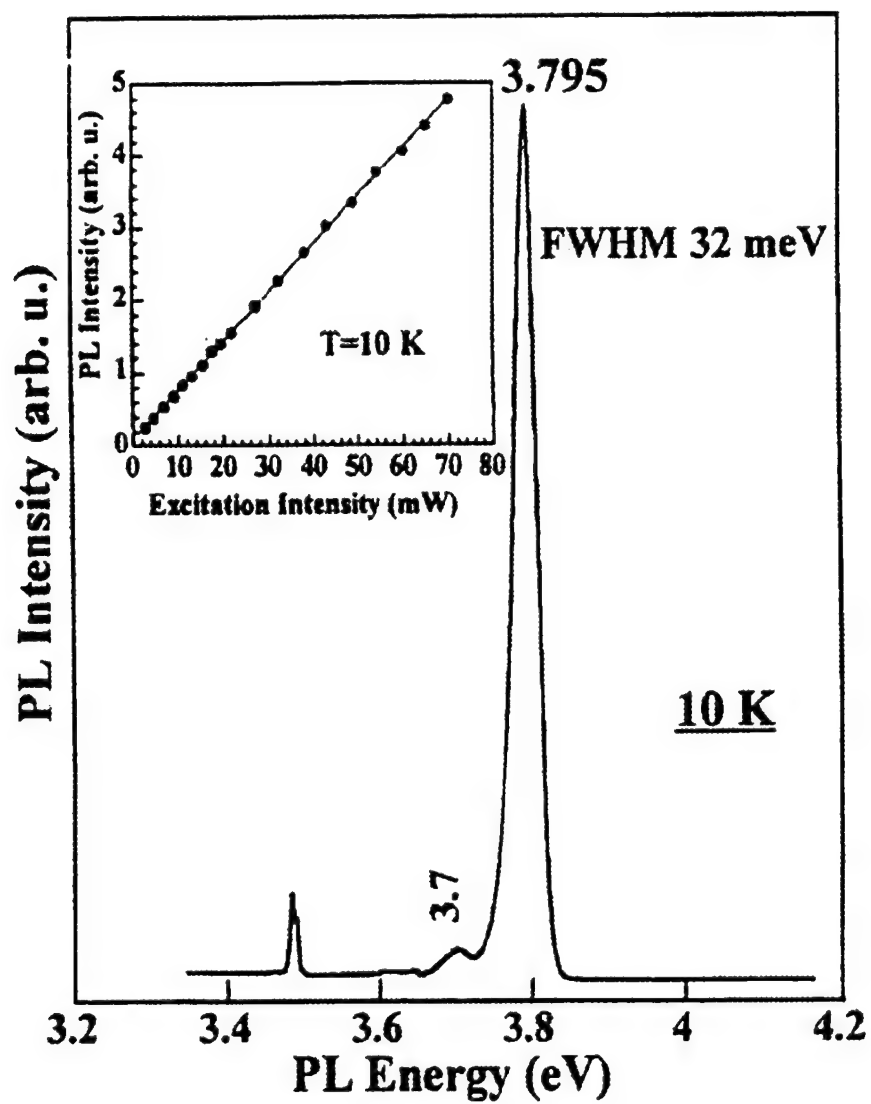
Leah Bergman acknowledges the Army Research Office via a National Research Council postdoctoral associateship for supporting this research.

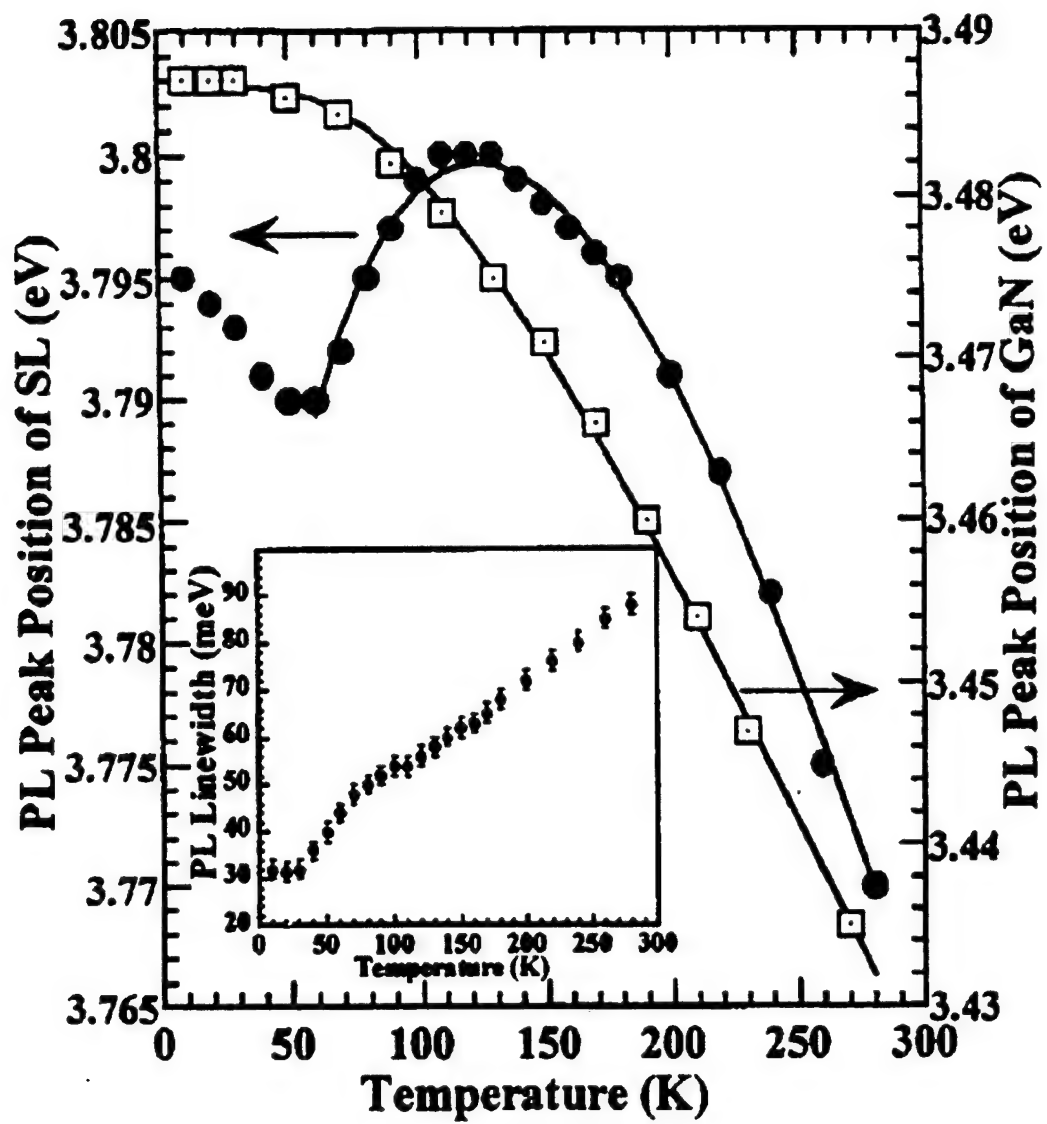
References

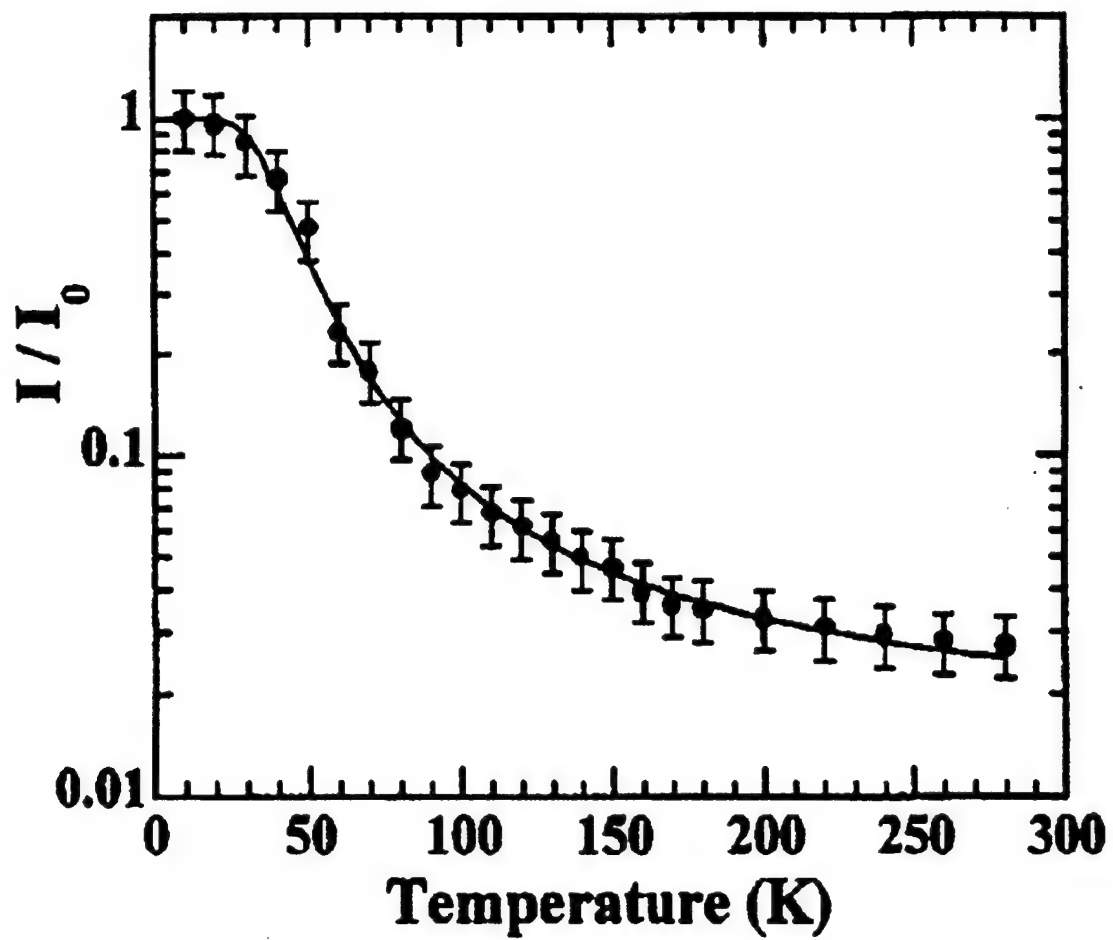
1. Y.P. Varshni, Physica 34, 149 (1967).
2. L. Vina, S. Logothetidis, and M. Cardona. Phys. Rev.B 30, 1979 (1984).
3. P. Lautenschlager, M. Garriga, S. Logothetidis, and M. Cardona. Phys. Rev.B 35, 9174 (1987).
4. P.G. Eliseev, P. Perlin, J. Lee, and M. Osinski, Appl. Phys. Lett. 71, 569 (1997).
5. M.S. Skolnick, P.R. Tapster, S.J. Bass, A.T. Pitt, and N. Apsley. Semicond. Sci. Technol. 1, 29 (1986).
6. S.T. Davey, E.G. Scott, B. Wakefield, and G.J. Davies. Semicond. Sci. Technol. 3, 365 (1988).
7. H. Nashiki, I. Suemune, H. Kumano, H. Suzuki, and T. Obinata. Appl. Phys. Lett. 70 2350, 569 (1997).
8. S. Guha, Q. Cai, M. Chandrasekhar, H.R. Chandrasekhar, H. Kim, A.D. Alvarenga, R. Vogelgesang, A.K. Ramdas, and M.R. Melloch. Phys. Rev.B 58, 7222 (1998).
9. S. Jin, Y. Zheng, and A. Li. J. Appl. Phys. 82, 3870 (1997).
10. C.F. Li, Y.S. Huang, L. Malikova, and F.H. Pollak. Phys. Rev.B 55, 9251 (1997).
11. A. Manoogian, and A. Leclerc, Phys. Stat. Sol. B 92, K23 (1979).
12. A. Manoogian, and J.C. Woolley, Can. J. Phys. 62, 285 (1983).
13. M.O. Manasreh, Phys. Rev.B 53, 16425 (1996).
14. S.M. Komirenko, K.W. Kim, M.A. Stroscio, and M. Dutta, Phys. Rev. B, 59, 5013 (1999)
15. S-G. Yu, K.W. Kim, L. Bergman, M. Dutta, M.A. Stroscio, and J.M. Zavada. Phys. Rev. B. 58, 15283 1998.
16. D. Curie in "*Luminescence in Crystals*" (John Wiley & Sons, New York, 1963).
17. P. Riblet, H. Hirayama, A. Kinodhita, A. Hirata, T. Sugano, Y. Aoyagi, Appl. Phys. Lett. 75, 2241 (1999).
18. F. Bernardini, V. Fiorentini, and D. Vanderbilt, Phys. Rev. B 56, R10024 (1997).

FIGURE CAPTIONS

1. The PL at 10K of the SL. The peak at 3.795 is due to the emission from the GaN wells. The inset to the Figure depicts the PL intensity as a function of the laser excitation power.
2. The temperature dependence of the PL peak position of the SL GaN wells (circles) and of GaN film (squares). The line represents the model of Equation 2. The inset to the Figure depicts the PL linewidth as a function of temperature.
3. The normalized PL intensity of the SL GaN wells as a function of temperature; Data points and the curve fit (line) to Equation 3.







Raman Analysis of the E1 and A1 Quasi-LO and -TO Modes in Wurtzite AlN

Leah Bergman, Mitra Dutta^(a), Cengiz Balkas^(b), Robert F. Davis^(b), James A. Christman,

Dimitri Alexson, and Robert J. Nemanich.

Department of Physics, North Carolina State University, Raleigh, NC 27695-8202

^(a) *U. S. Army Research Office, P. O. Box 12211, Research Triangle Park, NC 27709-2211*

^(b) *Department of Materials and Science Engineering, North Carolina State University, Raleigh, NC 27695.*

ABSTRACT

This paper presents a study of the quasi-LO and -TO modes in Wurtzite AlN which originate from the interaction of phonons belonging to the A1 and E1 symmetry groups. In order to analyze the allowed quasi as well as pure Raman modes, the modes were observed in a rotating crystallographic coordinate system, and the Raman tensors of the Wurtzite crystal structure were calculated as a function of the crystallographic rotation. The frequencies of the quasi-modes of Wurtzite AlN were also analyzed in terms of the interaction of the polar-phonons with the long range electrostatic field model. The experimental values of the Raman frequencies of the quasi-phonons concur with these expected from the model, implying that the long range electrostatic field dominates the short range forces for polar phonons in AlN.

INTRODUCTION

Raman spectroscopy has proven to be a useful and informative tool in the investigation of semiconductors with the Wurtzite (WZ) crystal structure, in particular in the investigation of material quality as well as in the study of phonon dynamics and interactions [1-9]. Due to the long range electrostatic field associated with the LO phonons, various types of interactions are allowed in the WZ semiconductors, among them the phonon-plasmon coupling [3]. Another is the possibility of interaction between polar modes belonging to different symmetry groups which result in the creation of new mixed-symmetry phonons referred to as quasi modes [1]. This paper presents a study of the LO and TO quasi modes in AlN crystallite which originate from the interaction of phonons belonging to the A1 and E1 symmetry groups; the study focuses on the mode-selection rules and mode-frequency calculations as well as on the Raman technique which enables the observation of the modes.

The theory developed by Loudon formulates that in uniaxial materials the polar phonon characteristics may be affected via two interaction mechanisms: one due to the long range electrostatic field, and the other due to the short range field which exhibits the anisotropy of the vibrational force constants [10]. The phonon dynamics and thus the Raman spectra depend on which of the two mechanism is the dominant interaction.

For the case where the long range electrostatic field is the dominant mechanism, the interaction of the polar phonons with the long range electrostatic field may result in a significant frequency separation between the group of the TO phonons relative to that of the LO phonons, as is schematically depicted in Figure 1a. Moreover, the TO phonons belonging to different symmetry are grouped together in a relatively narrow frequency range; the same holds for the LO phonons. One consequence of the dominant electrostatic field interaction is that the phonons exhibit nearly pure longitudinal or transverse character: essentially no mixing occurs between the transverse and the longitudinal atomic vibrations. The other consequence is that under certain propagation and polarization conditions, phonons of mixed A1 and E1 symmetry character exist and can be observed in the Raman spectra. These mixed symmetry modes are termed quasi-LO

and -TO modes. The frequencies of such quasi modes are predicted by the theory to be between the values of the pure-A1 and the pure-E1 for each of the LO and the TO bands.

Alternatively, for the case where the short range interatomic forces are dominant, the LO-TO splitting will be small and in this case the TO and LO mode of each symmetry group will occur in a relatively narrow band as shown in Figure 1b. The theory predicts that the phonons will exhibit essentially pure symmetry character (either A1 or E1). A consequence is that under certain propagation conditions the phonons will exhibit mixing of the transverse and longitudinal vibrations for a given symmetry. These mixed LO-TO modes are termed quasi-E1 and -A1 modes. The frequencies of such quasi modes are predicted by the theory to be in bands between the values of the TO-LO modes of the pure A1 or E1 phonons.

In AlN the E1(TO) and A1(TO) Raman frequencies are grouped together in $\sim 60 \text{ cm}^{-1}$ frequency range, the E1(LO) A1(LO) in $\sim 20 \text{ cm}^{-1}$ range, and the LO-TO group-splitting is $\sim 220 \text{ cm}^{-1}$. The frequency scheme of AlN thus implies the dominance of the long range electrostatic force interaction. The mode-mixing in AlN may occur if the propagation direction (q-vector) of the quasi-polar phonons, their polarization LO, and one of their two TO's, lie in the plane which spans between the c and the a_1 (or a_2) crystallographic axes [1]. This plane is referred as to the mixing plane. For example, the pure-A1 phonon has a c-direction polarization while the pure-E1 phonon is polarized in the basal plane; thus a quasi-phonon with the q-vector between the c and the a_1 axes would exhibit a mixed polarization of A1-E1 symmetry. When the q-vector lies along the crystallographic axes or in the a_1 - a_2 plane only pure phonons are observed in the spectra.

Arguello et al. investigated the long range electrostatic field interaction and the quasi modes in the WZ materials: ZnO, ZnS, and CdS [1]. In their study a frequency shift was observed of the quasi modes relative to that of the pure modes, in agreement with Loudons' theory. Filippidis et. al. have carried out plane-wave pseudopotential calculations to investigate the optical modes in GaN and AlN; their model and experiment concerning the A1(TO) mode agree with that of Loudons' [9].

In our study we investigate the behavior of the quasi-TO and the quasi-LO in AlN crystallite. We present calculations of the WZ Raman tensors as a function of rotation angle from which the allowed modes, pure and quasi, can be deduced and analyzed for different crystal orientations. The experimental values of the quasi frequencies agree well with those predicted by the phonon-electrostatic field interaction model. The motivation behind the present study was to gain information on the Raman frequencies from scattering geometries which are not along the crystallographic directions. As mentioned above, Raman spectroscopy has been successfully utilized in the characterization of the group III-nitrides semiconductors and has proven useful in studies of the stress state of films grown on the c-axis. However for films grown on other crystallographic directions, a technique which potentially might minimize film substrate interfacial stress, the contribution of the long range electrostatic field to the Raman shift has to be taken into consideration. This contribution has to be deconvoluted it in order to isolate the Raman shift due to stress.

EXPERIMENT

The micro-Raman scattering experiments were carried out at room temperature utilizing the 514.5 nm line of the ion argon laser and the J-Y U1000 scanning double monochromator. The spot size of the laser on the sample was $\sim 2 \mu\text{m}$ in diameter. The experimental error of the Raman peak position and the angle of rotation, θ , is $\pm 0.5 \text{ cm}^{-1}$, and $\pm 5^\circ$ respectively. The AlN crystallite, depicted in Figure 2, was grown via the sublimation process and its size is $\sim 500 \times 25 \times 25 \mu\text{m}$ [5]. In the figure, the face of the $(10\bar{1}0)$ plane is along the c-axis while the face of the (0001) plane is at the base of the hexagonal crystallite [5].

RESULTS AND DISCUSSION

In this study we observed the AlN quasi-TO and -LO modes by rotating the crystallite relative to the laboratory coordinate system as schematically depicted in Figure 3. In the figure, the X, Y, and Z are the axes of the fixed coordinate laboratory system (where X is out of the paper plane), while the c, a_1 and a_2 are the axes of the rotating coordinate system of the crystal (where a_2 is out of the paper plane and is coincided with the X-axis), and N is the normal to the crystallite surface (and is coincided with the a_1 -axis). The AlN crystallite was rotated through an angle θ about the X-axis such that the quasi-phonon propagation direction, the q-vector (\mathbf{q}), as well as its LO and one of its two TO components lay in the mixing c- a_1 plane (the other TO is along the X-axis). The micro-Raman spectra was acquired in a back scattering geometry from the Y-axis for various values of θ .

In order to investigate the polarization conditions upon which the quasi modes appear in the spectra, the Raman tensors, R_θ , of the rotating crystal (relative to a fixed X,Y,Z laboratory coordinate system) are calculated via the rotational transformation equation [11]:

$$R_\theta = T_x R T_x^{-1} \quad (1)$$

where T_x is the rotation matrix about the X-axis [12]. The Raman tensors of the WZ structure take the form:

$$A1_c(\theta) = \begin{pmatrix} h & 0 & 0 \\ 0 & h \cos^2 \theta + b \sin^2 \theta & b \sin \theta \cos \theta - h \sin \theta \cos \theta \\ 0 & b \sin \theta \cos \theta - h \sin \theta \cos \theta & h \sin^2 \theta + b \cos^2 \theta \end{pmatrix}$$

$$E1_x(\theta) = \begin{pmatrix} 0 & d \sin \theta & d \cos \theta \\ d \sin \theta & 0 & 0 \\ d \cos \theta & 0 & 0 \end{pmatrix} \quad E1_{a_1}(\theta) = \begin{pmatrix} 0 & 0 & 0 \\ 0 & 2d \sin \theta \cos \theta & d(\cos^2 \theta - \sin^2 \theta) \\ 0 & d(\cos^2 \theta - \sin^2 \theta) & -2d \sin \theta \cos \theta \end{pmatrix}$$

$$E2(\theta) = \begin{pmatrix} 0 & f \cos \theta & -f \sin \theta \\ f \cos \theta & 0 & 0 \\ -f \sin \theta & 0 & 0 \end{pmatrix} \quad E2(\theta) = \begin{pmatrix} f & 0 & 0 \\ 0 & -f \cos^2 \theta & f \cos \theta \sin \theta \\ 0 & f \cos \theta \sin \theta & -f \sin^2 \theta \end{pmatrix} \quad (2)$$

The tensors describe the in-crystal projections, due to the rotation, of the incident and scattered polarizations of the light. The group theory analysis indicates that the A1 is a non degenerate mode and thus has a one matrix representation, while the E1 and E2 are both doubly degenerate modes and therefore each mode-representation requires two matrices. The entries of each matrix, i.e. the constants h, b, d, and f, are related to the Raman cross section which determines the Raman intensity of each of the modes [13]. Moreover, for each polar mode the direction of the polarization is indicated in the subscripts: A1 is polarized along the c axis while E1 is polarized along a_1 and a_2 , the latter which coincides with the X-axis ($E1_x$). The polarization direction of the polar modes, like the Raman tensors, can be expressed in terms of the laboratory coordinate system; however, it is not necessary for the present study. For $\theta=0$ the crystal coordinate system coincides with that of the laboratory ($a_1=Y$ and $c=Z$, see Fig. 3), and Eq. 2 takes the usual form [1, 13].

For the first set of experiments we chose the Raman setup such that the incident light is polarized along the X-axis and the scattered light has both X and Z polarization directions, expressed in Raman notation as: $Y \begin{pmatrix} X & X \\ Z \end{pmatrix} \bar{Y}$. This choice of polarization implies that the XX and the XZ components of each of the Raman tensors will contribute a Raman signal provided they are not zero. Figure 4 presents the Raman spectra for this setup for rotations: $\theta = 0^\circ, 35^\circ$, and 70° . Inspection of Eq.2 indicates that the E2 mode should appear in the spectra since the XX and the XZ components of its tensors are not zero; our spectra display the E2 mode at 655 cm^{-1} . This mode is non-polar and as such no change in frequency is expected as a function of the rotation. The XZ component of the $E1_x$ is non-zero, and although the q-vector of the mode lies in the a-c mixing plane its polarization is not: it is in the X-direction (TO component) and thus no symmetry mixing is expected. This analysis indicates that the spectra should exhibit the pure- $E1(\text{TO})$ with no

change of frequency upon rotation. The pure-E1(TO) in our spectra is at 669 cm⁻¹ and is independent of rotation.

Next we investigated the A1 mode which contributes a signal to the Raman spectra via the non-zero value of its XX tensor component. The pure-A1 mode has solely c-polarization; however, upon rotating the crystal quasi modes are created for which their TO and LO components have a c-polarization component of A1 symmetry as well as an a₁-polarization component of E1 symmetry. This situation is schematically depicted in the inset to Figure 3. In the figure, the TO component of the quasi-mode lies in the mixing plane and is composed of A1 and E1 polarization symmetry components; the quasi-TO mode will have mostly A1 symmetry for q-vectors near the a-axis and mostly E1 symmetry for q-vectors near the c-axis. The frequency of the quasi-TO, according to Loudons' theory, should be between the frequency of the pure-A1(TO) mode and that of the pure-E1(TO) mode. As can be seen in Figure 4, the frequency of the A1(TO) mode shifts from its pure value at 608 cm⁻¹ towards that of the E1(TO) mode as a function of the rotation angle: for $\theta=35^\circ$ the peak of the quasi-TO is at 614 cm⁻¹ and for $\theta=70^\circ$ is at 620 cm⁻¹. The spectrum of $\theta=70^\circ$ exhibits a small peak of the pure-A1(TO) and is attributed to an internal reflection.

The frequencies of the quasi-TO can be calculated via the relation [1,10]

$$\omega_{Q(TO)}^2 = \omega_{E1(TO)}^2 \cos^2(90 - \beta) + \omega_{A1(TO)}^2 \sin^2(90 - \beta) \quad (3)$$

where β (see Fig. 3) is the propagation angle of the q-vector of the quasi-phonon (**q**) in the crystallite, and is related to the angle of rotation, θ , via Snell's law and the momentum-conservation law of the Raman scattering effect as is discussed next. The conservation law states that in the scattering medium $\mathbf{q} = \mathbf{k}_i - \mathbf{k}_s$ where \mathbf{k}_i and \mathbf{k}_s are wavevectors of the incident and scattered photons respectively [13-14]. Thus, for our backscattering geometry the q-vector lies along the same path as that of the incident and scattered photons. To find the angle, β , of that path the index of refraction has to be taken into account via Snell's law: $n_1 \sin \theta = n_2 \sin \beta$, where for air

$n_1=1$ and for AlN $n_2=2.2$ which is the accepted value in the visible range and of negligible anisotropy [15]. Our calculations yield a value of $\beta=15^\circ$ for the rotation $\theta=35^\circ$, and from Eq. 3, $\omega_{Q(TO)} = 612 \text{ cm}^{-1}$, a value which concurs with our experimental finding of 614 cm^{-1} . For the 70° rotation, $\beta=25^\circ$ and $\omega_{Q(TO)} = 619 \text{ cm}^{-1}$, a value which is similar to the experimental result of 620 cm^{-1} .

Lastly we investigated the quasi-LO Raman mode. In order to observe this mode the incoming polarization of the light was set at the Z-direction such that the Raman geometry was $Y\left(\begin{smallmatrix} Z & X \\ & Z \end{smallmatrix}\right)\bar{Y}$. This Raman geometry enables the observation of the quasi-LO modes since the ZZ component of the $E1_a$ Raman tensor is non-zero for $\theta>0$ as is indicated by Eq. 2. In this configuration the q-vector of the phonon as well as its polarization directions lie in the mixing plane. Figure 5 presents the Raman spectra of the quasi-LO mode for $\theta=15^\circ$, 35° , and 70° , and the pure A1(LO) mode at $\theta=90^\circ$; the Raman peak positions are at 913 cm^{-1} , 912 cm^{-1} , 908 cm^{-1} , and 890 cm^{-1} respectively. Taking into account the index of refraction and utilizing the equation for the quasi-LO frequencies [1,10],

$$\omega_{Q(LO)}^2 = \omega_{A1(LO)}^2 \cos^2(90 - \beta) + \omega_{E1(LO)}^2 \sin^2(90 - \beta) \quad (4)$$

where $\omega_{A1(LO)}$ is 890 cm^{-1} and $\omega_{E1(LO)}$ is 916 cm^{-1} [4], we found the calculated quasi frequencies to be 915 cm^{-1} , 914 cm^{-1} , and 911 cm^{-1} , which agree well with the above experimental values.

Figure 6 summarizes our findings. In the figure the lines denote the TO and LO quasi-frequencies calculated utilizing Loudons' model (Eqs. 3 and 4), and the dots represent our experimental values for the modes. The additional data points of the quasi-TO modes, represented by X's, are from Filippidis et al who were the first to observe the quasi-TO modes in AlN [9]; our results are in agreement with theirs. Moreover, as depicted in the figure, our study of the quasi-TO as well as the quasi-LO concur with Loudons' model, implying the presence of a long range

electrostatic field which is active in the coupling of modes belonging to the different symmetry groups.

One important implication of the above findings involves the accurate determination of the Raman frequency acquired from AlN thin films. In such films, due to their micron-size dimension along one of the crystallographic axes, the determination of the various Raman frequencies requires the data to be acquired at grazing angle geometry. Such an experimental setup, which deviates by an angle from the crystallographic coordinate system, may result in a mode mixing of a characteristic Raman frequency. Due to the strong angular dispersion of the quasi-TO mode frequency, a disparity in the TO Raman frequency values of thin films is expected to be observed; less disparity is expected for the LO mode. A similar effect in which the frequency is shifted from its pure value is also expected to occur in films grown on crystallographic directions which do not coincide with the c-axis. As Raman spectroscopy is widely used in the determination of stress in thin films via the Raman frequency shift, the possible additional shift due to the electrostatic field effect has to be considered.

CONCLUSIONS

The Raman tensors of the WZ structure were calculated as a function of the crystallographic rotation and the allowed modes for various rotations were studied. The LO and TO quasi-modes of AlN crystallite were observed and analyzed in terms of the phonon-electrostatic field interaction model. The Raman selection rules as well as the experimental values of the Raman frequencies concur with the model implying the dominance of the long range electrostatic field in AlN. The quasi-TO mode exhibits a shift of 12 cm^{-1} relative to its pure value for mode-propagation angle $\sim 25^\circ$ measured from the a-axis. For the same propagation direction, the quasi-LO mode exhibits a shift of $\sim 5 \text{ cm}^{-1}$.

ACKNOWLEDGMENTS

We gratefully acknowledge the Army Research Office and the National Research Council for supporting this research.

REFERENCES

1. C.A. Arguello, D.L. Rousseau, and S.P.S. Porto, Phys. Rev. **181**, 1351 (1969).
2. L. Bergman, M.D. Bremser, W.G. Perry, R.F. Davis, M. Dutta, and R.J. Nemanich. Appl. Phys. Lett. **71**, 2157 (1997).
3. T. Kozawa, T. Kachi, H. Kano, Y. Taga, M. Hashimoto, N. Koide, and K. manabe, J. Appl. Phys. **75**, 1098 (1994).
4. L.E. McNeil, M. Grimsditch, and R.H. French, J. Am. Ceram. Soc. **76**, 1132 (1993)
5. C.M. Balkas, Z. Sitar, T. Zheleva, L. Bergman, R.J. Nemanich, and R.F. Davis. J. Crys. Growth, **179**, 363 (1997).
6. T. Azuhata, T. Sota, K. Suzuki, and S. Nakamura, J. Phys.: Condens. Matter **7**, L129 (1995).
7. J.A. Sanjurjo, E.L. Cruz, P. Vogl, and M. Cardona, Phys. Rev. **B28**, 4579 (1983).
8. L. Bergman, and R.J. Nemanich, Annu. Rev. Mater. Sci. **26**, 551 (1996).
9. L. Filippidis, H. Siegle, A. Hoffmann, C. Thomsen, K. Karch, and F. Bechstedt, Phys. Stat. Sol. **B198**, 621 (1996).
10. R. Loudon, Advan. Phys. **13**, 423 (1964).
11. D. A. Long in "Raman Spectroscopy" (McGraw-Hill, New York, 1977).
12. G. B. Arfken, and H. J. Weber, in "Mathematical Methods for Physicists", (Academic Press, Boston, 1995).
13. W. Hayes, and R. Loudon, in "Scattering of Light by Crystals", (John Wiley & Sons, New York, 1978).
14. M. Cardona in "Light Scattering in Solids II", ed. M. Cardona, and G. Gunthrod, (Springer-Verlag, New York 1982).
15. S. Loughin, and R. H. French, in "Properties of Group III Nitrides" Ed. J. H. Edgar, (INSPEC, London, 1994).

FIGURE CAPTIONS

Figure 1. Raman frequency scheme and directions of phonon vibration for (a) the case when the long range electrostatic field is the dominant interaction, and (b) when the anisotropy of the short range dominates the interaction.

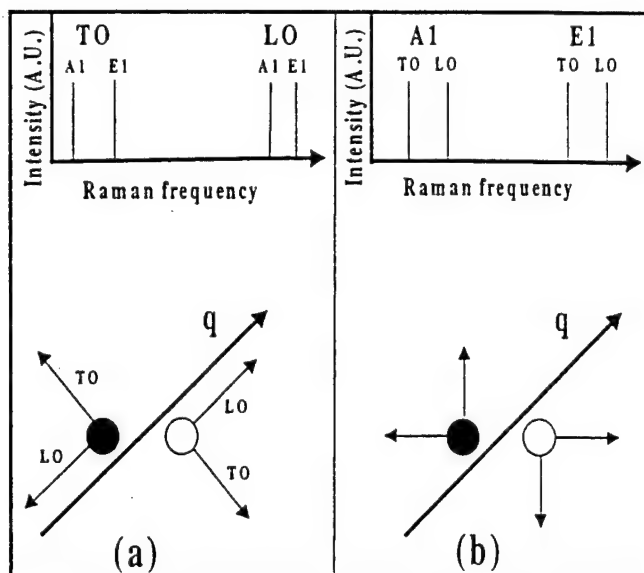
Figure 2. A micrograph of the Wurtzite AlN crystallite, size $\sim 500 \times 25 \times 25 \mu\text{m}$. Along the c-axis is the face of the $(10\bar{1}0)$ plane, the face of the (0001) plane is at the base of the hexagonal crystallite.

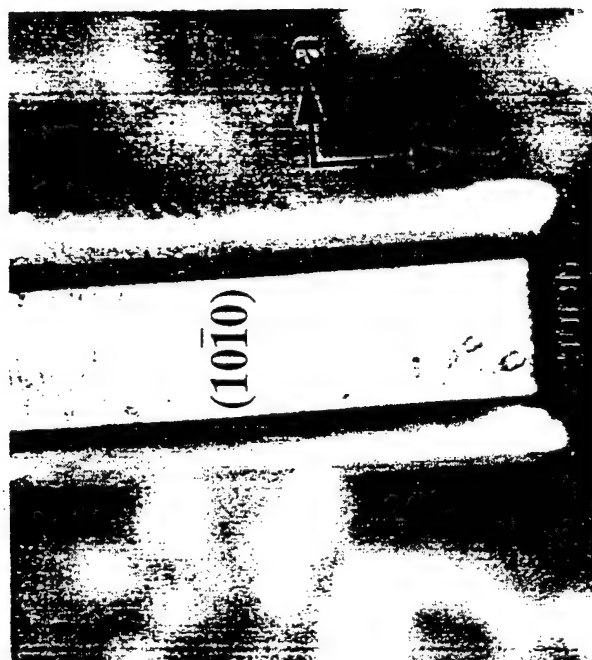
Figure 3. The geometry of the experimental setup. The laboratory coordinate system is: X, Y, and Z (X is out of the paper plane). The crystal-rotating system is: c, a_1 , and a_2 (a_2 out of the paper plane and is coincided with the X-axis). N is the normal to the surface and coincides with the a_1 -axis. The angle of rotation about the X-axis is θ , while the angle of refraction and phonon propagation is β . The dashed line represents the propagation of the phonon with a q-vector; the arrows represent its LO and TO components. The Raman spectra were acquired in a backscattering geometry from the Y. The inset to the figure describes the A1-E1 mixing of the LO and the TO components.

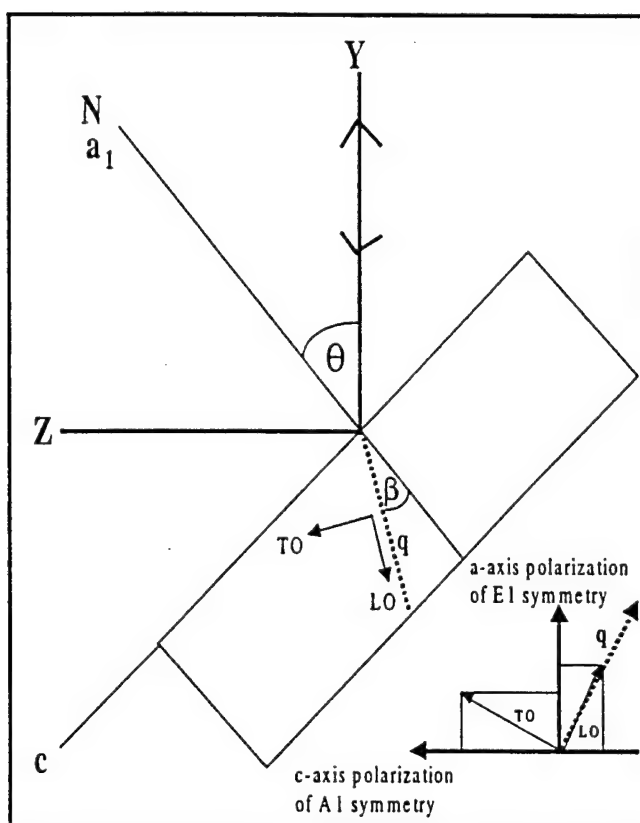
Figure 4. The Raman spectra for rotation angle $\theta = 0^\circ, 35^\circ$, and 70° . The pure-A1(TO) is at 608 cm^{-1} , and the quasi-TO modes are at 614 cm^{-1} , and 620 cm^{-1} . All intensities are normalized to that of the E2 mode.

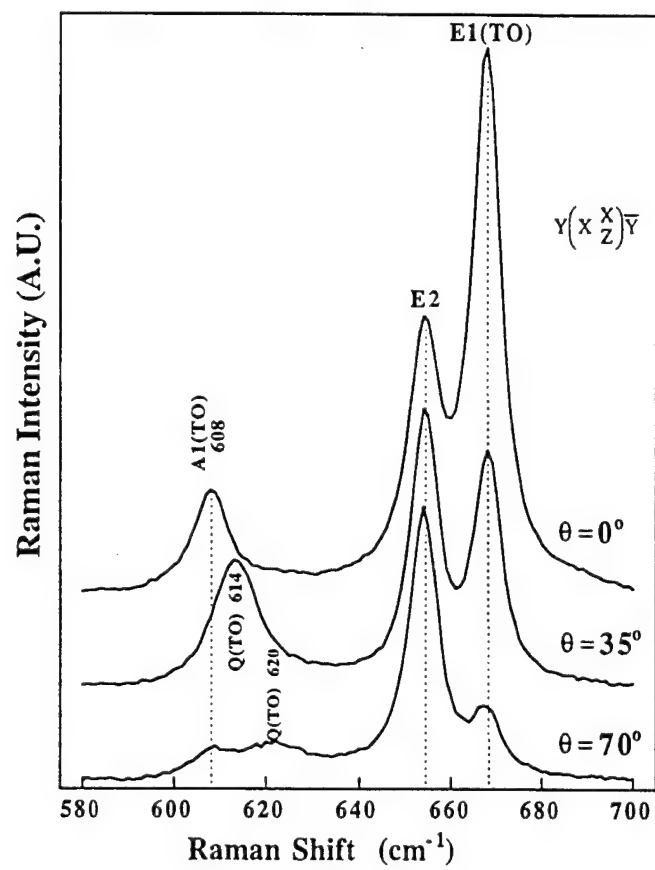
Figure 5. The normalized Raman spectra of the quasi-LO modes for rotation angle $\theta = 15^\circ, 35^\circ$, and 70° . The pure $A_1(\text{LO})$ is also presented for which $\theta = 90^\circ$.

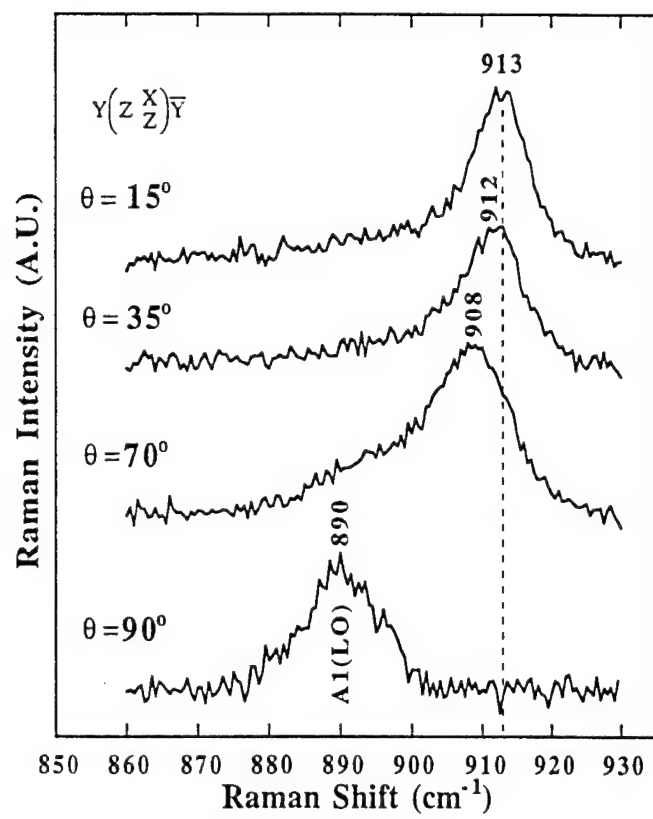
Figure 6. The behavior of the quasi-LO and -TO modes as a function of phonon propagation angle β (measured from the a-axis). The lines represent the TO and LO quasi frequencies calculated using Loudons' model equations 3 and 4; the dots represent our experimental values for the LO and the TO modes, the value of the pure $E_1(\text{LO})$ is from reference 4 (presented by a triangle), while the X's represent the data points of the quasi TO from reference 9.

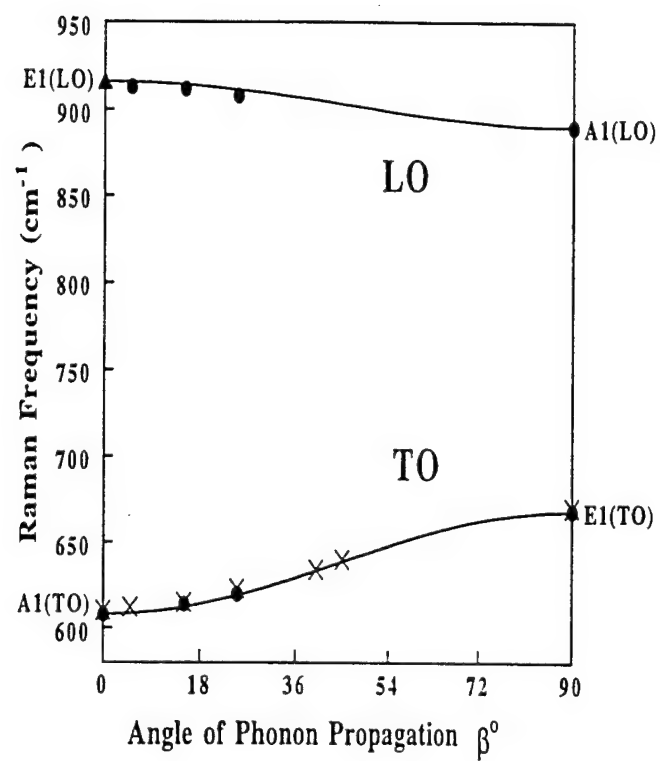












Raman Scattering Spectroscopy and Analyses of

III-V Nitride-Based Materials

Leah Bergman^{*}, Mitra Dutta[†], and Robert J. Nemanich^{*}

^{*} Department of Physics, North Carolina State University, Raleigh, NC 27695-8202

[†] US Army Research Office, Research Triangle Park, NC 27709-1221

Abstract This paper reviews Raman studies of GaN, AlN, InN, and the alloy systems $\text{Ga}_x\text{Al}_{1-x}\text{N}$ and $\text{In}_x\text{Ga}_{1-x}\text{N}$. The review focuses on the applications of Raman spectroscopy to material characterizations and phonon dynamics of the wurtzite (WZ) and the zincblende (ZB) polytypes. Among the topics addressed are structure determination and microstructure identification, stress and strain in film-substrate interfaces and in crystallites, phonon-plasmon coupling, and the determination of free carrier density. The issue of phonon mode-type in the alloys is also examined, as well as the topic of alloy order. The subject of the quasi-modes, their angular dispersion, and the dominance of the long range electrostatic field is addressed. Also, the issues of the isotope effects on the various vibrational modes as well as the phonon lifetimes are discussed.

1. Introduction

The potential of UV optoelectronic devices made of III-V nitrides has prompted numerous studies focusing on the properties of this family of materials [1-5]. One of the most attractive properties of the III-V nitrides is the nature of their wide band gaps, which in the wurtzite structure have the values of 1.95 eV for InN, 3.45 eV for GaN, and 6.4 eV for AlN [2, 5]. In addition, the superior mechanical and thermal properties of the III-V nitrides, as well as the feasibility of alloying and the material polymorphism, have made this family of materials a unique candidate for synthesizing high-performance UV devices.

Raman spectroscopy has contributed a great deal to the advances in the III-V nitride field, and the key studies leading to these advances are reviewed here. This review focuses in particular on the application of Raman spectroscopy to topics that are of concern to material scientists including structure determination, stress analysis, determination of free carrier concentrations, and material quality characterization. Other issues such as alloy-disorder and alloy-mode, isotopic effects, and aspects of phonon dynamics and phonon lifetimes are also addressed. The implications of these issues for material characterizations are discussed as well.

In Section 2 a discussion of the underlying principles involved in Raman scattering experiments on wide band-gap semiconductors is presented. Section 3 focuses on Raman selection rules and studies concerning the structural properties of the III-V nitrides. In particular, Section 3.1 surveys polarized Raman analyses of the wurtzite and zincblende structures, and Sections 3.2 and 3.3 review structure-related studies of GaN, and AlN and InN respectively. Stress effect studies on GaN and AlN films and crystallites are next reviewed in Section 4. The relevance of the hydrostatic and biaxial Raman stress coefficients to stress analysis of the nitride

films and crystals is discussed. Specifically, Sections 4.1 and 4.2 focus on stress analysis of GaN and AlN, respectively.

Section 5 is devoted to Raman analyses of the *LO*- and *TO*-quasi-modes and their frequency dispersion; the implications of the dispersion to film characterization are also presented. Another topic addressed in Section 6 is the *LO* phonon-plasmon coupling and the resulting spectral lineshape. The validity of using the lineshape as a measure of the free carrier concentration in GaN is discussed. In Section 7 studies of the isotopic effects on the phonon dynamics as well as studies concerning the mode lifetimes are summarized. Section 8 presents Raman studies of III-V nitride alloy systems. The one-mode and two-mode behavior of phonons in the alloy is described, and experimental and theoretical studies are presented. The topic of alloy disorder and its detectability via Raman spectroscopy is addressed as well. Section 9 concludes with comments about directions of future research.

2. Experimental Considerations for Raman Scattering of Wide Band-Gap Semiconductors

In its general form the Raman scattering intensity I can be expressed as

$$I(\omega_L) \propto \omega_s^4 |\hat{\mathbf{e}}_s \cdot \mathbf{R} \cdot \hat{\mathbf{e}}_L|^2 \left| \sum_{\alpha\beta} \frac{1}{(E_\alpha - \hbar\omega_L)(E_\beta - \hbar\omega_s)} \right|^2, \quad (1)$$

where ω_L , ω_s are the incoming and scattered laser frequencies, respectively; E_α and E_β are the energies of intermediate crystal states (to be defined); \mathbf{R} is the Raman tensor; and $\hat{\mathbf{e}}_s$ and $\hat{\mathbf{e}}_L$ are the scattered and incident polarization vectors. In (1) the first term is due to the dipole transition radiation, the second represents the Raman selection rules, which come about from crystal symmetry considerations, and the last term leads to resonance effects [6].

Energy conservation relates ω_L and ω_s to the phonon frequency ω :

$$\omega_p = \omega_i - \omega_s \quad (2)$$

As the incident laser frequency approaches the energies of the crystal intermediate states, the Raman intensity becomes larger and the signal is said to be resonance-enhanced; an additional enhancement comes from the dipole radiation term. In general, for semiconductors there may be three relevant types of intermediate states: Bloch states which are the conduction-valence bands, exciton states, and in-gap impurity states. Thus as the incident frequency approaches the band-gap frequency, an enhancement of the Raman intensity should be observed. Similarly, resonance may be achieved via the interaction of the incoming light with the exciton states as well as the impurity states.

The band gaps of InN, GaN, and AlN are listed in Table 1 [2]. It is evident that if enhancement of the Raman signal of pure GaN is to be achieved, a laser line in the lower energy range of the UV ($\approx 2.7\text{--}4$ eV) should be utilized [7], unless impurity resonance is present [8]. Resonance Raman scattering of AlN and AlGaN alloys, on the other hand, requires laser excitation lines in the deep UV range ($\approx 4\text{--}7$ eV) depending on the alloy composition [9]. The resonance of the Raman signal of InN, due to its narrower band gap, can be achieved via excitation in the visible optical range. For laser excitation energy much above the fundamental band-gap energy of the semiconductor, the light is absorbed and thus only a small volume of the material is probed. In the case of strong absorption the Raman signal would be significantly weakened.

Table 1. Band-gap energies in units of eV of GaN, AlN, and InN [2].

Structure	GaN	AlN	InN
Wurtzite	3.39 (200 K)	6.2 (300 K)	1.89 (300 K)
	3.50 (1.6 K)	6.28 (5 K)	
Zincblende	3.2-3.3 (300 K)	5.11 (300 K)	2.2 (300 K)

3. Raman Scattering of GaN, AlN, and InN Films and Crystallites

GaN, AlN, and InN based materials can be grown in the wurtzite as well as the zincblende structure, depending mainly on the choice of substrates and growth conditions [10-12]. Unintentional coexistence of both structures in a film thus may occur. This section focuses on the identification of the structure in the films via polarized Raman spectroscopy and analysis.

3.1 Raman Tensors and Structure Identification of GaN, AlN, and InN

The III-V nitrides are highly stable in the hexagonal WZ structure and high quality material in that structure has been achieved [13]. However, it has been demonstrated that the growth of films in the less stable cubic ZB structure is feasible as well [14-17]. Due to the polymorph nature of the III-V nitrides, the identification of material structure as well as its purity, i.e., the possibility of polytype material, is an issue. The following section addresses the topic of Raman spectroscopy for structure determination of GaN, AlN, and InN films and crystallites.

The WZ crystal structure belongs to the space group C_{6v}^4 , and the group theory analysis predicts the zone-center optical modes $A_1 + 2B_1 + E_1 + 2E_2$ [18]. The A_1 , E_1 , and the two E_2 modes are Raman active, while the B_1 modes are silent, i.e., forbidden in Raman scattering. Furthermore, the A_1 and E_1 modes are polar: their vibrations polarize the unit cell which results in

the creation of a long-range electrostatic field. The effect of this field manifests itself in the splitting of the A_1 , E_1 modes into longitudinal optical (LO) and transverse optical (TO) components, thus creating the $A_1(LO, TO)$ and $E_1(LO, TO)$ modes. Figure 1 depicts the scheme of the vibrational modes in the wurtzite structure [19]. The ZB structure belongs to the space group T_d^2 and group theory predicts one Raman active mode of T_2 representation: it is a polar mode which splits into the TO and LO components [18, 20].

Tables 2 and 3 list the experimental Raman frequencies that have been reported for WZ- and ZB-GaN, respectively [14, 16, 17, 21-28]. In Table 4 the Raman frequencies of AlN and InN are listed as well. There are small differences in the Raman frequencies presented in Tables 2, 3 and 4, which in most cases are due to differences in material quality. Moreover, as can be observed in the Tables, the Raman frequency of the TO mode of the ZB lies between the frequencies of the E_1 (TO) and the $A_1(TO)$ of the WZ; similarly, the frequencies of the LO , $E_1(LO)$, and the $A_1(TO)$ lie in the same range. The close proximity of the ZB and the WZ phonons has been attributed to the close relation between these two structures [29], and is explained as follows. The WZ structure, consisting of four atoms per primitive cell, can be obtained from the ZB structure, consisting of two atoms per cell, by a rearrangement of the atom-planes that are perpendicular to the (111) axis [29]. Due to this relation the WZ phonon dispersion curve along [0001] may be obtained via folding of the ZB phonon dispersion along the [111] direction, thus doubling the phonon modes in the WZ Brillouin zone as required by the increased number of the atoms per primitive cell.

Figure 2 presents a description of the phonon dispersion of the two structures. In the figure, the LO 's and the TO 's of the ZB structure are plotted along the Γ -L [111] direction (thick lines); the folding creates the two E_2 branches and the two B_1 branches (thin lines) along the Γ -A [0001] direction of the WZ structure. Moreover, due to the WZ crystal potential, a splitting occurs in

which the $E_1(TO)$ and $A_1(TO)$, and the $E_1(LO)$ and $A_1(LO)$ branches (dashed lines) are created from the original TO and LO branches, respectively [29]. Thus, as can be seen in Fig. 2, the folding and splitting mechanisms cause the Raman frequencies of the $A_1(TO)$ and $E_1(TO)$ modes of the WZ structure to be in the same range as that of the TO mode of the ZB structure; the same holds for the LO modes.

Table 2. Raman frequencies (cm^{-1}) of the WZ-GaN modes.

E_2^1	145		144	143		144	142
E_2^2	568	568	569	568	570	569	567
$A_1(TO)$	533	533	532	533		533	530
$A_1(LO)$					738	735	
$E_1(TO)$	559	559	560	559		561	558
$E_1(LO)$				726		743	
Ref.	[21]	[22]	[23]	[25]	[24]	[26]	[27]

Table 3. Raman frequencies (cm^{-1}) of the ZB-GaN modes.

TO		554	555	555
LO	730	740	740	737
Ref.	[16]	[17]	[28]	[14]

Table 4. The Raman frequencies (cm^{-1}) of WZ-AlN and WZ- and ZB-InN.

WZ-AlN					WZ-InN		ZB-AlN
E_2^1	241	252	246	249			655 (TO)
E_2^2	660	660	655	657	495	491	
$A_1(\text{TO})$	607	614	608	610			
$A_1(\text{LO})$		893	890		596	590	902 (LO)
$E_1(\text{TO})$		673	668	670			
$E_1(\text{LO})$	924	916		913			
Ref.	[30]	[31]	[27]	[32]	[33]	[34]	[15]

The identification of the Raman mode may be achieved using the Raman tensors. Equations (3) and (4) present the Raman tensors for the ZB and WZ structures respectively [18]. The x , y , and z in the equations represent the phonon-polarization direction for each of the polar modes. Each non-zero entry in the matrices represents a coupling of the polarization of the incoming and scattered light to the lattice vibrations that results in an allowed Raman spectral line via the second term of (1). Throughout this review Porto notation $a(bc)d$ will be used to describe a Raman geometry: a and d represent the wavevector direction of the incoming and scattered light respectively, while b and c represent their polarization state [35]. Additionally, for each of the polar modes the direction of the phonon propagation with respect to its polarization direction determines whether the observed spectral line is of a longitudinal or a transverse mode. The phonon propagation direction can be ascertained via the wavevector conservation law: $\mathbf{k}_L = \mathbf{k}_S + \mathbf{q}$, where \mathbf{k}_L and \mathbf{k}_S are the wavevectors of the incoming and the scattered light, respectively, and \mathbf{q} is the phonon wavevector.

Thus, for example, the Raman backscattering configuration $z(xy)\bar{z}$ would give rise to the LO mode in a case of ZB-(001) oriented crystallographic plane or to the two E_2 modes in a case of WZ-(0001) plane. The other modes are said to be symmetry forbidden at that configuration and will not appear in the spectra unless a mechanism exists, such as internal reflection due to defects and interfaces, that may cause the forbidden scattering.

$$u_x: \begin{pmatrix} 0 & 0 & 0 \\ 0 & 0 & d \\ 0 & d & 0 \end{pmatrix} \quad u_y: \begin{pmatrix} 0 & 0 & d \\ 0 & 0 & 0 \\ d & 0 & 0 \end{pmatrix} \quad u_z: \begin{pmatrix} 0 & d & 0 \\ d & 0 & 0 \\ 0 & 0 & 0 \end{pmatrix} \quad (3)$$

$$A_1(z): \begin{pmatrix} a & 0 & 0 \\ 0 & a & 0 \\ 0 & 0 & b \end{pmatrix} \quad E_1(x): \begin{pmatrix} 0 & 0 & c \\ 0 & 0 & 0 \\ c & 0 & 0 \end{pmatrix} \quad E_1(y): \begin{pmatrix} 0 & 0 & 0 \\ 0 & 0 & c \\ 0 & c & 0 \end{pmatrix} \quad (4)$$

$$E_2: \begin{pmatrix} f & 0 & 0 \\ 0 & -f & 0 \\ 0 & 0 & 0 \end{pmatrix} \quad \begin{pmatrix} 0 & -f & 0 \\ -f & 0 & 0 \\ 0 & 0 & 0 \end{pmatrix}$$

3.2 Wurtzite and Zincblende Phases of GaN

GaN in the WZ structure has been grown in the crystalline form of needles and platelets as well as heteroepitaxial films [1, 2, 5]. The most widely used substrates are sapphire(0001), 6H-SiC(0001), and ZnO(0001). Their thermal expansion coefficients and lattice constants are approximately matched to GaN. Among the first to identify the Raman modes in WZ-GaN were Manchon et al. [21], Lemos et al. [22], Burns et al. [23] and Cingolani et al. [25], followed by Murugkar et al. [24] and Azuhata et al. [26]. Table 5 lists the scattering configurations and the observable modes for the WZ-GaN film studied by Azuhata et al. [26]. The 2 μm GaN film in that

study was grown on a sapphire(0001) substrate via MOCVD and was capped with a thin layer of InGaN. The sample quality was reported to be comparable to that of a double-heterostructure light-emitting diode [26]. Figures 3 and 4 show the Raman spectra of that film.

Table 5. Scattering configurations and observable Raman modes of WZ-GaN(0001) [26].

Raman geometry	Raman mode
$y(xx)\bar{y}$	$A_1 (TO), E_2^1, E_2^2$
$y(zz)\bar{y}$	$A_1 (TO)$
$y(zx)\bar{y}$	$E_1 (TO)$
$z(xy)\bar{z}$	E_2^1, E_2^2
$z(xx)\bar{z}$	$A_1 (LO), E_2^1, E_2^2$

The values of the LO - and the TO -phonon may be used to determine the dielectric constants of a material via the Lyddane-Sachs-Teller relation [36]

$$\omega_L^2 = \frac{\epsilon_0}{\epsilon_\infty} \omega_T^2 \quad (5)$$

In this relation ϵ_0 is the static dielectric constant of the crystal, while ϵ_∞ is the dielectric constant at optical frequencies, and ω_L and ω_T are the LO - and the TO -frequency, respectively. Since GaN is an uniaxial crystal, there are two values for each of the dielectric constants defined as ϵ_\perp and ϵ_\parallel , respectively; the directions given are relative to the c -axis. In that respect, the phonons of E_1 symmetry correspond to the perpendicular Lyddane-Sachs-Teller relation whereas the A_1 phonons to the parallel relation. Moreover, infrared reflectivity measurements have indicated that for GaN $\epsilon_{\perp\omega} \cong \epsilon_{\parallel\omega}$, i.e., in the optical frequency range GaN is approximately an isotropic material [21].

Using the Raman frequencies of the *LO* and *TO*, Azuhata et al. calculated the perpendicular and the parallel static dielectric constants of the GaN film to be $\epsilon_{\perp 0} = 9.28$ and $\epsilon_{\parallel 0} = 10.1$, respectively (for $\epsilon_{\perp \infty} = \epsilon_{\parallel \infty} = 5.29$) [26]. These values are in accord with the ones obtained via infrared reflectivity and Kramers-Kronig analyses [37].

In contrast to the extensive studies that have been conducted on WZ-GaN material, the cubic phase is as yet a new and largely unexplored area. Raman and X-ray scattering studies of ZB-GaN films, grown on GaAs(001) substrates by metalorganic vapor phase epitaxy (MOVPE), have been reported by Miyoshi et al. [16]. In their study, the structure of the films was first identified via X-ray diffraction and then confirmed by Raman analysis. The X-ray spectra exhibit the (200) diffraction peak of the cubic face whereas the (0002) diffraction of the WZ symmetry is absent. In order to verify the X-ray findings, Raman spectra was acquired in the $z(xy)\bar{z}$ configuration for which the *LO* of the cubic symmetry is an allowed mode from the (001) face. The spectra of that study consist of a line at $\approx 730 \text{ cm}^{-1}$ which has been attributed by Miyoshi et al. to the *LO* mode of the ZB-GaN [16]. Moreover, from the X-ray data the authors calculated the lattice constant of the ZB-GaN to be 4.5 \AA , which agrees well with their theoretical calculation. In light of that, Miyoshi et al. concluded that despite the 20% lattice mismatch with the GaAs substrate, the ZB-GaN films ($\approx 0.4 \text{ }\mu\text{m}$ thick) are almost strain-free due to a relaxation mechanism occurring at the early stages of the growth [16].

Phonon characteristics of cubic, hexagonal, and mixed phase GaN films grown via molecular beam epitaxy (MBE) on GaAs(001) substrates were studied by Giehler et al. [17]. Each film in this study was grown under different conditions to invoke the growth of the different structure types. The structural properties were analyzed by high-energy electron diffraction and X-ray scattering, and the phonon characteristics were investigated utilizing infrared transmission and

Raman spectroscopy. The structural analysis conducted by Giehler et al. revealed that the sample grown under Ga-rich conditions (sample A) consists of nonepitaxial hexagonal columns whose c -axes are aligned parallel to the [001] direction of the substrate. The film grown under N-rich conditions (sample B) exhibits a phase mixture, while the film grown under near-stoichiometric conditions (sample C) was mainly cubic.

The infrared transmission spectra of sample A consist of signals at 558 cm^{-1} and 735 cm^{-1} , which have been attributed by Giehler et al. to the $E_1(TO)$ and $A_1(LO)$ phonons, respectively, of the WZ-GaN. The spectra of sample C reveals transmittance signals at 552 cm^{-1} and 739 cm^{-1} that were assigned to the TO and LO phonons, respectively, of the ZB-GaN [17]. The spectra in the TO frequency range of the mixed sample exhibit a broad signal centered approximately between the $E_1(TO)$ and the TO modes; similarly, the signal in the LO range is broad and centered between the $A_1(LO)$ and the LO modes. The Raman spectra of the three samples are presented in Fig. 5; the spectra were acquired in the $z(xy)\bar{z}$ configuration. The spectra of sample A exhibit the E_2^2 mode at 569 cm^{-1} and a broad band $\sim 680\text{ cm}^{-1}$ which has been assigned by the authors to a disordered state. The spectra of sample C consist of the allowed LO mode at 740 cm^{-1} and the symmetry forbidden TO mode at 554 cm^{-1} . The forbidden scattering has been explained by Giehler et al. to occur via multiple reflections inside the film. The spectra of the mixed phase film exhibit the E_2^2 of the WZ structure, the LO and the TO of the ZB, and a broad band due to a disorder-activated scattering [17].

Comparative Raman studies of cubic and hexagonal GaN have been reported also by Tabata et al [14]. In that study, both WZ and ZB films were grown on GaAs(001) substrates via MBE. The nucleation of the two structures was achieved by varying the Ga-to-N flux ratio in the initial stage of the growth: the growth of the ZB film was initiated using N-rich conditions, and that of

the WZ phase was obtained under a slight excess of Ga [14]. The X-ray spectra of the sample grown under Ga-rich condition (sample A) exhibit the (0002) and the (0004) diffraction peaks associated with the WZ-GaN, whereas the spectra of the sample grown under N-rich condition (sample B) exhibit the (002) peak of the ZB-GaN. From these findings, the authors concluded that sample A has a WZ structure with the surface-normal parallel to the c -axis, and sample B consists of ZB structure with the surface-normal parallel to the cubic axis [14].

The Raman spectra of samples A and B are presented in Figs. 6 and 7, respectively. The spectra were acquired in nearly backscattering geometry with polarized incident light and unanalyzed scattered light. Moreover, the spectra in Tabata's study were acquired at three different incident wavelengths in order to enhance the Raman signal [14]. Figure 6 exhibits the allowed E_2^2 mode at 571 cm^{-1} as well as the $A_1(LO)$ mode at 737 cm^{-1} , which is also allowed in that configuration. The Raman spectra of the ZB-GaN in Fig. 7 exhibit the allowed LO mode at 741 cm^{-1} , and the forbidden TO mode appears as well at 555 cm^{-1} . The appearance of the TO mode was attributed by Tabata et al. to the presence of a short-range perturbation in the film, which relaxes the Raman selection rules [14].

3.3 Wurtzite and Zincblende Structure of AlN and InN

In the following, a review of Raman scattering studies in AlN and InN is presented. AlN and InN, like GaN, in the stable state have a wurtzite crystal structure and belong to the space group C_{6v}^4 . The cubic zincblende phase of AlN and InN can be grown as well; however, these materials have been studied much less than the wurtzite polytype. The Raman selection rules leading to mode assignments and polytype identification are the same as those for GaN, as described in Section 3.1.

Figure 8 shows typical Raman spectra of a WZ-AlN crystallite grown via the sublimation method [27]. The spectra were acquired in a backscattering geometry from the α -face of the crystallite, and the Raman frequencies are listed in Table 4. Figures 9 and 10 present the Raman spectra of a ZB-AlN film along with that of ZB-AlGaN films; the symmetry-allowed LO and the forbidden TO modes of the cubic ZB are both present in the spectra [15]. These cubic films were grown by Harima et al. via the MBE method on cubic SiC/Si substrates, and the cubic phase was confirmed by X-ray diffraction as well to be the major structure [15].

Due to the difficulties in achieving reasonably good quality InN films, information on its material properties is as yet scarce. Raman scattering studies of InN films grown on (0001) sapphire substrates via metalorganic vapor phase epitaxy were first reported by Kwon et al. [33]. X-ray diffraction indicated that the structure of the InN films was wurtzite. Identification of the Raman modes was carried out via the Raman selection rules in a backscattering geometry; the modes are listed in Table 4. The authors reported a linewidth of 20 cm^{-1} for the E_2^2 mode, a value that is larger compared to the E_2^2 linewidths of WZ-GaN and AlN, which usually range from 3 to 8 cm^{-1} . Lee et al. investigated the unusual line broadening of the InN Raman modes as a function of growth temperature [34]. These films were grown at temperature ranges of $325\text{-}600^\circ\text{C}$ via the same method used by Kwon et al. It was found that in the elevated temperature range (450°C and above), the E_2^2 linewidth is $\approx 6 \text{ cm}^{-1}$ while in the lower range the linewidth is $\approx 70 \text{ cm}^{-1}$; the broadening of the spectral lines was accompanied by a frequency shift as well. Lee et al. suggested that this significant line broadening reflects the coexistent of cubic and amorphous phases in the WZ structure of the InN films [34].

4. Stress Analysis and Substrate Issues for Epitaxial Growth

Among the important factors leading to the synthesis of high quality films is the availability of matching substrates. In order to minimize the internal stress, the substrate under consideration should have lattice parameters and thermal expansion coefficients similar to these of the film. Table 6 lists some of the substrates most commonly used in the growth of III-V nitride films, as well as their lattice parameters and thermal expansion coefficients [2].

One of the most informative methods of measuring stress in materials is Raman spectroscopy [19, 38, 39]; however, it requires an a-priori knowledge of the Raman pressure coefficients that relate the peak position to the stress. The following reviews some of the Raman studies concerning the determination of the pressure coefficients and the stress state in GaN and AlN.

Table 6. Material properties for the GaN-and AlN-substrate system [2].

Material	Lattice parameters (Å)	Coefficients of thermal expansion ($10^{-6}/K$)
6H-SiC	$a = 3.080$	4.2
	$c = 15.12$	4.68
Sapphire	$a = 4.758$	7.5
	$c = 12.99$	8.5
ZnO	$a = 3.252$	2.9
	$c = 5.213$	4.75
WZ-AlN	$a = 3.112$	4.2
	$c = 4.982$	5.3
WZ-GaN	$a = 3.189$	5.59
	$c = 5.185$	3.17

4.1 Stress Analysis of GaN Films

A detailed study of the effect of pressure on the crystalline WZ-GaN Raman spectral lines was reported by Perlin et al. [38]. The applied pressure was hydrostatic in the range 0 to 50 GPa. The

pressure dependence of the Raman frequencies of the $A_1(TO)$, $E_1(TO)$, E_2^2 , and E_2^1 modes was shown to follow the quadratic relation [38]:

$$\omega(\text{cm}^{-1}) = \omega_0 + \sigma_1 P + \sigma_2 P^2 \quad (6)$$

where P is the applied pressure in units of GPa, ω_0 is the Raman frequency at zero applied pressure, and σ_1 and σ_2 are the first and second order pressure coefficients, respectively. The hydrostatic pressure coefficients derived from first principal density-functional calculations by Gorczyca et al. [19] were found to agree well with the experimental results [38]. Table 7 summarizes the set of parameters for the various Raman modes.

Table 7. The hydrostatic pressure coefficients of WZ-GaN, σ_1 and σ_2 , in units of $\text{cm}^{-1}/\text{GPa}$ and $\text{cm}^{-1}/(\text{GPa})^2$, respectively, as obtained from theory [19] and experiment [38].

Raman mode	Theory		Experiment	
	σ_1	σ_2	σ_1	σ_2
$E_1(TO)$	4.10	0.013	3.68	-0.0078
E_2^1	-0.15	0.006	-0.25	-0.0017
E_2^2	4.46	0.018	4.17	-0.0136
$A_1(TO)$	4.08	0.024	4.06	-0.0127

The stress-strain relation for an isotropic material under hydrostatic pressure is [40, 41]:

$$\varepsilon = E^{-1} \sigma (1 - 2\nu), \quad (7.1)$$

where ε is the strain, E the Young's modulus, σ the stress, and ν the Poisson ratio. However, for thin epitaxial films the stress is more likely to be two dimensional due to film-substrate lattice and thermal mismatches (see Table 6). For the case of biaxial stress, σ_a , a strain is induced in the basal plane, ε_a , and along the c -direction, ε_c ; the isotropic constituent equations are [41]:

$$\varepsilon_a = E^{-1} \sigma_a (1-2\nu) \quad (7.2a)$$

$$\varepsilon_c = -E^{-1} \sigma_a 2\nu. \quad (7.2b)$$

For thin epitaxial films, the biaxial stress approximations in (7.2 a, b) may be used to describe the stress state of a thin film if the stress contribution from point defects is negligible [40].

Kisielowski et al. have analyzed the stress state of GaN films grown on the *c*-face of SiC and sapphire [40]. The authors analyzed the stress in the films in terms of the biaxial isotropic approach described in (7.2). It was shown that, due to point defects, an additional hydrostatic component has to be superimposed to the biaxial component in order to fully describe the stress state of the films. Moreover, Kisielowski et al. determined that a biaxial stress of 1 GPa would shift the Raman peak position of the E_2^2 mode by $\approx 4.2 \text{ cm}^{-1}$, a result consistent with the values listed in Table 7.

Strain effect studies in epitaxial GaN grown on AlN-buffered Si(111) have been reported by Meng et al. [42]. One of the objectives of the study was the determination of the Raman stress coefficient for the biaxial stress state, taking into account the hexagonal anisotropy. An outline of their method is presented here. The films were grown via RF-glow discharge reactive magnetron sputtering at various RF input powers. Raman and X-ray spectroscopy established that the film structure is WZ with an (0001) orientation. In their analysis, Meng et al. assumed a biaxial stress state and took into consideration the hexagonal anisotropy; the constituent relation in that case is [42]:

$$\sigma_a = \frac{2C_{13}^2 - C_{33}(C_{11} + C_{12})}{2C_{13}} \varepsilon_c. \quad (8)$$

Using the elastic constants C_{ij} for WZ-GaN in (8) the authors obtained $\sigma_a = -202\varepsilon_c$. The values of the vertical strain ε_c determined via X-ray measurements were correlated to the RF input power

and to the E_2^2 Raman peak position; in both cases a direct correlation was found. The vertical strain-Raman frequency relation found for the E_2^2 mode was $\omega(\varepsilon_c) = 561 + 701\varepsilon_c$, which in conjunction with (8) yields the relation between the biaxial stress and the Raman frequency to be $\omega(\sigma_a) = 561 + 4.4\sigma_a$. Thus the biaxial pressure coefficient found in the study of Meng et al. (4.4 $\text{cm}^{-1}/\text{GPa}$) [42] is comparable to the hydrostatic pressure coefficient [38].

Other studies of stress-related phenomena have been reported [43-45]; a brief summary is given below. Thermal stress effects on GaN films of differing thickness grown on the c -plane of sapphire substrates were investigated by Kozawa et al [45]. As can be seen in Table 6, a significant difference exists between the thermal expansion coefficients of GaN and those of sapphire, which produces a compressive stress in the film. In the studies of Kozawa et al., the magnitude of the biaxial compressive stress in each of the GaN films was obtained via the curvature wafer bending method; the obtained values were correlated to the peak positions of the E_2^2 Raman mode. It was found that the Raman pressure coefficient is 6.2 $\text{cm}^{-1}/\text{GPa}$, a value somewhat greater than the one listed in Table 7. Additionally, the authors demonstrated that the compressive stress decreases as the thickness of the film increases: for $\approx 5 \mu\text{m}$ and $50 \mu\text{m}$ films the Raman peak position was found to be at 569 and 567.5 cm^{-1} , respectively [45].

Rieger et al. investigated the influence of the AlN buffer layer, when deposited on the c -plane of sapphire substrates, on the stress state of the GaN films [43]. In order to estimate the stress magnitude, they analyzed the Raman peak position of the E_2^2 mode as a function of the AlN layer thickness. Rieger et al. observed a pronounced reduction of the compressive stress in the GaN films with increasing AlN buffer layer thickness. According to the authors, an AlN layer thicker than 200 nm eliminates the compressive stress completely [43]. Depth profiles of the strain in a

220- μm thick GaN film grown on sapphire were investigated by Siegle et al. utilizing Raman spectroscopy PL and CL imaging [44]. The depth profile of the stress was determined from the peak position of the E_2^2 mode. The authors found that the stress decreases nearly exponentially with increasing distance from the substrate; the film was found to be relaxed at a distance ≈ 35 μm away from the substrate.

4.2 Stress Analysis in WZ-AlN

The influence of hydrostatic pressure on the Raman frequencies of WZ-AlN has been investigated by various groups [19, 30, 46]. The Raman pressure coefficients for the AlN modes, defined in (7.1), are listed in Table 8.

Table 8. The hydrostatic pressure coefficients of WZ-AlN, σ_1 and σ_2 , in units of $\text{cm}^{-1}/\text{GPa}$ and $\text{cm}^{-1}/(\text{GPa})^2$ respectively as obtained from theory [19] and experiment [30].

Raman mode	Theory		Experiment	
	σ_1	σ_2	σ_1	σ_2
$E_1(TO)$	4.36	0.059		
E_2^1	-0.29	0.022		
E_2^2	4.79	0.063	3.99	0.035
$A_1(TO)$	4.29	0.019	4.63	-0.01
$E_1(LO)$			1.67	0.27

Figures 11 and 12 [19] show the functional behavior of the Raman modes under pressure; the dots represent the experimental data of [30] while the lines represent the model calculation [19]. One of the most intriguing aspects of these results is the anomalous behavior of the E_2^1 mode of

AlN as well as of GaN; unlike the other modes it decreases to lower frequencies with increasing pressure. This tendency is better expressed in terms of the Grüneisen parameter γ_i [47]:

$$\gamma_i = \frac{B_0}{\omega_i} \left(\frac{d\omega_i}{dP} \right), \quad (9)$$

where the ω_i 's are the given phonon modes, B_0 is the bulk modulus, and P is the pressure. Thus all the AlN and GaN modes have positive γ values, excepting the E_2^1 mode, which has a negative γ value. Similar behavior has been found in CdS and ZnO, both of which have a WZ structure [47]. It has been suggested that the negative γ value may indicate a softening of the lattice to a particular mode under compression, preceding a first-order transition [19, 47]. Moreover, it has been established that WZ-ZnO and -CdS undergo a phase transition to the NaCl structure [47]; the same phase transition has been suggested to occur in GaN crystallites at ≈ 45 GPa [38]. However, the reason for the softening of the E_2^1 mode in the wurtzite structure materials needs further investigation.

5. Raman Analysis of the Quasi-Modes in AlN

The theory developed by Loudon formulates that in uniaxial materials the polar phonon characteristics may be affected via two interaction mechanisms: one due to the long range electrostatic field, and the other due to the short range field which exhibits the anisotropy of the vibrational force constants [18, 48]. The phonon dynamics and thus the Raman spectra depend on which of the two mechanisms is the dominant interaction. Figure 13 depicts the Raman frequency scheme and the direction of phonon vibrations for both interactions [49].

For the case where the long range electrostatic field is the dominant mechanism, the interaction of the polar phonons with the long range electrostatic field may result in a significant

frequency separation between the group of the TO phonons relative to that of the LO phonons. Moreover, the TO phonons belonging to different symmetry are grouped together in a relatively narrow frequency range; the same holds for the LO phonons. One consequence of the dominant electrostatic field interaction is that under certain propagation and polarization conditions, phonons of mixed A_1 and E_1 symmetry character exist and can be observed in the Raman spectra [48]. These mixed symmetry modes are termed quasi- LO and $-TO$ modes. The frequencies of such quasi modes are predicted by the theory to be between the values of the pure A_1 and E_1 modes for each of the LO and the TO bands. Alternatively, for the case where the short range interatomic forces are dominant, the LO - TO splitting will be small and in this case the TO and LO mode of each symmetry group will occur in a relatively narrow band.

In AlN the $E_1(TO)$ and $A_1(TO)$ Raman frequencies are grouped together within about 60 cm^{-1} , the $E_1(LO)$ and $A_1(LO)$ within 20 cm^{-1} , and the LO - TO group-splitting is $\approx 220 \text{ cm}^{-1}$. The frequency scheme of AlN thus implies the dominance of the long-range electrostatic force interaction. The mode-mixing in AlN may occur if the propagation direction (q -vector) of the quasi-polar phonons lies in the plane which spans between the c and the a_1 (or a_2) crystallographic axes [50]. This plane is referred as to the mixing plane. For example, the pure A_1 phonon has a c -direction polarization while the pure E_1 phonon is polarized in the basal plane; thus a quasi-phonon with the q -vector between the c and the a_1 axes would exhibit a mixed polarization of A_1 - E_1 symmetry. When the q -vector lies along the crystallographic axes or in the a_1 - a_2 plane, only pure phonons are observed in the spectra. A detailed analysis of the Raman configurations that enable the observation of the quasi modes in WZ materials is given in [50] and [49].

Raman studies of quasi modes in AlN have been reported by Filippidis et al. [32] and Bergman et al. [49]. In these studies the q -vector direction was achieved by rotating the crystallite by an angle θ relative to a fixed laboratory coordinate system, as depicted in Fig. 14. Figures 15 and 16 present Raman spectra for various rotations in a scattering configuration that enables the quasi- TO and $-LO$ to be observable [49]. Figure 17 shows the behavior of the quasi-modes as a function of the phonon propagation angle β , where β is related to θ via Snell's law and a small anisotropy is assumed. In Fig. 17 the points represent the experimental results while the lines represent Loudon's model [48, 50]:

$$\omega_{Q(TO)}^2 = \omega_{E1(TO)}^2 \cos^2(90 - \beta) + \omega_{A1(TO)}^2 \sin^2(90 - \beta) \quad (10a)$$

$$\omega_{Q(LO)}^2 = \omega_{A1(LO)}^2 \cos^2(90 - \beta) + \omega_{E1(LO)}^2 \sin^2(90 - \beta) . \quad (10b)$$

As was discussed in [49], one important implication of these results involves the accurate determination of the Raman frequency acquired from AlN thin films. In such films, due to their μm -size dimension along one of the crystallographic axes, the determination of the various Raman frequencies requires the data to be acquired at grazing angle geometry. Such experimental setup, which deviates by an angle from the crystallographic coordinate system, may result in a mode mixing of a characteristic Raman frequency. Due to the strong angular dispersion of the quasi- TO mode frequency (see Fig. 17), a disparity in the TO Raman frequency values of thin films is expected to be observed; less disparity is expected for the LO mode. A similar effect in which the frequency is shifted from its pure value may also occur in films grown at off-crystallographic directions. In measuring the stress state of the films, the possible additional shift due to the electrostatic coupling needs to be considered.

6. Phonon-Plasmon Interaction in GaN Films and Crystallites

Raman spectroscopy has proven to be a useful tool in analyzing the effect of free electrons on the lattice dynamics of GaN which, as grown, tends to be an n -type material [4]. A free carrier concentration in GaN may be achieved via intentional n -type doping or via the growth method [5, 51]. In general, when an appreciable free carrier concentration is present in a polar-semiconductor, a coupling of the LO -phonons to the plasma oscillations of the free carriers (plasmons) may occur [52]. The phonon-plasmon interaction results in a characteristic Raman scattering that may yield information on the free carrier density of a given sample [51, 53-58]. This section examines the topic of Raman phonon-plasmon coupled modes in GaN.

The determination of the free carrier concentration via Raman spectroscopy is often more advantageous than that via electrical measurements since no contacts are required. The plasma frequency ω_p at wavevector $q = 0$ is related to the free carrier concentration n through the relation [36]:

$$\omega_p^2 = \frac{4\pi n e^2}{m^* \epsilon_\infty}, \quad (11)$$

where ϵ_∞ is the high frequency dielectric constant, e is the charge, and m^* is the effective mass of the free carriers. Moreover, in the case when the plasma oscillations are not overdamped the frequencies of the coupled plasmon- LO -phonon may be approximated by [59]:

$$\omega_\pm^2 = \frac{1}{2} \left\{ (\omega_{LO}^2 + \omega_p^2) \pm \left[(\omega_{LO}^2 + \omega_p^2)^2 - 4\omega_p^2 \omega_{TO}^2 \right]^{1/2} \right\}. \quad (12)$$

Therefore the Raman spectra in principle should exhibit two spectral lines corresponding to an upper branch coupling ω_+ and a lower branch ω_- (also known as L_+ and L_-) whose frequencies depend on the free carrier concentration. No LO -mode is expected in the spectra. The two

coupled frequencies have been observed in the Raman spectra of n -type GaAs as well as other III-V semiconductors of the ZB structure [20].

In the case of overdamped plasmons (12) is not applicable; the spectra cannot be analyzed in terms of the ω_+ and ω_- coupled modes. However, the case of large damping of the plasma oscillations in 6H-SiC (doped with nitrogen $\sim 10^{19} \text{ cm}^{-3}$) has been analyzed and modeled by Klein et al. [60]. In their study the Raman spectra of the SiC do not exhibit the ω_+ and ω_- branches. Instead, the influence of the coupling manifests itself in the lineshape of the LO -mode: it is asymmetrically broadened and slightly shifted toward the frequency range where the ω_+ was supposed to be (in the case of small damping). Moreover, Klein et al. demonstrated that the line broadening as well as intensity reduction is directly correlated to the increase of carrier concentrations. The influence of damping effect on the Raman scattering efficiency of the coupled modes has also been investigated by Hon et al. [61] and by Irmer et al. [62] in the case of n -type GaP. The Raman spectra were found to exhibit characteristics similar to those of n -type SiC. The model developed to explain the effect of the large damped plasmons on the coupled modes can be expressed as [60-62]:

$$I(\omega) \approx [1, C, C^2] \text{Im}(-1/\epsilon) \quad (13a)$$

$$\epsilon(\omega) = \epsilon(\infty) \left[1 + \frac{\omega_L^2 - \omega_T^2}{\omega_T^2 - \omega^2 - i\gamma\omega} - \frac{\omega_p^2}{\omega^2 + i\gamma_p\omega} \right], \quad (13b)$$

where $I(\omega)$ is the Raman cross section, $\epsilon(\omega)$ is the dielectric function, and $[1, C, C^2]$ is the interference factor expressed in term of the Faust-Henry coefficient C [61]. In (13b) ω_L , ω_T and ω_p are the frequencies of the longitudinal phonon, the transverse phonon, and the plasmons, respectively. Additionally, γ and γ_p are the damping constants of the phonons and the plasmons,

respectively. Equation (13a), when fully expanded, predicts the Raman lineshape of the phonon-plasmon coupled modes.

In a manner similar to SiC the plasma oscillations in GaN are considered to be overdamped. Kozawa et al. investigated the $A_1(LO)$ phonon-plasmon coupled mode in WZ-GaN film as a function of a relatively low level of Si-dopant concentration [51]. The dopant concentration in these samples ranged from about 1×10^{16} to $2 \times 10^{18} \text{ cm}^{-3}$. Figure 18 depicts the Raman spectra of the $A_1(LO)$ mode at several carrier densities; here the Raman band shifts towards the high frequency side as well as broadens and weakens as the carrier concentration increases. The spectra of the $A_1(LO)$ coupled mode as well as the model predicted by the lineshape (13) are presented in Fig. 19. The inset to the figure lists the values of the fitting parameters, among which are the plasma damping constant $\gamma = 400 \text{ cm}^{-1}$ and the plasma frequency $\omega_p = 119 \text{ cm}^{-1}$, the latter from which the carrier concentration may be evaluated via (11). Figure 20 shows the carrier concentration n calculated from the Raman data versus the one obtained from the Hall measurements. As shown in the figure, the values of the concentrations obtained in both techniques agree [51].

Kirillov et al. studied the effect of free carriers on phonon-plasmon interactions in WZ-GaN films in the high concentration regime [54]. The concentrations in their study were determined via Hall measurements to be $4 \times 10^{19} \text{ cm}^{-3}$ for sample A and $8 \times 10^{19} \text{ cm}^{-3}$ for sample B. From those measurements the plasma damping constant for sample A was been determined to be 1116 cm^{-1} . Figure 21 presents the Raman spectra acquired in a backscattering geometry from the c -face of the two films: neither spectra exhibits the allowed $A_1(LO)$ mode at $\approx 735 \text{ cm}^{-1}$. In order to gain further insight into the dynamics of the phonon-free carrier interactions, Kirillov et al. calculated the expected spectra using Klein's model expressed in (13a,b). Figure 22 shows the calculated

spectra for a free carrier concentration of $4 \times 10^{19} \text{ cm}^{-3}$ for two values of the plasma damping constant. The dotted line in Fig. 22 is a calculated spectrum for a hypothetical sample with a low damping constant of 100 cm^{-1} . This value is typical for plasmons in GaAs films; in that material the upper branch coupling ω_+ and a lower branch ω_- have been clearly identified. The solid line in Fig. 22 is the calculated spectrum where the damping constant is taken to be that of sample A (1116 cm^{-1}). As shown in the figure the lines become much broader as the plasma damping constant increases, with the upper branch being the most affected.

In contrast to the study of Kozawa et al. in the low dopant regime, the study of Kirillov et al. indicates that for high free carrier concentrations Raman spectroscopy may not be a useful tool to extract qualitative information on the concentration [54]. This is because the line of the upper branch of the phonon-plasmon coupling is too broad to allow a meaningful analysis. However, the model calculations presented in Fig. 22 reveal that the line of the lower branch at $\approx 530 \text{ cm}^{-1}$ is not too broad and thus potentially may be used in the concentration analysis. This line corresponds to the 523 and 530 cm^{-1} spectral lines of samples A and B, respectively (see Fig. 21). However, due to defects and inhomogeneities in the film, which relax the Raman selection rules, the $A_1(\text{TO})$ mode near 530 cm^{-1} may be present in the spectra as well. Thus the identification of the lower phonon-plasmon coupling mode has to be dealt with cautiously.

A detailed investigation into the issue of the lower branch of the phonon-plasmon coupled modes in the case of high carrier concentration was carried out by Demangeot et al. [55]. The GaN sample was found via infrared reflectivity measurements to contain a high level of free carrier $\approx 10^{20} \text{ cm}^{-3}$, and the plasma damping constant was determined to be 1480 cm^{-1} [55]. Figure 23 shows Raman spectra of the GaN film that were acquired at two locations on the sample. As can be seen in the figure, a relatively broad Raman peak at 525 cm^{-1} is present in the spectra.

Demangeot et al. used the model of (13a, b) and found a good fit (dotted line in the figure) to the Raman data of the low branch coupled mode. As can be observed in Fig. 23, the Raman spectra in the high frequency range do not exhibit the $A_1(LO)$ mode nor a pronounced high-branch coupled mode, results which are consistent with the model calculation. Additionally, the results of Demangeot et al. indicate that the distribution of the free carriers is not uniform across the GaN sample.

The fact that in the limit of low free carrier concentration the modified $A_1(LO)$ is present in the Raman spectra led Wetzel et al. to quantitatively determine the concentrations [57]. In this study they investigated bulk GaN crystallites and correlated the free carrier concentration to the Raman peak position of the coupled $A_1(LO)$ -plasmon mode. The authors suggested that the following correlation holds in the concentration range of $10^{17} \text{ cm}^{-3} < n < 10^{19} \text{ cm}^{-3}$ [57]:

$$n(\omega) = 1.1 \times 10^{17} \text{ cm}^{-3} (\omega - 736)^{0.764}. \quad (14)$$

In the above approximation ω is the $A_1(LO)$ phonon-plasmon coupled mode in cm^{-1} , and the value 736 is the frequency of the $A_1(LO)$ Raman mode. At that low level of free carriers, Ponce et al. investigated the spatial distribution in GaN crystallites via a Raman imaging technique [56]. The underlying principle of the technique involves the recording and digitization of the $A_1(LO)$ -plasmon mode intensity across the sample. The images presented by Ponce et al. show a variation of brightness across the crystallite, with the areas of brightness corresponding to low doping concentration [56].

7. Isotopic Effects and Phonon Lifetimes in the Wurtzite Materials

Since the isotope mass affects the phonon frequency, Raman analysis of isotopic films may convey information on the elements controlling the mode-vibrations. Such studies of WZ-GaN films made

from natural Ga and N as well as the isotope ^{15}N have been reported by Zhang et al. [63]. In the film containing the ^{15}N all of the observed Raman modes, excluding the E_2^1 , were found to exhibit prominent downward frequency shifts. Additionally, the Raman frequencies of the polar modes $A_1(\text{LO}, \text{TO})$ and $E_1(\text{LO}, \text{TO})$ were found by Zhang et al. to be shifted according to the inverse square root of the reduced masses, as would be expected from the first principal calculations of crystal dynamics [63]. Since the reduced mass is $\mu^{-1} = 1/m_{\text{Ga}} + 1/m_{\text{N}}$, the vibrations of the polar modes are mainly due to the nitrogen oscillations. However, the isotope shifts of the non-polar modes E_2^1 and E_2^2 were found to deviate from the expected reduced mass behavior, with significant deviation found for the E_2^1 which seems not to be affected by the isotopic mass. The model calculations used to explain the vibrational dynamics of the non-polar modes led the authors to conclude that although the E_2^2 mode is still dominated by nitrogen atom vibrations, it constitutes only 92% of the total vibrations. The rest of the 8% vibrations in the admixture are due to the movements of the Ga atoms. A different scenario was inferred for the E_2^1 mode; its vibration mostly involves the motion of Ga which explains the lack of frequency response to the isotope mass of the ^{15}N . Thus, Zhang's studies indicated that all of the Raman modes but the E_2^1 involve the vibrations of the nitrogen atoms, while that of the E_2^1 involves the vibrations of the heavier gallium atoms [63].

One crucial aspect impacting device performance is phonon interaction with free carriers. In general, the interaction can degrade the viability of the device; however, studies have also demonstrated that the phonon-electron interaction may be used to engineer certain laser devices [64-66]. The phonon lifetimes are important in both these aspects, and although the interaction involves only the *LO* phonons, knowledge of other mode-lifetimes may give insight into the

characteristic dynamics of the material. One fundamental lifetime shortening mechanism in semiconductors has been established to occur via the anharmonic interaction [67-72]. In this mechanism, the Raman phonons decay into other normal modes in such a way that there is a conservation of momentum and energy in the process. More specifically, for a three-phonon decay process a phonon of frequency ω_1 and a wavevector \mathbf{q}_1 decays into two phonons of energies ω_2 , ω_3 , and wavevectors \mathbf{q}_2 , \mathbf{q}_3 , such that $\omega_1 = \omega_2 + \omega_3$ and $\mathbf{q}_1 = \mathbf{q}_2 + \mathbf{q}_3$. However, the additional lifetime shortening mechanism due to phonon scattering at point defects has to be considered as well [67].

Tsen et al. have reported phonon lifetime measurements via Raman spectroscopy [73]. In their investigation, the decay of the $A_1(LO)$ mode in WZ-GaN film was studied via time-resolved Raman spectroscopy. The measured lifetime was found to be ≈ 3 ps at 300 K and ≈ 5 ps at 5K. Tsen et al. hypothesized that the zone-center $A_1(LO)$ phonons decay primarily into a large wavevector TO phonon and a large wavevector LA or TA phonon. [73].

Raman studies of phonon lifetimes in GaN, AlN, and ZnO crystallites have been reported by Bergman et al. [27]. The lifetimes were obtained from the Raman linewidth, after correcting for the instrument broadening, using the uncertainty relation $\frac{\Delta E}{\hbar} = \frac{1}{\tau}$, where ΔE is the linewidth and τ is the lifetime [74]. The lifetime analysis of Bergman et al. indicated that the phonon lifetimes in AlN, GaN, as well as ZnO crystallites fall into two main time regimes: a relatively long lifetime of the E_2^1 mode and much shorter lifetimes for the E_2^2 , $E_1(TO)$, $A_1(TO)$, and $A_1(LO)$ modes. The lifetime of the E_2^1 mode of high quality GaN crystallites was found to be ≈ 10 ps, whereas the lifetimes of the other modes were found to be approximately an order of magnitude shorter. A similar trend in the lifetimes was observed for phonons of high quality AlN, ZnO, and AlN that

contain high levels of impurities. Moreover, the lifetimes of all the modes of both the high and low quality AlN crystallites were found to be correlated to their relative impurity concentrations [27].

A tentative explanation of the relative long lifetime of the E_2^1 in the WZ-crystallites was given by Bergman et al. in terms of the factors determining the anharmonic lifetimes, specifically the energy-conservation constraints, the density of the final states, as well as the anharmonic interaction coefficient. Unlike the other modes, the energy of the E_2^1 mode lies in the low energy regime of the wurtzite dispersion curve [75-77] and only the acoustic phonons are available as a channel of decay. At the zone edges the energies of the acoustic phonons are equal or larger than that of the E_2^1 mode; thus, in order for the energy conservation to hold the optical phonons have to decay into acoustic phonons at the zone-center for which their density is low. Although the contribution of the anharmonic coefficient, which has not yet been determined theoretically, has to be taken into account, the authors have suggested that the low density of states significantly reduces the scattering rate, thus increasing the phonon lifetime.

8. Wide Band-Gap Alloys

In the following, a review of the mode behavior of III-V nitride-based alloys is presented. Mixed crystals of the form $AB_{1-x}C_x$ are classified into two main groups according to the behavior of the $q \approx 0$ optical phonons [78]. Figure 24 depicts the two classes for ZB material, referred to as the one-mode and two-mode material, respectively [79]. In general, if the frequencies of the AB and the AC components differ greatly, a two-mode behavior is expected; if the frequencies of both components have proximate values, a one-mode behavior results. In addition to the one-mode and two-mode classes of materials, an intermediate class exists that exhibits two-mode behavior over a

The polar phonon in III-V ternary nitride semiconductors of wurtzite structure were investigated theoretically by Yu et al. [86]. Within the modified-random-element isodisplacement model (MREI), they demonstrated that the polar modes of $\text{Ga}_x\text{Al}_{1-x}\text{N}$ and $\text{In}_x\text{Ga}_{1-x}\text{N}$ follow a one-mode behavior [86]. The MREI model in [86] is based on the model developed previously for the ZB materials with the modifications that include the additional phonon modes and the anisotropy of the WZ structure. Figures 25 and 26 present the theoretical results and some of the compiled experimental results. As can be seen in Fig. 25, the theory concurs well with the experiment except for the $E_1(\text{TO})$ mode. This small deviation has been attributed to crystal quality. The one-mode behavior found by Yu et al. was explained in terms of the large mass difference between the nitrogen and the other alloy constituents. Since the atomic mass of nitrogen is much smaller than that of gallium, indium, and aluminum, the reduced masses of GaN, InN, and AlN are almost the same as that of nitrogen. As a result, no distinct GaN-like modes and AlN-like modes may exist in the $\text{Ga}_x\text{Al}_{1-x}\text{N}$ alloy system; the same situation holds for the $\text{In}_x\text{Ga}_{1-x}\text{N}$ alloy [86]. It should be noted that in all of the aforementioned experimental results the other possible factors affecting the line position such as stress, phonon-plasmon coupling, and symmetry mixing were not taken into consideration.

Raman studies on phonon mode behavior in ZB-AlGaN films were reported by Harima et al. [15]. It was found that the *LO* mode is a one-mode type while the *TO* mode is a two-mode type. The authors calculated the mode behavior for the ZB-AlGaN alloy system and found it to be consistent with the experimental results. Figure 27 presents the phonon frequency versus the composition for the experimental as well as the calculated results [15].

The topic of ordering in the AlGaN alloy system was addressed by Korakakis et al., utilizing X-ray diffraction [87], and by Bergman et al., utilizing Raman and X-ray spectroscopy [88]. The

films in the former study were grown by MBE at a temperature of $\approx 750^\circ\text{C}$ on SiC and sapphire substrates. The ordering in the films was inferred from the superlattice (SL) lines of the (0001), (0003), and (0005) diffraction [87]. These lines are forbidden reflections in WZ structure and appear as SL lines only when lattice ordering exists. The intensity ratio of the SL line to the allowed (0002) line of the WZ structure is thus a measure of the extent of the order. The X-ray analysis of Korakakis indicated a long-range order; the relative intensity of SL lines was found to be strong. In contrast to these results the AlGa_xN films, which were grown via MOCVD at the elevated temperature range $\approx 1100^\circ\text{C}$ and which have been investigated by Bergman et al., were found to exhibit a much smaller intensity ratio thus implying a disordered state of the alloy [88]. The different order states found in both studies may be attributed to the temperature employed in growth, since it has been demonstrated that the achievement of an ordered alloy in some families of ternary tetrahedral semiconductors is a function of the growth temperature [89].

The influence of the disorder on the E_2^2 Raman mode of the Al_xGa_{1-x}N MOCVD films in the composition range $0 < x < 1$ has been investigated as well by Bergman et al. [88]. Figure 28 presents the Raman spectra of the E_2^2 mode at various alloy compositions; it is shown that the spectral lines exhibit asymmetric broadening toward the higher frequency range. The asymmetry of the E_2^2 lines was explained in light of the spatial correlation model [90-92]. The foundation of the model lies in the wave vector uncertainty: $\Delta q = 2\pi/L$. In that relation Δq is the phonon wavevector range; this range is due to the relaxation of the $q = 0$ Raman selection rules caused by the disorder. The parameter L may be regarded as the size of the embedded ordered domain in the disordered matrix: thus the larger the disorder, the smaller the ordered domain. The model may be expressed as [90-92]

$$I(\omega) \propto \int \exp(-q^2 L^2 / 4) \frac{d^3 q}{[\omega - \omega(\mathbf{q})]^2 + [\Gamma_0 / 2]^2}. \quad (15)$$

In this relation Γ_0 is the linewidth of the alloy of composition $x = 0$ and $\omega(\mathbf{q})$ is the phonon dispersion curve. Few and to some extent conflicting theoretical predictions of the dispersion relation in the III-V nitrides semiconductors have been reported [75, 76, 93-99]. Moreover, due to the lack of experimental results no consensus has been reached regarding the phonon dispersion relations in these materials. In order to fit the Raman data to the model, the authors in [88] assumed an averaged value of $\omega(\mathbf{q})$ of the form $A+Bq^2$ (in units of cm^{-1} and with $A=568$ and $B=100$). As can be seen in Fig. 28, the Raman data for the $x = 0.12$ and $x = 0.22$ can be fit with this model (represented by the solid lines), albeit with different values for Γ . These fits suggest an estimate $L \approx 3.5$ nm for the size of the embedded ordered domain [88]. Figure 29 shows the E_2^2 Raman linewidth as a function of composition; a maximum is observed at composition $x \approx 0.5$, a value at which maximum disorder would be expected in a random alloy.

9. Concluding Remarks

The Raman effect arises from the interaction of light with matter; as such, Raman spectroscopy is a nondestructive and powerful tool in the study of lattice dynamics. The various investigations reviewed here demonstrate the utility of Raman spectroscopy in characterizing the material properties of the III-V nitrides. Although significant progress has been made many issues are still in the initial stages of research. The cubic phases, the InN and its alloy system, and the deconvolution of the combined phonon dynamics effect on the alloy Raman spectra merit closer investigation. Moreover, the topic of Raman spectroscopy of phonon-interfaces and phonon-

superlattices needs to be addressed. The successful investigation of many of the above issues is contingent on advances in material quality of the wide band-gap semiconductors.

Acknowledgments

Leah Bergman acknowledges the US Army Research Office for supporting this work.

References

1. J.W. Orton, C.T. Foxon: Rep. Prog. Phys. **61**, 1 (1998).
2. H. Morkoc, S. Strite, G.B. Gao, M.E. Lin, B. Sverdlov, M. Burns: J. Appl. Phys. **76**, 1363 (1994).
3. J.H. Edgar: J. Mater. Res. **7**, 235 (1992).
4. J.H. Edgar (ed.), *Properties of Group III Nitrides* (INSPEC, London, 1994).
5. R.F. Davis: Proc. IEEE **79**, 702 (1991).
6. M. Cardona: *In Light Scattering in Solids I*, M. Cardona (ed.) (Springer-Verlag, New York, 1983) p. 1.
7. D. Behr, J. Wagener, J. Schneider, H. Amano, I. Akasaki: Appl. Phys. Lett. **68**, 2404 (1996).
8. M. Ramsteiner, J. Menniger, O. Brandt, H. Yang, K.H. Ploog: Appl. Phys. Lett. **69**, 1276 (1996).
9. M. Kuball, F. Demangeot, J. Frandon, M.A. Renucci, H. Sands, D.N. Batchelder, S. Clur, O. Briot: Appl. Phys. Lett. **74**, 549 (1999).
10. H. Okumura: In *Gallium Nitride and Related Semiconductors*, J.H. Edgar, S. Strite, I. Akasaki, H. Amano, C. Wetzel (ed.) (INSPEC, London, 1999) p. 402.
11. Y. Takeda, M. Tabuchi: In *Gallium Nitride and Related Semiconductors*, J.H. Edgar, S. Strite, I. Akasaki, H. Amano, C. Wetzel (ed.) (INSPEC, London, 1999) p. 381.
12. A.D. Hanser, R.F. Davis: In *Gallium Nitride and Related Semiconductors*, J.H. Edgar, S. Strite, I. Akasaki, H. Amano, C. Wetzel (ed.) (INSPEC, London, 1999) p. 386.
13. P. Lawaetz: Phys. Rev. B **5**, 4039 (1972).

14. A. Tabata, R. Enderlein, J.R. Leite, S.W. da Silva, J.C. Galzerani, D. Schikora, M. Kloidt, K. Lischka: J. Appl. Phys. **79**, 4137 (1996).
15. H. Harima, T. Inoue, S. Nakashima, H. Okumura, Y. Ishida, S. Yoshida, T. Koizumi, H. Grille, F. Bechstedt: Appl. Phys. Lett **74**, 191 (1999).
16. S. Miyoshi, K. Onabe, N. Ohkouchi, H. Yaguchi, R. Ito, S. Fukatsu, Y. Shiraki: J. Cryst. Growth **124**, 439 (1992).
17. M. Giehler, M. Ramsteiner, O. Brandt, H. Yang, K.H. Ploog: Appl. Phys. Lett. **67**, 733 (1995).
18. W. Hayes, R. Loudon: *Scattering of Light by Crystals* (John Wiley & Sons, New York, 1978).
19. I. Gorczyca, N.E. Christensen, E.L. Peltzer, Y. Blanca, C.O. Rodriguez: Phys. Rev. B **51**, 11936 (1995).
20. F.H. Pollak: In *Analytical Raman Spectroscopy*, J.G. Grasselli, B.J. Bulkin (ed.) (John Wiley & Sons, New York, 1991) pp. 137-221.
21. D.D. Manchon, A.S. Barker, P.J. Dean, R.B. Zetterstrom: Solid State Commun. **8**, 1227-31 (1970).
22. V. Lemos, C.A. Arguello, R.C.C. Leite: Solid State Commun. **11**, 1352 (1972).
23. G. Burns, F. Dacol, J.C. Marinace, B.A. Scott: Appl. Phys. Lett. **22**, 356 (1973).
24. S. Murugkar, R. Merlin, A. Botchkarev, A. Salvador, H. Morkoc: J. Appl. Phys. **77**, 6042 (1995).
25. A. Cingolani, M. Ferrara, M. Lugara, G. Scamarcio: Solid State Commun. **58**, 823 (1986).
26. T. Azuhata, T. Sota, K. Suzuki, S. Nakamura: J. Phys.: Condens. Matter **7**, L129 (1995).
27. L. Bergman, D. Alexson, P.L. Murphy, R.J. Nemanich, M. Dutta, M.A. Stroscio, C. Balkas, H. Shin, R.F. Davis: Phys. Rev. B **59**, 12977 (1999).
28. H. Siegle, I. Eckey, A. Hofmann, C. Thomsen: Solid State Commun. **96**, 943 (1995).
29. J.L. Birman: Phys. Rev. **115**, 1493 (1959).
30. P. Perlin, A. Polian, T. Suski: Phys. Rev. B **47**, 2874 (1993).

31. L.E. McNeil, M. Grimsditch, R.H. French: J. Am. Ceram. Soc. **76**, 1132 (1993).
32. L. Filippidis, H. Siegle, A. Hoffmann, C. Thomsen, K. Karch, F. Bechstedt: Phys. Stat. Sol. B **198**, 621 (1996).
33. H.J. Kwon, Y.H. Lee, O. Miki, H. Yamano, A. Yoshida: Appl. Phys. Lett. **69**, 937 (1996).
34. M.C. Lee, H.C. Lin, Y.C. Pan, C.K. Shu, J. Ou, W.H. Chen, W.K. Chen: Appl. Phys. Lett. **73**, 2606 (1998).
35. S.P.S. Porto: In *Light Scattering Spectra of Solids*, G.B. Wright (ed.) (New York, 1969) p. 1.
36. N.W. Ashcroft, N.D. Mermin: Solid State Physics (Holt, Rinehart and Winston, New York, 1976).
37. A.S. Barker Jr., M. Ilegems: Phys. Rev. B **7**, 743 (1973).
38. P. Perlin, C.J. Carillon, J.P. Itie, A.S. Miguel, I. Grzegory, A. Polian: Phys. Rev. B **45**, 83 (1992).
39. V.Y. Davydov, N.S. Averkiev, I.N. Goncharuk, D.K. Nelson, I.P. Nikitina, A.S. Polkovnikov, A.N. Smirnov, M.A. Jacobson: J. Appl. Phys. **82**, 5097 (1997).
40. C. Kisielowski, J. Krüger, S. Ruvimov, T. Suski, J.W. Ager III, E. Jones, Z. Liliental-Weber, M. Rubin, E.R. Weber, M.D. Bremser, R.F. Davis: Phys. Rev. B **54**, 17745 (1996).
41. J.F. Nye: *Physical Properties of Crystals* (Clarendon Press, Oxford, 1984).
42. W.J. Meng, T.A. Perry: J. Appl. Phys. **76**, 7824 (1994).
43. W. Rieger, T. Metzger, H. Angerer, R. Dimitrov, O. Ambacher, M. Stutzmann: Appl. Phys. Lett. **68**, 970 (1996).
44. H. Siegle, A. Hoffmann, L. Eckey, C. Thomsen, J. Christen, F. Bertram, D. Schmidt, D. Rudloff, K. Hiramatsu: Appl. Phys. Lett. **71**, 2490 (1997).
45. T. Kozawa, T. Kachi, H. Kano, H. Nagase, N. Koide, K. Manabe: J. Appl. Phys. **77**, 4389 (1995).
46. J.A. Sanjurjo, E.L. Cruz, P. Vogl, M. Cardona: Phys. Rev. B **28**, 4579 (1983).
47. S.S. Mitra, O. Brafman, W.B. Daniels, R.K. Crawford: Phys. Rev. **186**, 942 (1969).
48. R. Loudon: Advances in Physics **13**, 423 (1964).

49. L. Bergman, M. Dutta, C. Balkas, R.F. Davis, J.A. Christman, D. Alexson, R.J. Nemanich: J. Appl. Phys. **85**, 3535 (1999).
50. C.A. Arguello, D.L. Rousseau, S.P.S. Porto: Phys. Rev. **181**, 1351 (1969).
51. T. Kozawa, T. Kachi, H. Kano, Y. Taga, M. Hashimoto, N. Koide, K. Manabe: J. Appl. Phys. **75**, 1098 (1994).
52. B.B. Varga: Phys. Rev. **137**, 1896 (1965).
53. M. Ramsteiner, O. Brandt, K.H. Ploog: Phys. Rev. B **58**, 1118 (1998).
54. D. Kirillov, H. Lee, J.S. Harris: J. Appl. Phys. **80**, 4058 (1996).
55. F. Demangeot, J. Frandon, M.A. Renucci, C. Meny, O. Briot, R.L. Aulombard: J. Appl. Phys. **82**, 1305 (1997).
56. F.A. Ponce, J.W. Steeds, C.D. Dyer, G.D. Pitt: Appl. Phys. Lett. **69**, 2650 (1996).
57. C. Wetzel, W. Walukiewicz, E.E. Haller, J. Ager III, I. Grzegory, S. Porowski, T. Suski: Phys. Rev. B **53**, 1322 (1996).
58. G. Popovici, G.Y. Xu, A. Botchkarev, W. Kim, H. Tang, A. Salvador, H. Morkoc, R. Strange, J.O. White: J. Appl. Phys. **82**, 4020 (1997).
59. E. Burstein, A. Pinczuk, S. Iwasa: Phys. Rev. **157**, 611 (1967).
60. M.V. Klein, B.N. Ganguly, P.J. Colwell: Phys. Rev. B **6**, 2380 (1972).
61. D.T. Hon, W.L. Faust: Appl. Phys. **1**, 241 (1973).
62. G. Irmer, V.V. Toporov, B.H. Bairamov, J. Monecke: Phys. Stat. Sol. B **119**, 595 (1983).
63. J.M. Zhang, T. Ruf, M. Cardona, O. Ambacher, M. Stutzmann, J.M. Wagner, F. Bechstedt: Phys. Rev. B. **56**, 14399 (1997).
64. M.V. Kisin, V.B. Gorfinkel, M.A. Stroschio, G. Belenky, S. Luryi: J. Appl. Phys. **82**, 2031 (1997).
65. H.B. Teng, J.P. Sun, G.I. Haddad, M.A. Stroschio, S.G. Yo, K.W. Kim: J. Appl. Phys. **84**, 2155 (1998).
66. M.A. Stroschio: J. Appl. Phys. **80**, 6864 (1996).

67. P.G. Klemens: In *Solid State Physics; Advances in Research and Applications*, F. Seitz, D. Turnbull (ed.) (Academic Press Inc., New York, 1958), vol. 7, pp. 1-98.
68. P.G. Klemens: Phys. Rev. **148**, 845 (1966).
69. W.J. Borer, S.S. Mitra, K.V. Namjoshi: Solid State Commun. **9**, 1377 (1971).
70. A. Debernardi: Phys. Rev. B **57**, 12847 (1998).
71. J. Menéndez, M. Cardona: Phys. Rev. B **29**, 2051 (1984).
72. B.K. Ridley: J. Phys.: Condens. Matter **8**, L511 (1996).
73. K.T. Tsen, D.K. Ferry, A. Botchkarev, B. Sverdlov, A. Salvador, H. Morkoc: Appl. Phys. Lett. **72**, 2132 (1998).
74. B. Di Bartolo: *Optical Interactions in Solids* (John Wiley & Sons, Inc., New York, 1969).
75. J.C. Nipko, C.K. Loong, C.M. Balkas, R.F. Davis: Appl. Phys. Lett. **73**, 34 (1998).
76. J.C. Nipko, C.K. Loong: Phys. Rev. B **57**, 10550 (1998).
77. A.W. Hewat: Solid State Commun. **8**, 187 (1970).
78. I.F. Chang, S.S. Mitra: Phys. Rev. **172**, 924 (1968).
79. L. Bergman, R.J. Nemanich: Ann. Rev. Mater. Sci. **26**, 551 (1996).
80. G. Lucovsky, M.F. Chen: Solid State Commun. **8**, 1397 (1970).
81. K. Hayashi, K. Itoh, N. Sawaki, I. Akasaki: Solid State Commun. **77**, 115 (1991).
82. D. Behr, R. Niebuhr, J. Wagner, K.H. Bachem, U. Kaufmann: Appl. Phys. Lett. **70**, 363 (1997).
83. A. Cros, H. Angerer, O. Ambacher, M. Stutzmann, R. Hopler, T. Metzger: Solid State Commun. **104**, 35 (1997).
84. F. Demangeot, J. Groenen, J. Frandon, M.A. Renucci, O. Briot, S. Clur, R.L. Aulombard: Appl. Phys. Lett. **72**, 2674 (1998).
85. P. Wisniewski, W. Knap, J. P. Malzac, J. Camassel, M.D. Bremser, R.F. Davis, T. Suski: Appl. Phys. Lett. **73**, 1760 (1998).

86. S. Yu, K. W. Kim, L. Bergman, M. Duttá, M.A. Strosio, J.M. Zavada: Phys. Rev. B **58**, 15283 (1998).
87. D. Korakakis, K.F. Ludwig, T.D. Moustakas: Appl. Phys. Lett. **71**, 72 (1997).
88. L. Bergman, M.D. Bremser, W.G. Perry, R.F. Davis, M. Dutta, R.J. Nemanich: Appl. Phys. Lett. **71**, 2157 (1997).
89. A. Zunger: Appl. Phys. Lett. **50**, 164 (1987).
90. P. Parayanthal, F.H. Pollak: Phys. Rev. Lett. **52**, 1822 (1984).
91. R.J. Nemanich, S.A. Solin, R.M. Martin: Phys. Rev. B **23**, 6348 (1981).
92. P.M. Fauchet, I.H. Campbell: Critical Reviews in Solid State and Materials Sciences **14**, S79 (1988).
93. T. Azuhata, T. Matsunaga, K. Shimada, K. Yoshida, T. Sota, K. Suzuki, S. Nakamura: Physica B **219-220**, 493 (1996).
94. V.Y. Davydov, Y.E. Kitaev, I.N. Goncharuk, A.N. Smirnov, J. Graul, O. Semchinova, D. Uffmann, M.B. Smirnov, A.P. Mirgorodsky, R.A. Evarestov: Phys. Rev. B **58**, 12899 (1998).
95. K. Karch, F. Bechstedt, P. Pavone, D. Strauch: Physica B **219-220**, 445 (1996).
96. K. Karch, F. Bechstedt: Phys. Rev. B **56**, 7404 (1997).
97. K. Karch, J.M. Wagner, F. Bechstedt: Phys. Rev. B **57**, 7043 (1998).
98. K. Miwa, A. Fukumoto: Phys. Rev. B **48**, 7897 (1993).
99. H. Siegle, G. Kaczmarczyk, L. Filippidis, A.P. Litvinchuk, A. Hoffmann, C. Thomsen, Phys. Rev. B **55**, 7000 (1997).

Figure Captions

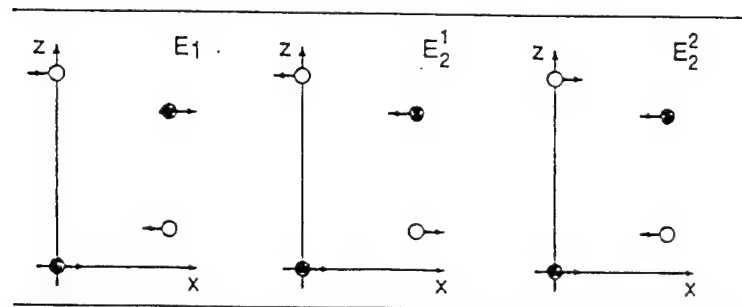
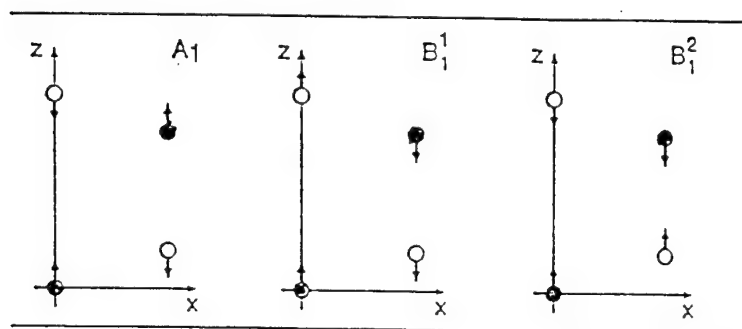
- Fig. 1. Optical phonon modes in the wurtzite structure. The Raman active modes are the polar A_1 and E_1 , and the two non-polar E_2 modes. The B_1 modes are silent [19].
- Fig. 2. Schematic phonon dispersions for the ZB and the WZ structures. The phonon curves: TA , LA , TO , and LO of the ZB are along the Γ -L [111] direction (*thick lines*). The folding (*thin lines*) of these curves into the WZ Brillouin zone Γ -A [0001] direction creates the: E_2^1 from the TA , B_1^1 from the LA , E_2^2 from TO and B_1^2 from LO . The splitting (*dashed lines*) creates the $A_1(TO)$ and the $E_1(TO)$ from the original TO as well as the $A_1(LO)$ and the $E_1(LO)$ from the original LO .
- Fig. 3. Polarized Raman spectra of GaN film in the y-direction backscattering geometry; the GaN modes are present as well as the sapphire substrate modes [26].
- Fig. 4. Polarized Raman spectra of GaN for the z-direction back-scattering Raman configuration [26].
- Fig. 5. Depolarized Raman spectra of GaN films grown on GaAs substrates. Sample A is mainly WZ, sample C is mainly ZB, and sample B is a mixed phase structure [17].
- Fig. 6. Raman spectra of WZ-GaN film at three incident laser wavelengths: (a) 514.5 nm, (b) 488 nm, and (c) 457.9 nm [14].
- Fig. 7. Raman spectra of the ZB-GaN film at the three incident laser wavelengths as in Fig. 6 [14].
- Fig. 8. Raman spectra and the curve fit to the spectra of AlN crystallite [27].
- Fig. 9. Compositional variation of the TO-Raman mode of ZB-AlGa_N alloy. The phonon frequency of the ZB-AlN is 655 cm⁻¹ [15].
- Fig. 10. LO phonon spectra of ZB-AlGa_N alloy. The LO mode of the ZB-AlN is observed at 902 cm⁻¹ [15].
- Fig. 11. Model calculations (*lines*) of the high frequency phonon of WZ-AlN and GaN under hydrostatic pressure. The *dots* represent experimental data from [30, 38, 19].
- Fig. 12. Model calculations (*lines*) of the low frequency phonons of WZ-AlN and GaN under hydrostatic pressure. The *dots* represent experimental data from [30, 38, 19].
- Fig. 13. Raman frequency scheme for (a) the case when the long range electrostatic field is the dominant interaction, and (b) when the anisotropy of the short range interaction dominates [49].

- Fig. 14. Geometry of the Raman experiment setup for the observation of the quasi-modes. The spectra were acquired in a backscattering geometry from the Y axis, θ is the rotation angle, and β is the angle of the phonon propagation [49].
- Fig. 15. Raman spectra at various rotations and Raman configuration which enable the observation of the quasi- TO modes. The pure-modes: E_2^2 , and $E_1(TO)$ are present as well [49].
- Fig. 16. Raman spectra of the quasi- LO modes of an AlN crystallite [49].
- Fig. 17. Angular dispersion of the quasi- LO and $-TO$ modes. The *lines* represent Loudon's model; the *dots* and X 's are the experimental results from [49] and [32], respectively [49].
- Fig. 18. Raman spectra of the $A_1(LO)$ mode of GaN at several Si doping concentrations n_H obtained via Hall measurements [51].
- Fig. 19. Experimental and calculated Raman lineshape of the $A_1(LO)$ -plasmon coupled mode [51].
- Fig. 20. Correlation between the carrier concentration n found from the Raman analysis and the concentration n_H obtained via Hall measurements [51].
- Fig. 21. Raman spectra of highly conductive GaN films. *Dotted line*: spectra from sample with free carrier density $n = 4 \times 10^{19} \text{ cm}^{-3}$; *solid line*: from sample with $n = 8 \times 10^{19} \text{ cm}^{-3}$ [54].
- Fig. 22. Calculated spectra of the coupled plasmon-phonon modes for a sample with $n = 4 \times 10^{19} \text{ cm}^{-3}$. The *dotted line* corresponds to a plasma damping constant of 100 cm^{-1} ; the *solid line* to 1116 cm^{-1} , which is a realistic value for the GaN film [54].
- Fig. 23. Experimental and calculated (*dotted line*) lineshape of the low-branch $A_1(LO)$ phonon-plasmon coupled mode in GaN films [55].
- Fig. 24. The two classes of mixed ZB crystals: (a) two-mode type and (b) one-mode type material [79].
- Fig. 25. Phonon mode behavior of WZ-GaAlN alloy. The *lines* represent the MREI model. The model calculations are for the $A_1(TO)$, $A_1(LO)$, $E_1(TO)$, and $E_1(LO)$ modes; the *points* represent the experimental data [86].
- Fig. 26. Phonon mode behavior of WZ-InGaN alloy. Theory (*lines*) and experiment (*dots*). The polar modes are presented [86].
- Fig. 27. Mode behavior of ZB-AlGaIn. For an intermediate composition x in the two-mode class of materials, two sets of frequencies would be observed in the spectra: one set is due to

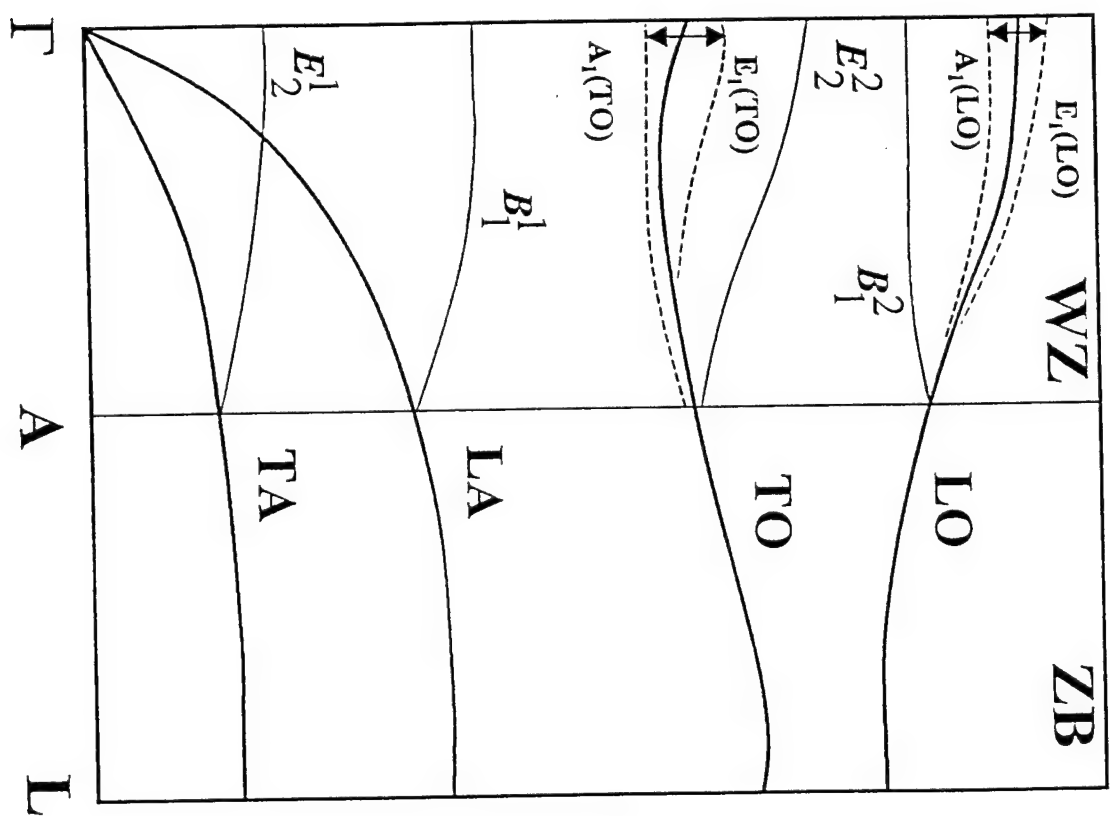
the *LO* and *TO* modes of the AB component and the other set is due to the *LO* and *TO* modes of the AC component. The one-mode exhibits only one set of *LO* and *TO* frequencies, which ideally are linear with composition [15].

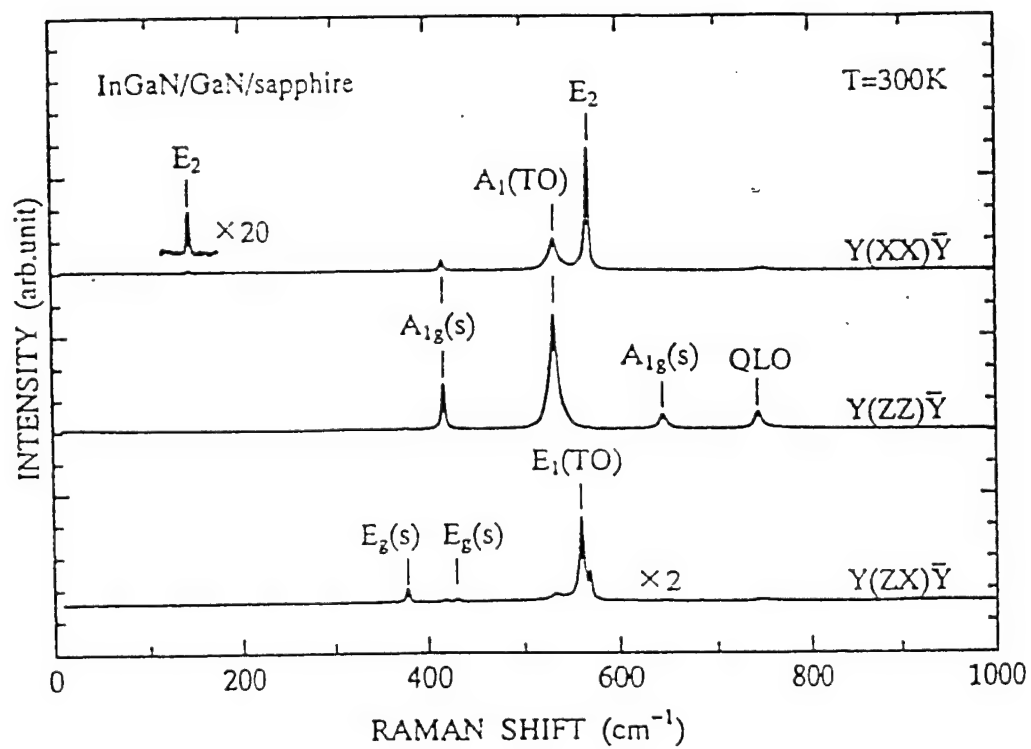
Fig. 28. Raman spectra of the E_2^2 mode of WZ-AlGa_xN films at various compositions. The *solid lines* represent the spatial correlation model [88].

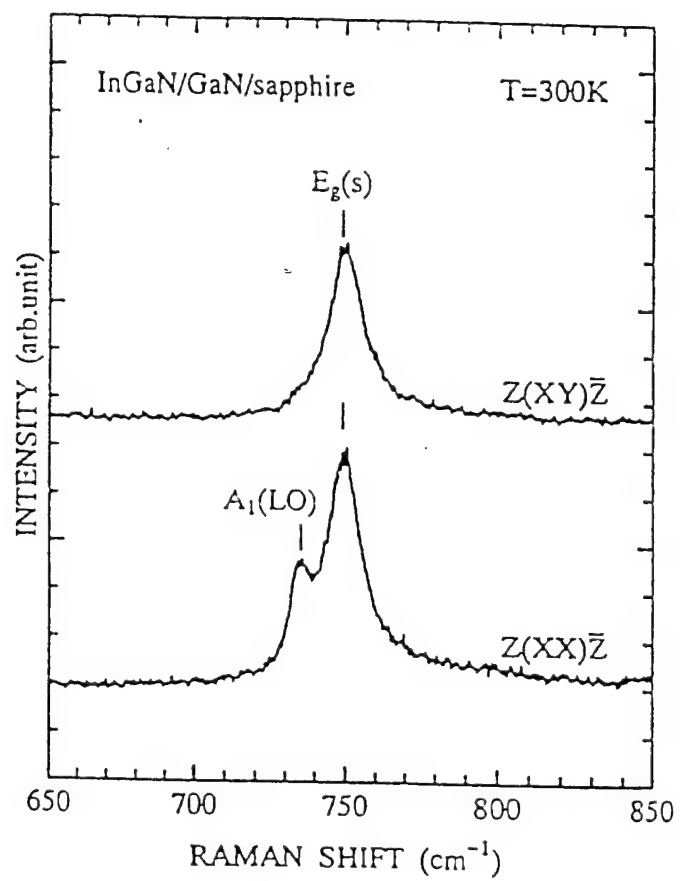
Fig. 29. The E_2^2 Raman linewidth as a function of composition (*dots*). The *solid line* is obtained from calculations of the entropy of mixing of an alloy system (in arbitrary units) [88].

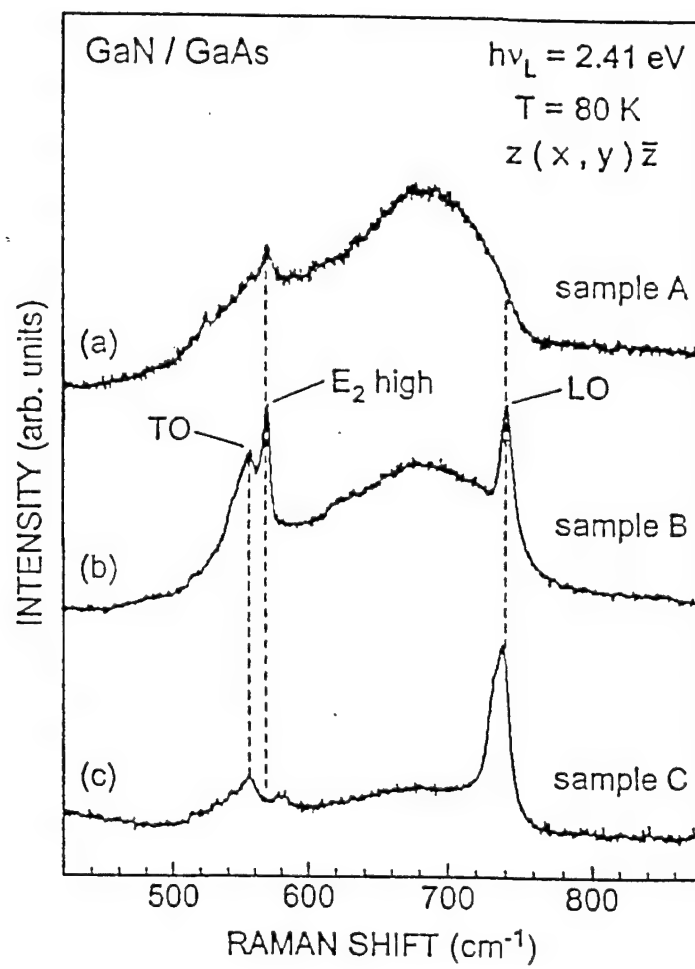


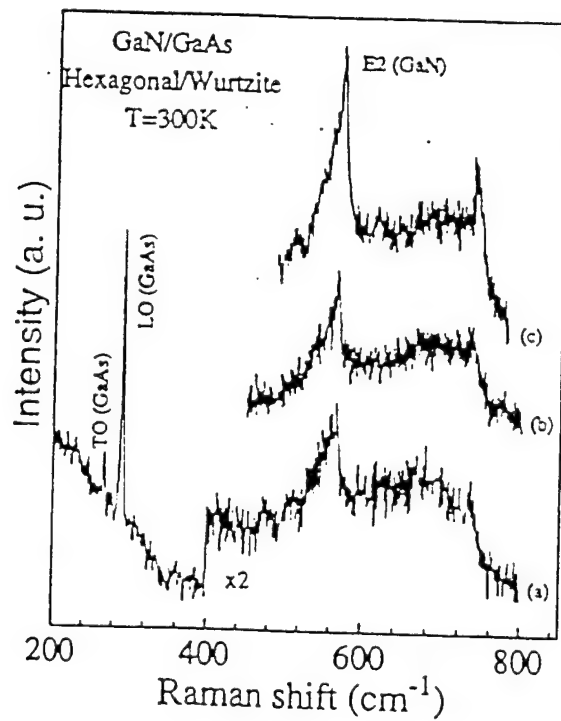
Phonon Frequency

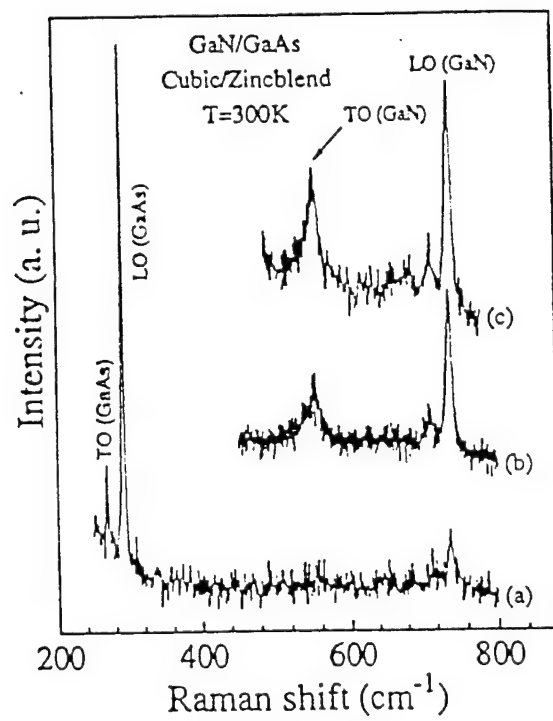




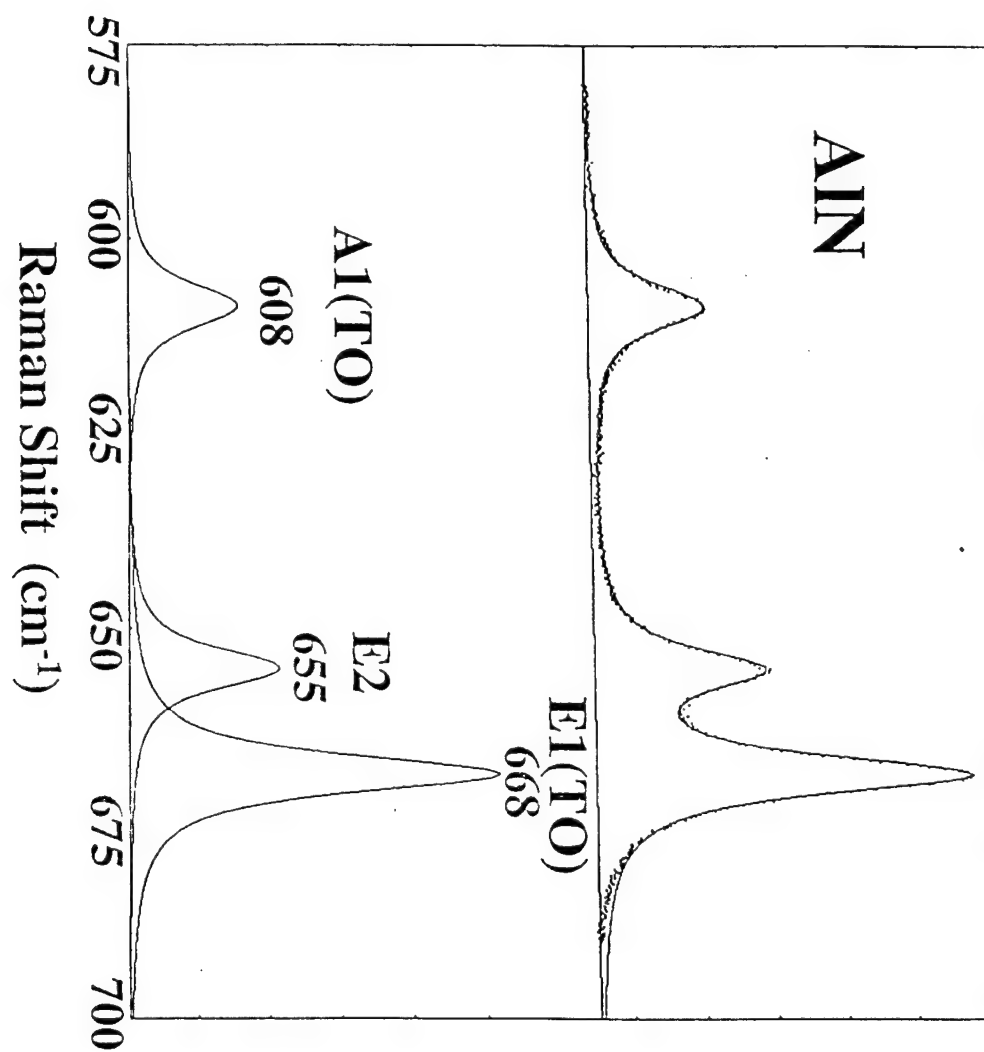


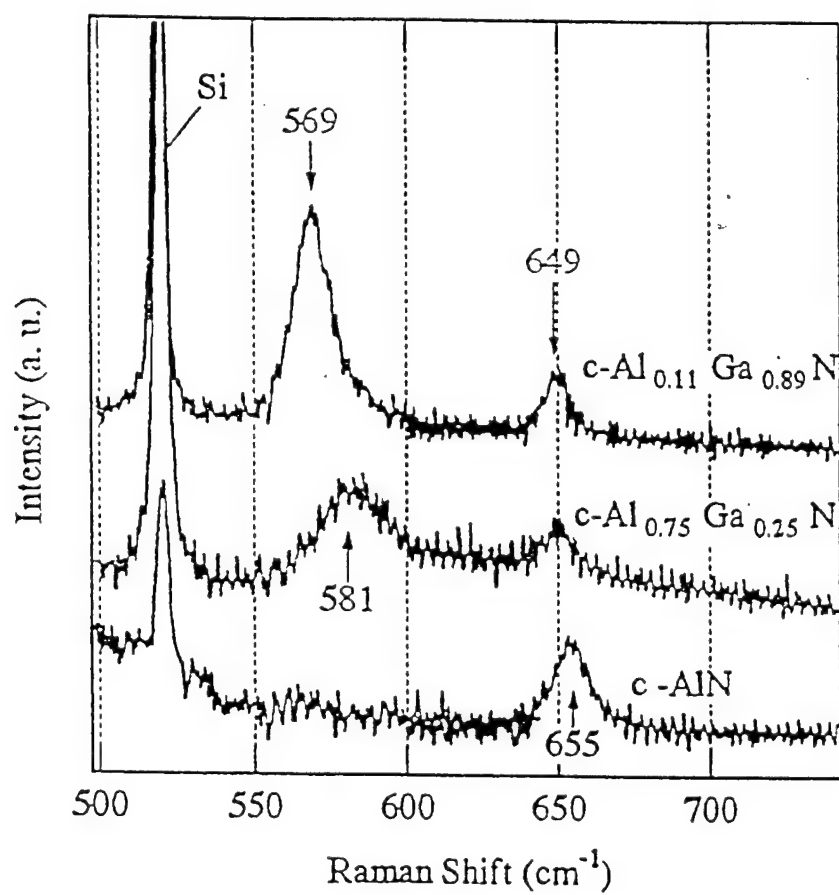


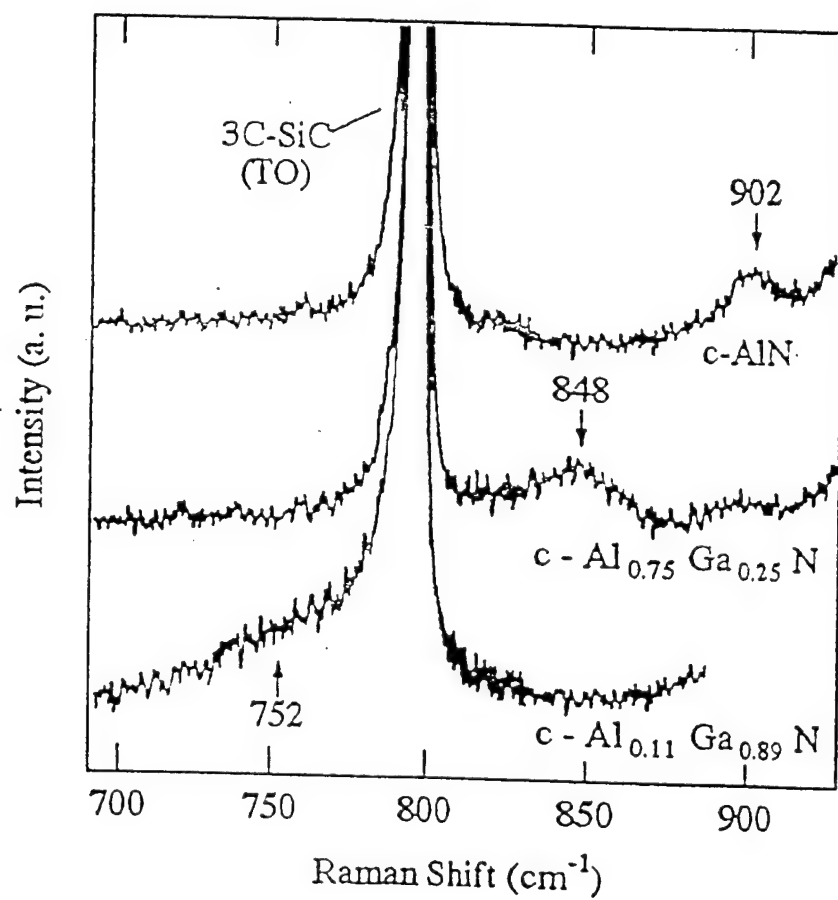


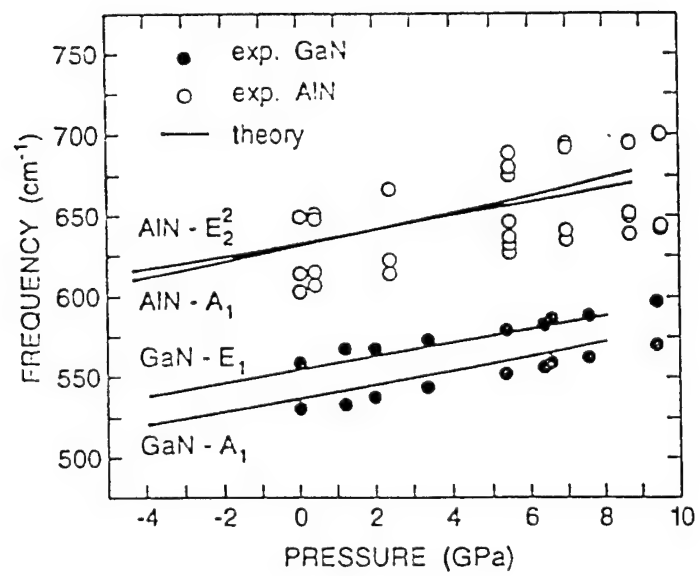


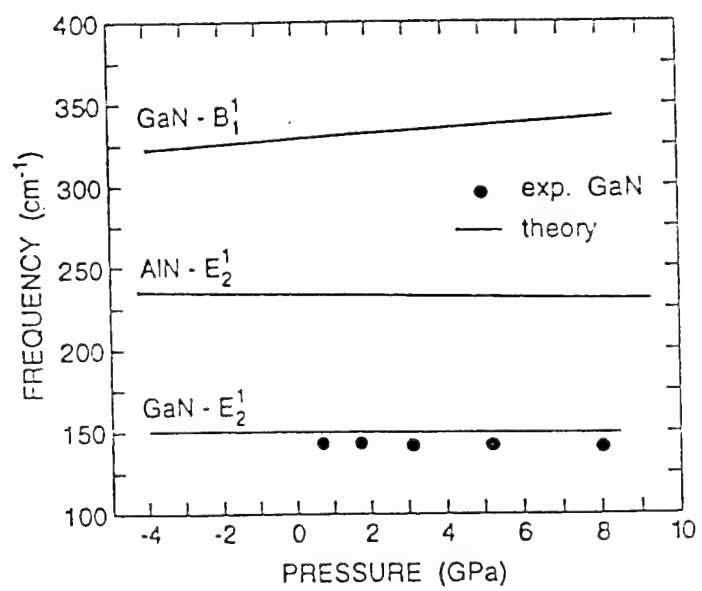
Raman Intensity (arb. Units)

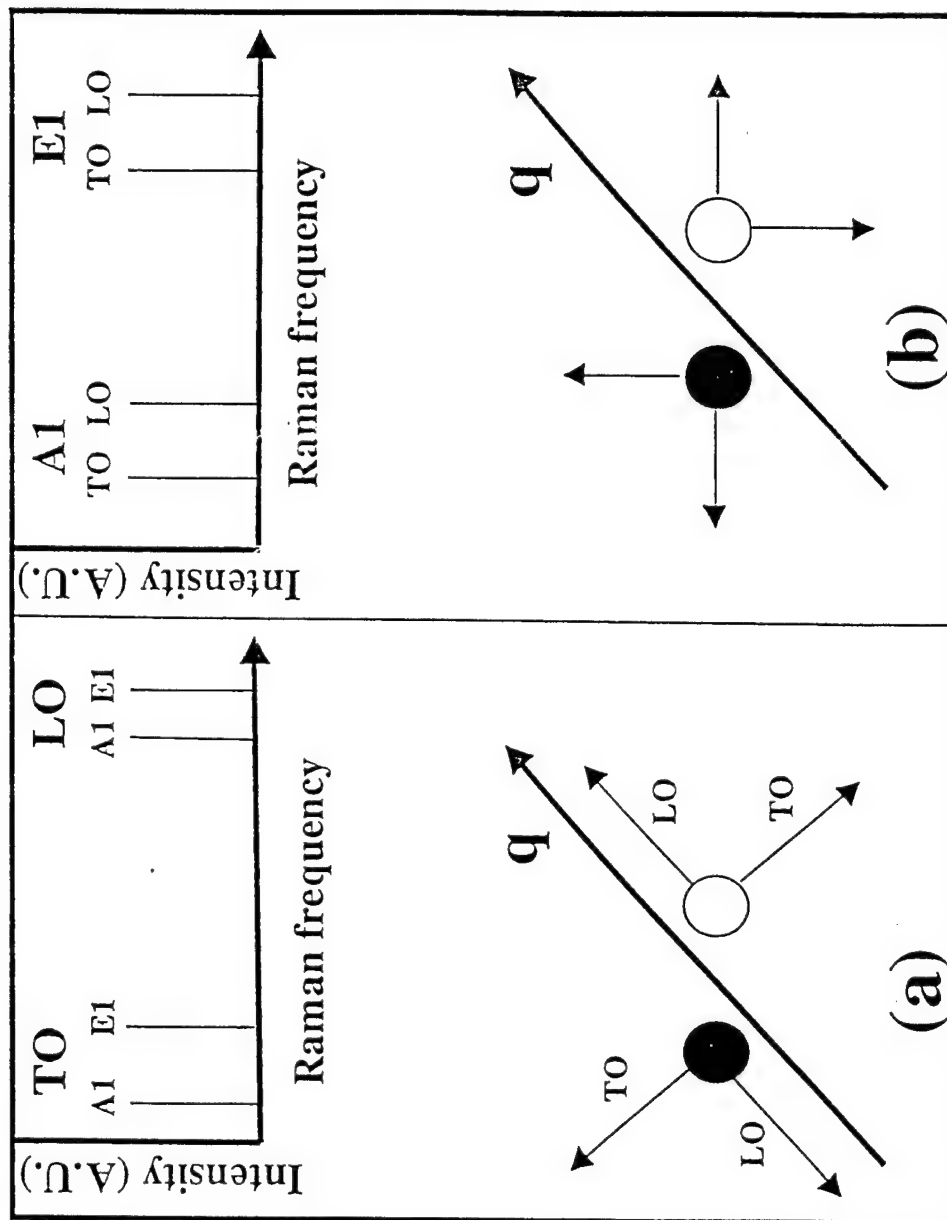


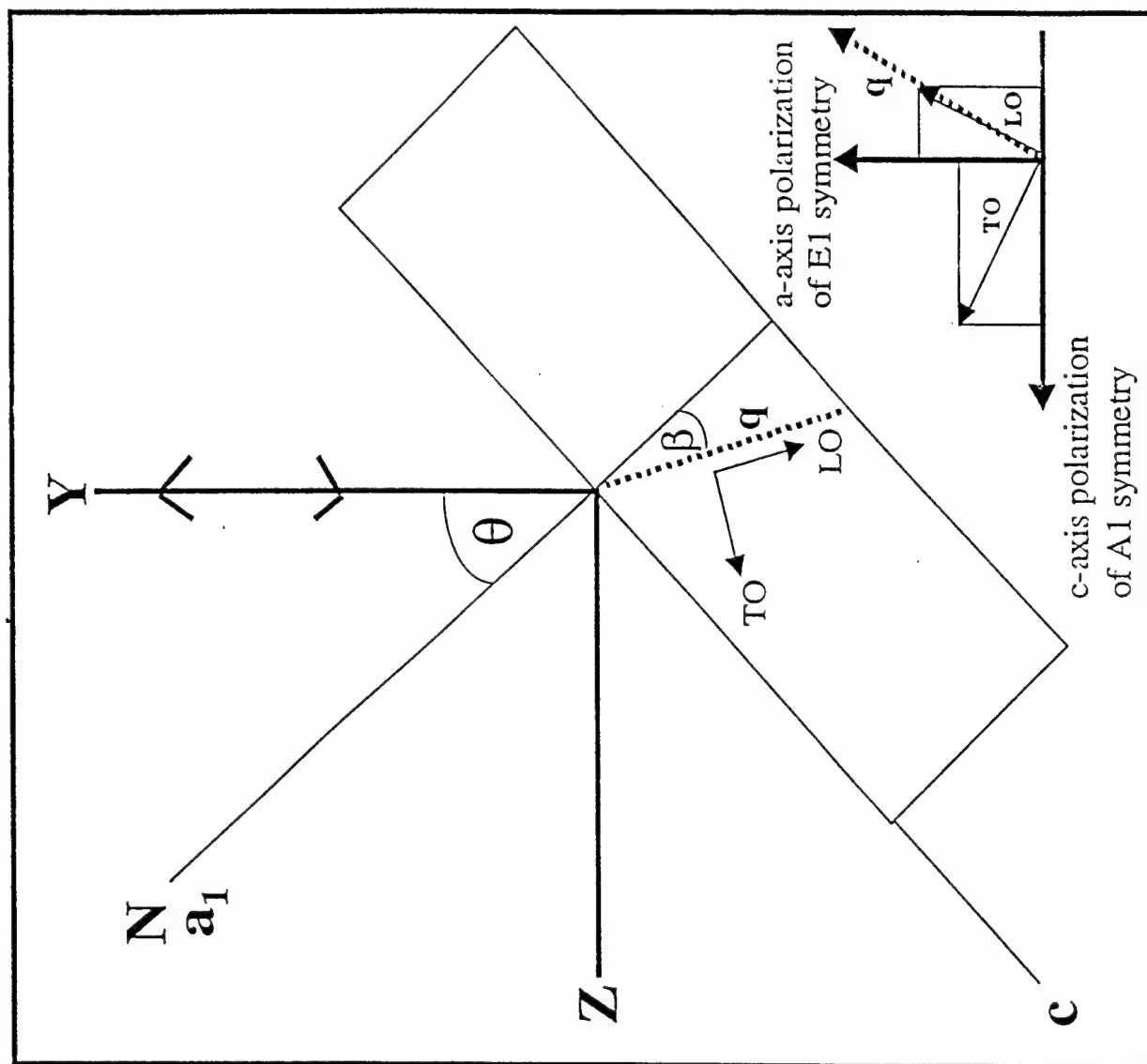


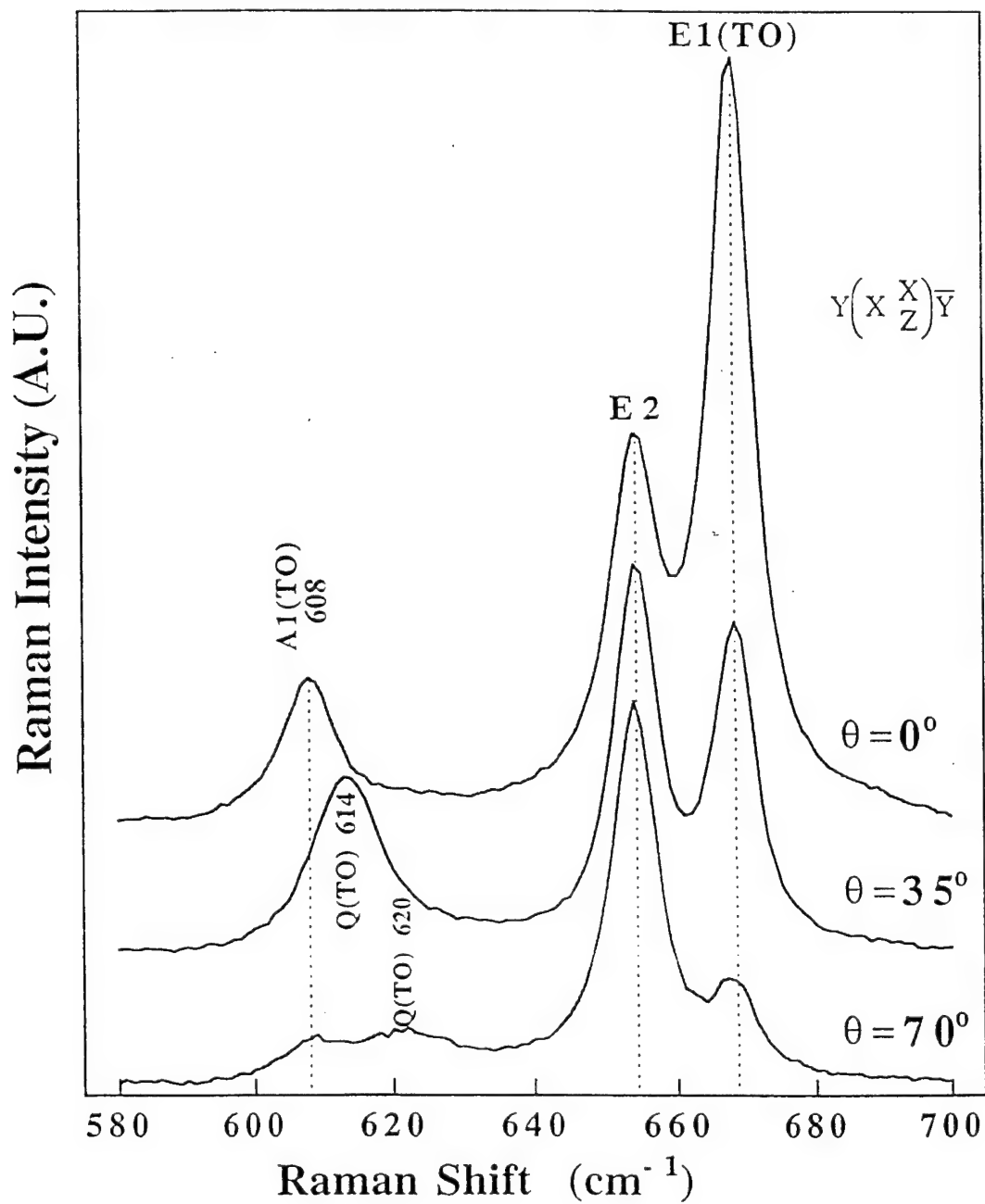


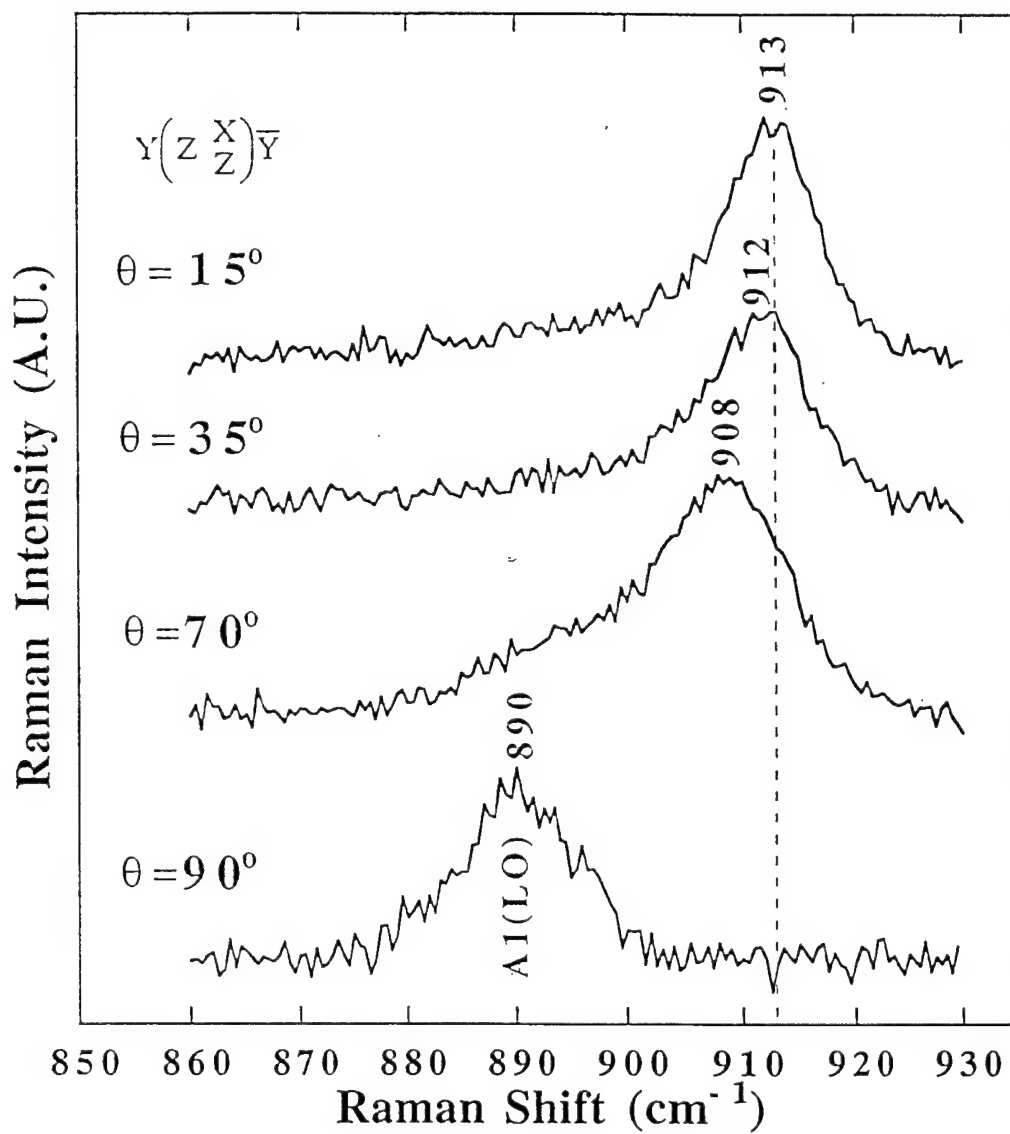


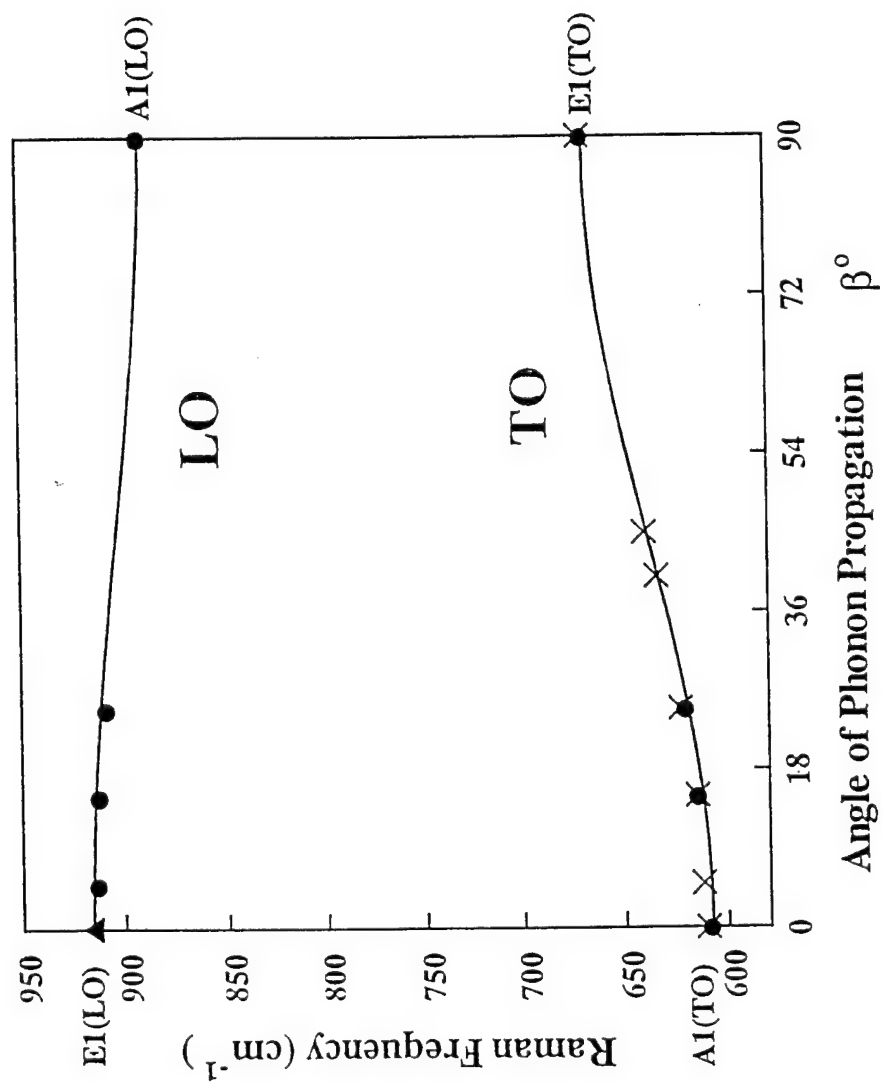


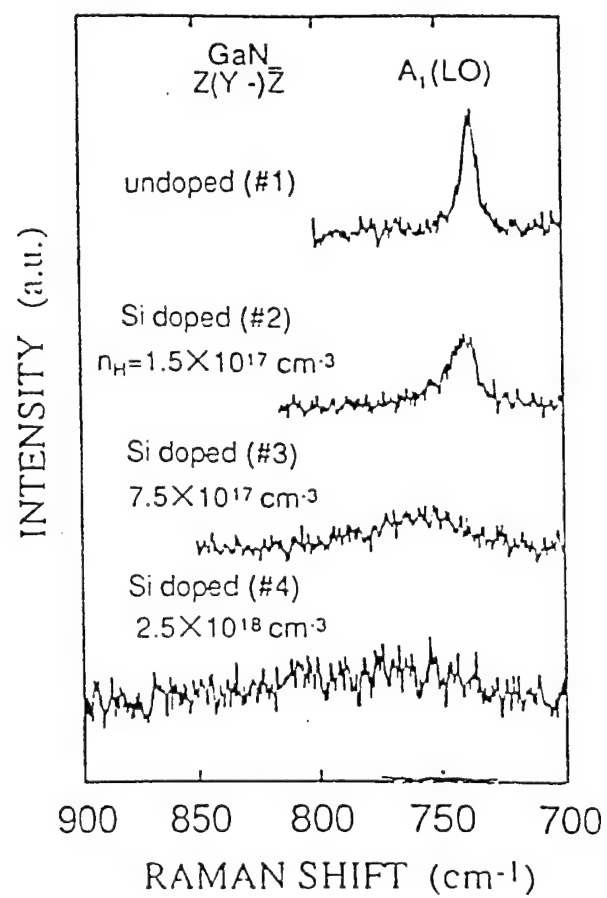


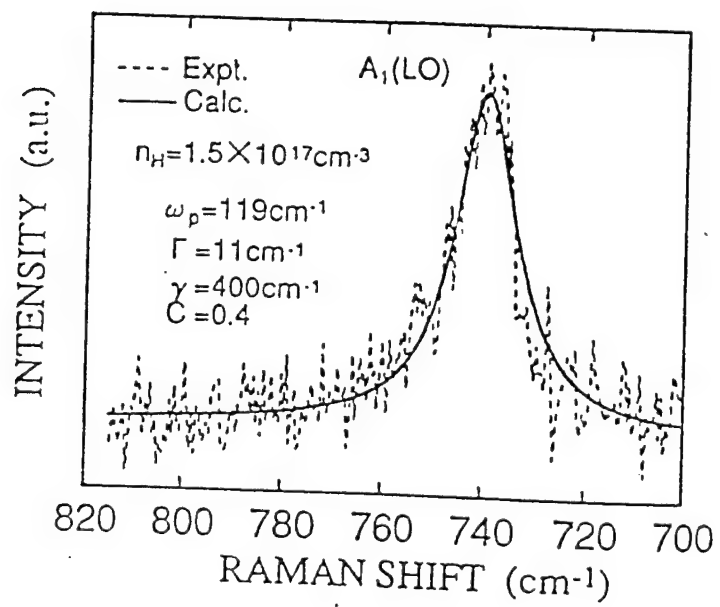


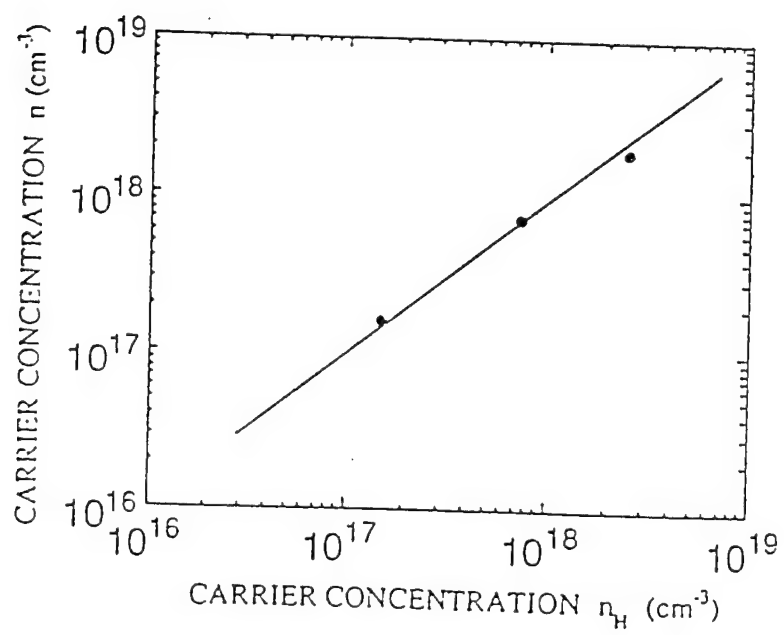


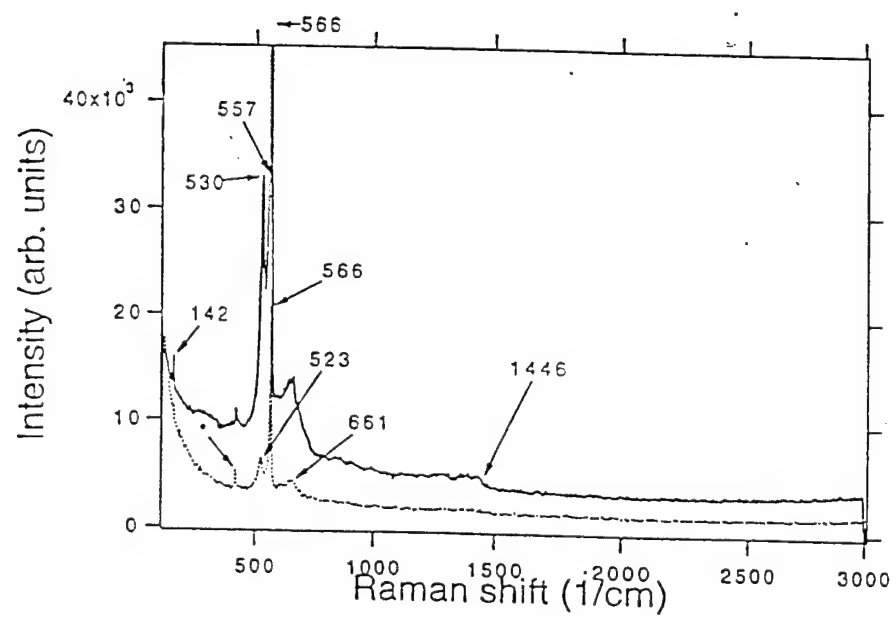


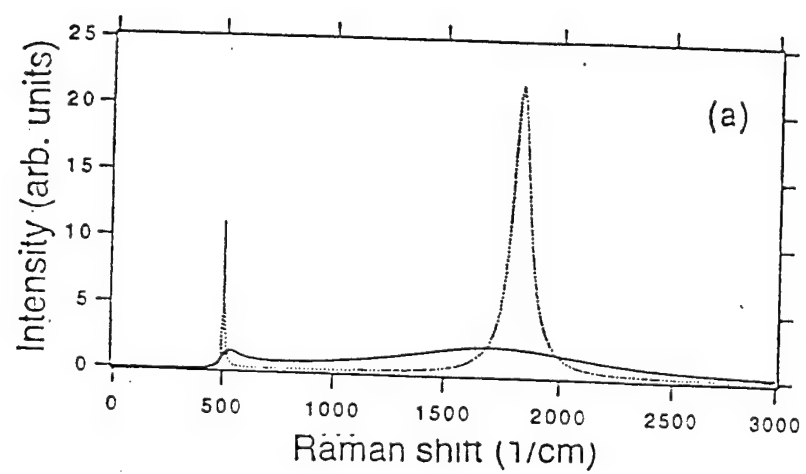


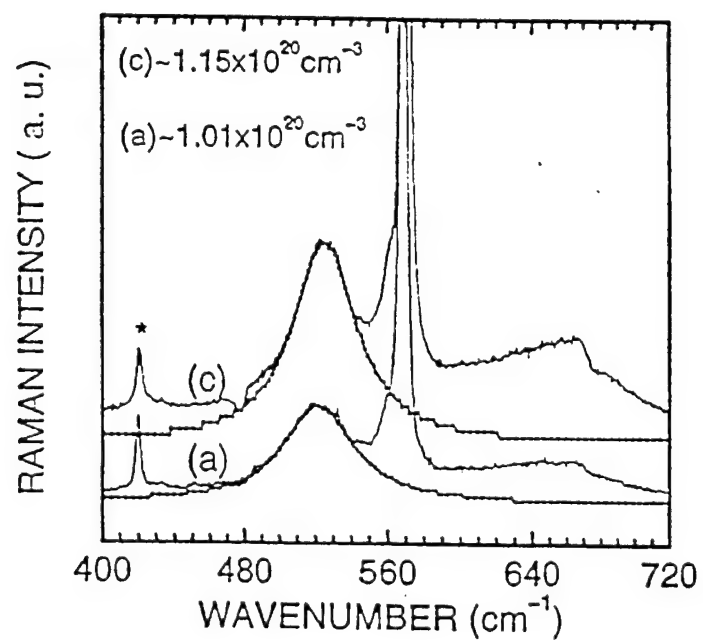


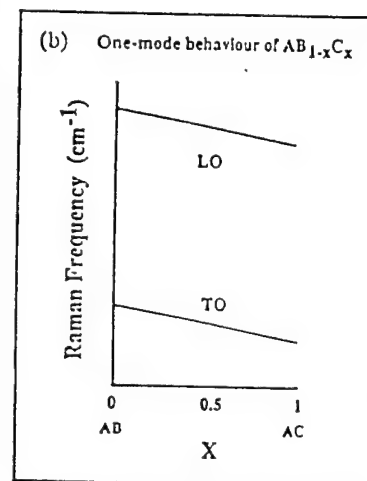
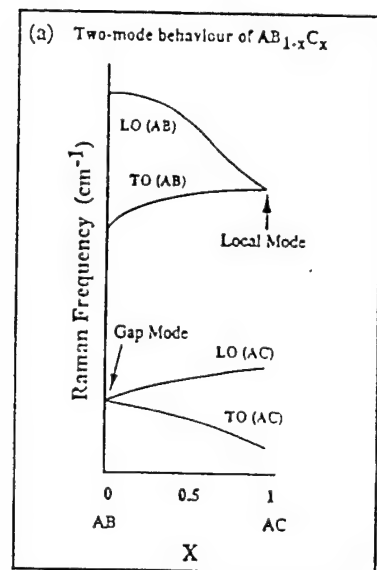


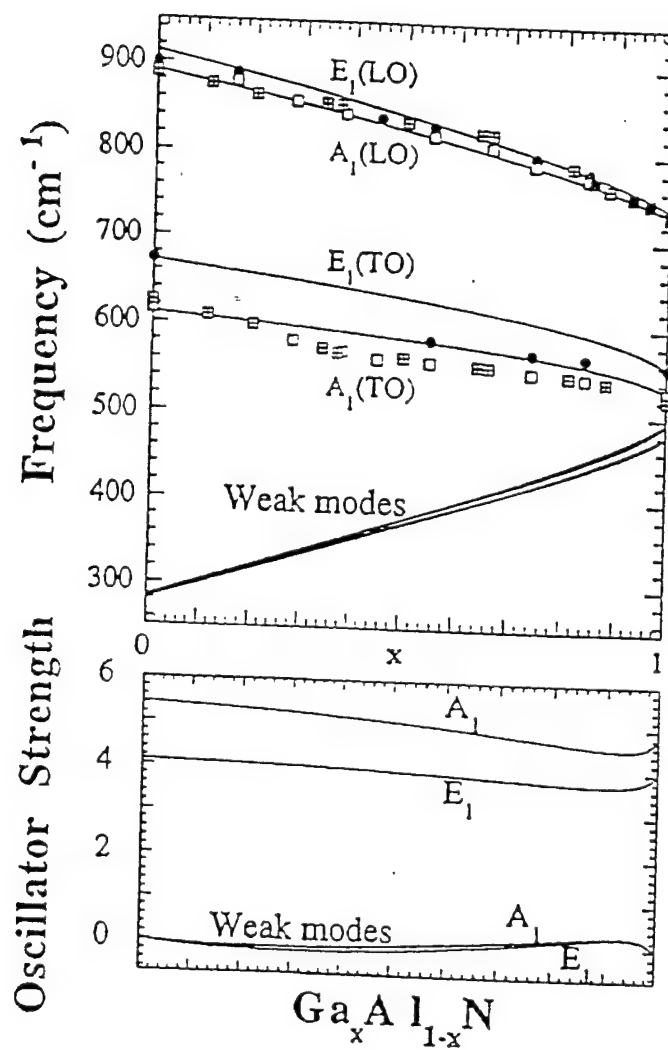


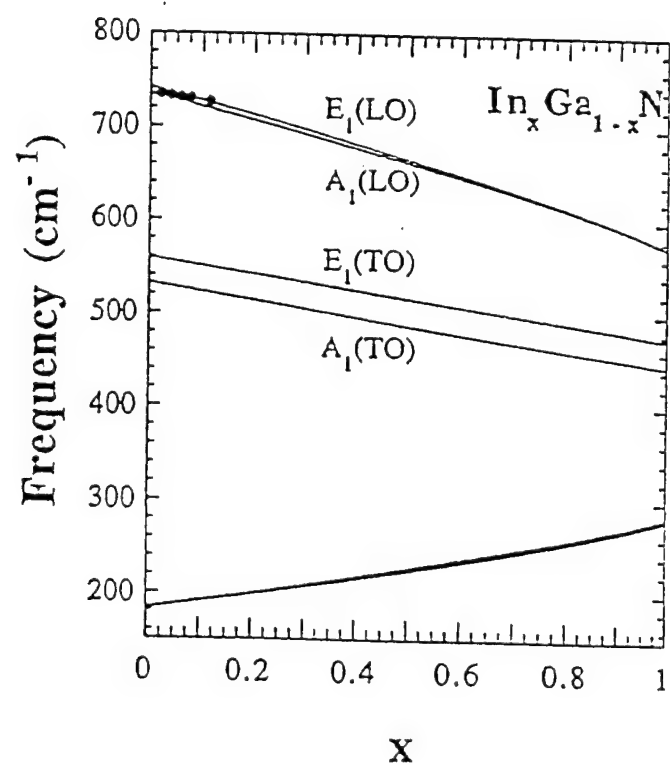


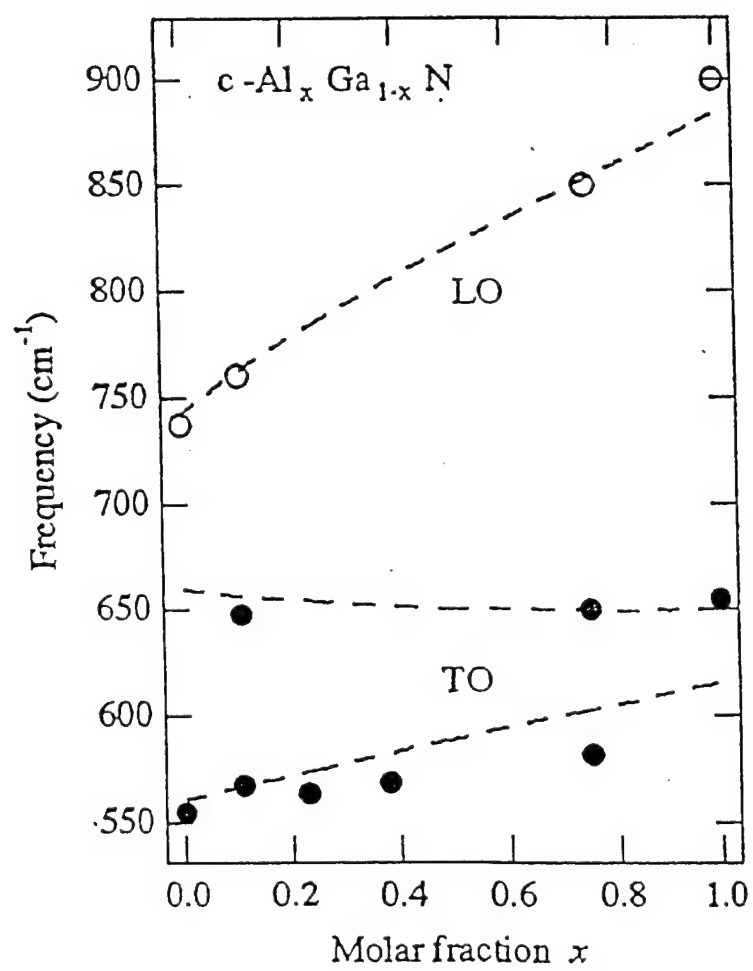


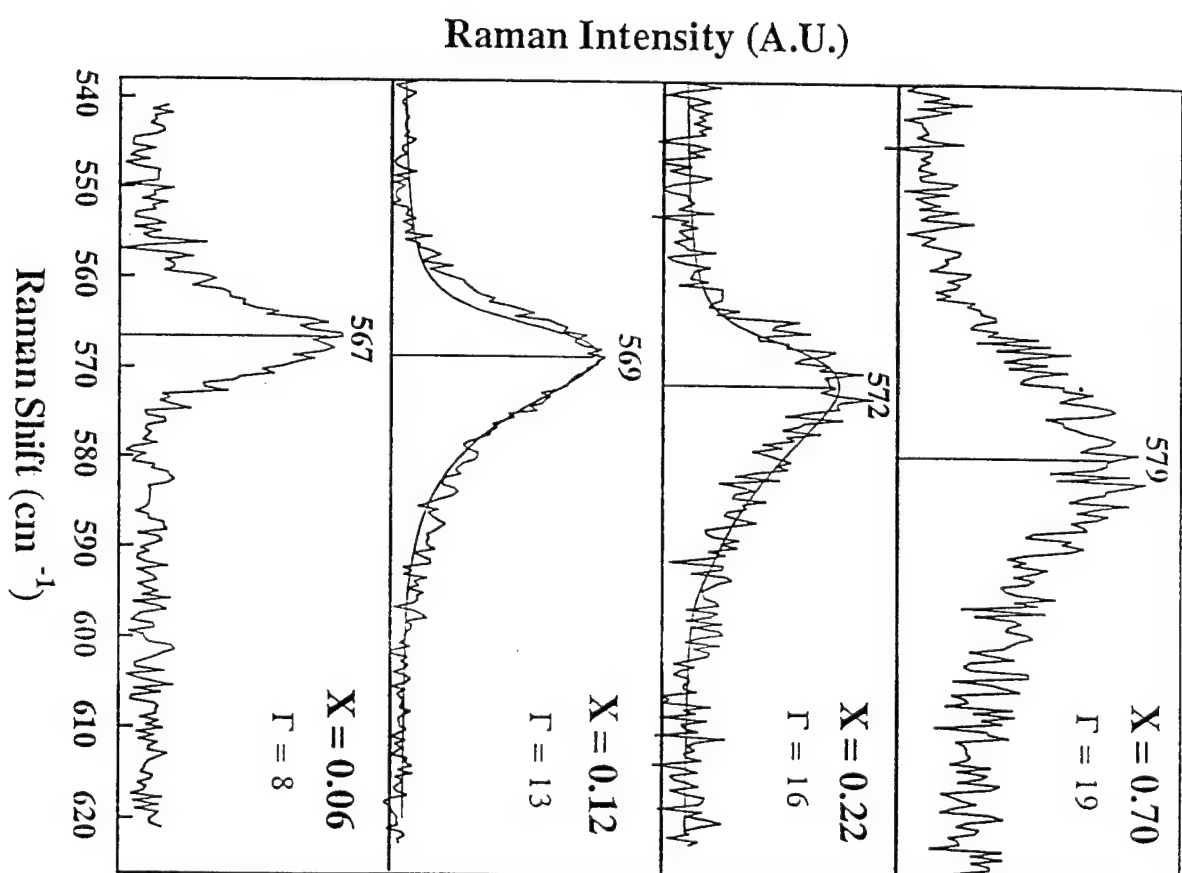


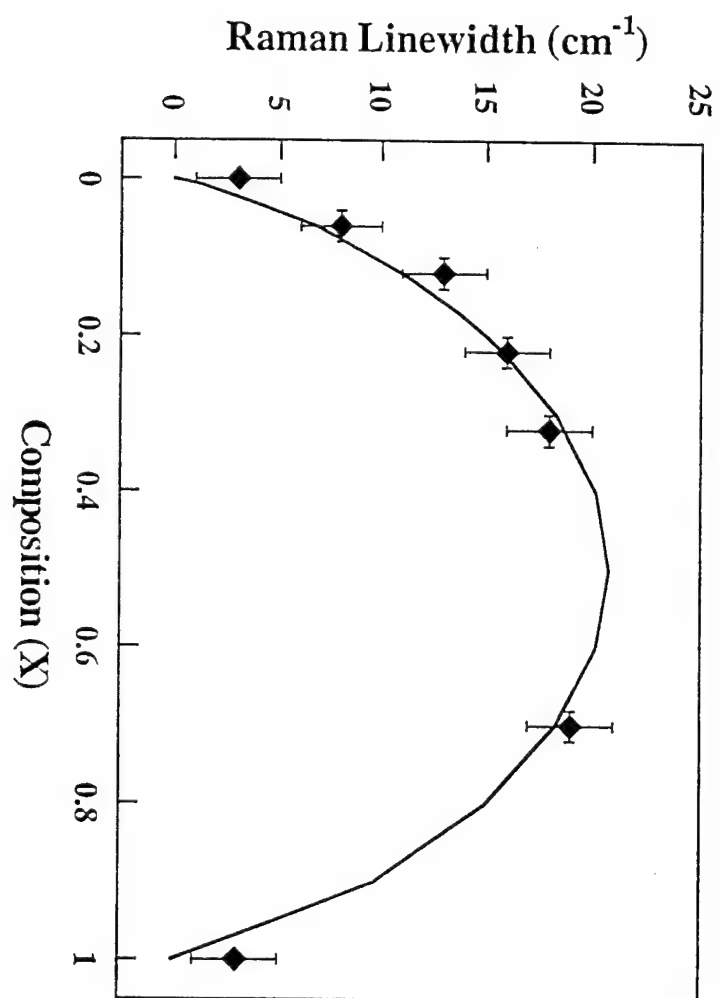












UV Raman Study of $A_1(\text{LO})$ and E_2 Phonons in $\text{In}_x\text{Ga}_{1-x}\text{N}$ Alloys

Dimitri Alexson, Leah Bergman, Robert J. Nemanich

Dept of Physics, North Carolina State University, Raleigh NC 27695-8202

Mitra Dutta, Michael A. Stroscio

U.S. Army Research Office, P.O. Box 12211, Research Triangle Park, North Carolina 27709-2211

C.A. Parker*, S.M. Bedair*, N.A. El-Masry**

*Electrical and Computer Engineering, North Carolina State University, Raleigh NC 27695

**Materials Science and Engineering, North Carolina State University, Raleigh NC 27695

Fran Adar

Jobin Yvon HORIBA Group, 3880 Park Avenue, Edison NJ 08820

We report on UV Raman spectroscopy of $\text{In}_x\text{Ga}_{1-x}\text{N}$ thin films grown on sapphire by metal-organic chemical vapor deposition (MOCVD). For the first time the $A_1(\text{LO})$ and E_2 phonon mode behavior was investigated over a large compositional range ($0 < x < 0.50$). Compelling evidence is presented for one-mode behavior for the $A_1(\text{LO})$ phonon, and data suggestive of two-mode behavior is presented for the E_2 phonon.

In recent years interest has increased in the group III nitrides as hopeful candidates for the fabrication of light emitting diodes and laser diodes operating throughout the visible region and into the UV range. AlN, GaN, and InN are an important set of semiconductors because their direct band gaps span the range 1.9 to 6.2eV [1]. In principle, this complete set of ternary alloys allows for any band gap within this range. This tunability of the energy band gap, combined with the fact that they generate efficient luminescence, has motivated the study and fabrication of high performance optical devices based on the group III nitrides. Potential applications range from high-density optical storage devices to projection and other bright displays. Presently much work and progress has been done on AlN, GaN, and their alloys. The growth of InGaN alloys, with a band gap energy range of 1.9 to 3.4eV, however, has proven to be very difficult. One of the main difficulties with InGaN growth is the large difference in interatomic spacing between GaN and InN of roughly 11%. This large difference can give rise to a solid miscibility gap and highly strained InGaN alloys [2]. As a result, phase separation in the alloy becomes a major concern. Until recently, there has been little attention given to the phonon mode behavior over a wide compositional range in the hexagonal wurzite $\text{In}_x\text{Ga}_{1-x}\text{N}$ system.

Mid and deep-UV Raman spectroscopy has been used here, we believe for the first time, as an effective tool for investigating LO-plasmon interactions and studying the issue of compositional inhomogeneities and spinodal decomposition in InGaN thin films. In addition, mode behavior over a large compositional range was investigated, and we have found compelling evidence for one-mode behavior for the $A_1(\text{LO})$ phonon mode,

while our data is suggestive of two-mode behavior for the E_2 mode consistent with the previously found behavior in AlGaN [3,4].

In this work, we study the Raman scattering spectra of $\text{In}_x\text{Ga}_{1-x}\text{N}$ alloys, grown on (0001) sapphire substrates using a specially designed metal-organic chemical vapor deposition (MOCVD) reactor and growth conditions that have been described elsewhere [5]. A buffer layer of GaN was grown on each substrate prior to the growth of the InGaN films. The growth temperature of the $\text{In}_x\text{Ga}_{1-x}\text{N}$ layer was between 690°C and 780°C. Variation of the growth temperature and the hydrogen gas flow rate determined the percent concentration of InN. Eight films were examined in the compositional range $0 < x < 0.50$. The composition x was determined by calculating the shift of the 0002 XRD InGaN peak relative to the 0002 peak position of GaN, and applying Vegard's law.

Raman scattering experiments, of thin $\text{In}_x\text{Ga}_{1-x}\text{N}$ films, using visible laser frequencies typically provide additional Raman peaks from buffer layers and substrates. In addition, InGaN films with low InN compositional content, emit strong interfering broadband luminescence in visible regions. The excitation of Raman scattering in the UV avoids both of these problems. The Raman spectral region of interest is well above any emitted photoluminescence, and there is strong absorption of the UV laser light in the film, resulting in a larger Raman signal and an absence of Raman peaks from layers below the film. The deep-UV Raman spectra were excited with the 244nm line of a frequency doubled Coherent Inc. Innova 300 FreD Argon Ion laser. The incident beam was focused onto the sample to a spot size of approximately 2mm in height and 50 microns in width. The intensity of the light on the surface of the sample, in this configuration, was on the order of 65 W/cm^2 . The scattered light was collected in a

backscattering geometry and imaged onto the entrance slit of a SPEX 1877 TripleMate spectrometer, equipped with a UV enhanced liquid nitrogen cooled CCD. Specialized high reflectance dielectric mirrors were used for steering the laser beam, and a single plano convex lens, of UV grade fused silica, was used to focus the scattered light. The Raman spectra were obtained with a 3600 gr/mm grating, providing 0.8 cm^{-1} resolution. The mid-UV Raman spectra were excited with the 325 nm line of a HeCd laser. The laser light was focused on the sample through a specialized 100x UV microscope objective down to a spot size of approximately 0.3 microns with a power density around $16.7 \times 10^5 \text{ W/cm}^2$. The scattered light was analyzed with a UV JY LabRam Infinity equipped with a UV enhanced liquid nitrogen cooled CCD. The Raman spectra were obtained with a 2400 gr/mm grating providing 3 cm^{-1} resolution. For both of these situations Raman scattering by the $A_1(\text{LO})$ and E_2 phonons are symmetry allowed from the (0001) surfaces of the hexagonal wurzite structures.

Figure 1 shows Raman spectra excited with the 244nm (5.1 eV) line of the frequency doubled Ar ion laser. The dashed lines indicate the Raman frequencies of the E_2 mode for InN and GaN. The value for the E_2 mode in InN was taken from other references [3-6]. Several Raman peaks due to scattering from air overlap the region of the $A_1(\text{LO})$ peak. Analysis of the $A_1(\text{LO})$ peak positions, for the data taken with the 244nm line, was not included for this reason. However, qualitative observations regarding the ratio of $A_1(\text{LO})$ to E_2 peak intensities are made. For the GaN and the films with low InN concentration, the intensity of the $A_1(\text{LO})$ mode, with respect to the E_2 mode, is small. The absence of the $A_1(\text{LO})$ mode has been previously observed in GaN and has been attributed to a high free carrier concentration in the film; the free carriers

form plasmon waves that interact and, in turn, damp the LO phonons [10,11]. The free carrier concentration of the GaN film used for Figure 1 was found to be $8.4 \times 10^{16} \text{ cm}^{-3}$ by Hall measurements. The free carrier concentrations in the InGaN films are of the order of 10^{18} cm^{-3} , and the concentration increases with higher In concentration. Despite this, the films with higher InN concentration show an increase in the $A_1(\text{LO})$ intensity with respect to the E_2 mode. Inushima et al. reported Raman spectra of InN films in which the $A_1(\text{LO})$ mode intensity was also greater than the E_2 mode intensity [9]. Their films were grown on (0001) sapphire substrates with a carrier density of $3 \times 10^{20} \text{ cm}^{-3}$ by Hall measurements. They ascribed this effect to the presence of a deep depletion layer on the air exposed surface of InN.

Figure 2 shows Raman spectra excited with the 325.2nm (3.81eV) line of the HeCd laser. The dashed lines again show the position of the E_2 mode for InN and GaN. Raman spectra for GaN could not be obtained due to the strong photoluminescence resulting from excitation just above the band gap of the material. In these spectra the opposite case is observed than in Figure 1. The E_2 mode intensity is weak with respect to the $A_1(\text{LO})$ mode for low concentrations of InN in the film. The $A_1(\text{LO})$ mode is easily detected, and though not shown here, even second and third order $A_1(\text{LO})$ phonons could be observed. This is presumably due to a resonant Raman effect at this laser energy. Also worth noting, the $A_1(\text{LO})$ mode develops an additional low energy feature for In concentrations higher than 15%. The shoulder and the large FWHM of the $A_1(\text{LO})$ peaks in Figure 2 have tentatively been assigned to compositional inhomogeneities and spinodal decomposition effects present in InGaN films that have been previously discussed [2,12,13]. This issue will be addressed more completely in a future publication.

Figure 3 shows the frequencies of the $A_1(\text{LO})$ and E_2 modes as a function of alloy composition. The filled circles represent the peak positions of the $A_1(\text{LO})$ mode in Figure 2. The peak positions of the $A_1(\text{LO})$ mode, in Figure 1, are not shown due to the presence of interfering air peaks, which made assignment of peak positions difficult. The crosses and unfilled circles in Figure 3 represent the E_2 mode frequencies from Figures 1 and 2 respectively. The peak positions, for the data in Figures 1 and 2, were determined by fitting the spectra with Lorentzian-Gaussian peak functions. The $A_1(\text{LO})$ peaks in Figure 2, which exhibited a low energy shoulder, were fit with two Lorentzian-Gaussian peak functions. The sample with 35.6% In concentration was fit with an additional high energy shoulder. The $A_1(\text{LO})$ peak positions used in Figure 3 are marked in Figure 2. These positions are assumed to be due to the majority phase of the alloy in the films, and the low energy shoulder is tentatively assigned to the phase segregated regions of higher In concentration. Similar InGa N films were analyzed by θ -2 θ x-ray diffraction. The x-ray data for films with concentrations above 40% In concentration showed a diffraction peak for the majority phase along with a shoulder that was fitted with several Gaussian distribution functions [13]. The authors ascribed this feature to phase separation occurring in the films. The value for the $A_1(\text{LO})$ mode in InN was taken from other references [6-9,14]. The $A_1(\text{LO})$ frequencies shift linearly as a function of percent InN composition. The experimental values presented here fit well with a linear extrapolation to the InN endpoint. This is indicative of one-mode behavior for the $A_1(\text{LO})$ mode. The one-mode behavior of the $A_1(\text{LO})$ phonon is in good agreement with theoretical calculations based on a modified random element isodisplacement model (MREI) for the

ternary family of semiconductors $AB_{1-x}C_x$ [15]. It has also been shown experimentally that the $A_1(\text{LO})$ phonon in $\text{Al}_x\text{Ga}_{1-x}\text{N}$ wurzite structures obeys a one-mode behavior [3,4].

The E_2 phonon frequencies shown in Figure 3, for the 244nm and 325.2nm laser lines, show a good consistent linear fit for the InN compositional range of $0 < x < 0.50$. However, the extrapolated line for the E_2 data intersects between 30 to 40 cm^{-1} lower at $x=1$ than the previously reported E_2 mode frequencies for InN. It has been shown experimentally that the E_2 phonon mode in the $\text{Al}_x\text{Ga}_{1-x}\text{N}$ wurzite structure displays a two-mode type behavior [3,4]. The phonon behavior in a mixed crystal of an $AB_{1-x}C_x$ ternary system falls into two main classes, referred to as one mode and two mode behavior. Phonons exhibiting one mode behavior have only one set of frequencies that show nearly linear dependency with the composition x , from the AB component to the AC component. The $A_1(\text{LO})$ mode in $\text{In}_x\text{Ga}_{1-x}\text{N}$ exhibits this behavior. On the other hand, the frequencies, of phonons in the two mode class of materials, exhibit a nonlinear dependence with composition x . Also, for an intermediate composition x in the two mode class of materials, two sets of frequencies are usually observed in the spectra. One set of frequencies is due to the modes of the lighter AB component and one set for the heavier AC component. These components in the $\text{In}_x\text{Ga}_{1-x}\text{N}$ crystal are GaN and InN. The absence of the InN set of frequencies in the spectra may be due to the large FWHM for peaks close to 50% In concentration, making it difficult to detect weak peaks in that spectral region.

In summary, we present the results of a Raman scattering study for a series of $\text{In}_x\text{Ga}_{1-x}\text{N}$ films from $x=0$ to 0.50, where the Raman scattering was excited with two different UV frequencies. Our results show the behavior of the $A_1(\text{LO})$ and E_2 modes as

a function of frequency. The $A_1(\text{LO})$ mode follows a one mode behavior while the E_2 mode appears to follow two mode behavior consistent with AlGaIn studies. The two different excitation frequencies provide complimentary information as to the aspects of the films, and provide more information to the behavior of the phonon-plasmon interaction as a function of Indium concentration that will be studied further.

Acknowledgements

The work at North Carolina State University was supported by the ARO (Army Research Office) under grants DAAH04-93-D-0003 and DAAD19-99-1-0293.

References

- [1] Orton JW, Foxon CT, Reports on Progress in Physics 61:(1) (1998)
- [2] I-hsiu Ho, G.B. Stringfellow, Appl Phys Lett **69**, 2701 (1996)
- [3] F. Demangeot, J. Groenen, J. Frandon, M.A. Renucci, O. Briot, S. Clur, R.L. Aulonbard, Appl. Phys. Lett. **72**, 2674 (1998)
- [4] A. Cros, H. Angerer, O. Ambacher, M. Stutzmann, R. Hopler, T. Metzger, Solid State Commun. **104**, 35 (1997)
- [5] E.L. Piner, N.A. El-Masry, S.X. Liu, and S.M. Bedair, in Nitride Semiconductors, edited by F.A. Ponce, S.P. DenBaars, B.K. Meyer, S. Nakamura, and S. Strite, Mater. Res. Soc. Proc. **482**, 125 (1998)
- [6] Hyuk-Joo Kwon, Yong-Hyun Lee, Osamu Miki, Hirofumi Yamano, Akira Yoshida, Appl. Phys. Lett. **69**, 937 (1996)
- [7] V. Yu Davydov, A. A. Klochikhin, M. B. Smirnov, V. V. Emstev, V. D. Petrikov, I. A. Abroyan, A. I. Titov, I. N. Goncharuk, A. N. Smirnov, V. V. Mamutin, S. V. Ivanov, T. Inushima, Phys. Stat. Sol. B **216**, 779 (1999)
- [8] Ming-Chih Lee, Heng-Ching Lin, Yung-Chung Pan, Chen-Ke Shu, Jehn Ou, Wen-Hsiung Chen, and Wei-Kuo Chen, Appl. Phys. Lett. **73**, 2606 (1998)
- [9] T. Inushima, T. Shiraishi, and V.Yu. Davydov, Solid State Commun. **110**, 491 (1999)
- [10] T. Kozawa, T. Kachi, H. Kano, Y. Taga, M Hashimoto, N. Koide, and K. Manabe, J. Appl. Phys **75**, 1098 (1994)

- [11] L. Bergman, M.D. Bremser, J.A. Christman, S.W. King, R.F. Davis, and R.J. Nemanich, in III-V Nitrides, edited by F.A. Ponce et al. MRS Symposia Proceedings No. 449 Symp. (Materials Research Society, Pittsburgh, 1997), p.725
- [12] D. Doppalapudi, S.N. Basu, K.F. Ludwig, Jr. and T.D. Moustakas, J. Appl. Phys. **83**, 1389 (1998)
- [13] N.A. El-Masry, E.L. Piner, S.X. Liu, S.M. Bedair, Appl. Phys. Lett. **72**, 40 (1998)
- [14] J.S. Dyck, K. Kash, K. Kim, W.R.L. Lambrecht, C.C. Hayman, A. Argoitia, M.T. Grossner, W.L. Zhou, and J.C. Angus, in Nitride Semiconductors, edited by T. Strite, MRS Symposia Proceedings No. 482 (Materials Research Society, Pittsburgh, 1998), p.549.
- [15] SeGi Yu, K.W. Kim, Leah Bergman, Mitra Dutta, Michael Stroscio, John M. Zavada, Phys. Rev. B **58**, 15283 (1998)

Figure Captions

Figure 1: Raman Spectra of InGaN films. Spectra excited with the 244nm line of the frequency doubled Ar ion laser. The dotted lines represent the positions of the E₂ mode for InN and GaN at 488 cm⁻¹ and 738 cm⁻¹.

Figure 2: Raman Spectra of InGaN films. Spectra excited with the 325.2nm line of a HeCd laser. The dotted lines represent the positions of the E₂ mode for InN and GaN at 488 cm⁻¹ and 738cm⁻¹. The positions of the A₁(LO) frequencies are marked.

Figure 3: Percent InN concentration vs frequency for the A₁(LO) and E₂ modes. A₁(LO) mode for 325.2nm data. E₂ mode for both 244nm and 325.2nm. The bars at x=1 represent data points for InN taken from the following refs. In descending order [6,8,7,9,14] for the A₁(LO) mode, and [6,8,7,9] for the E₂ mode.

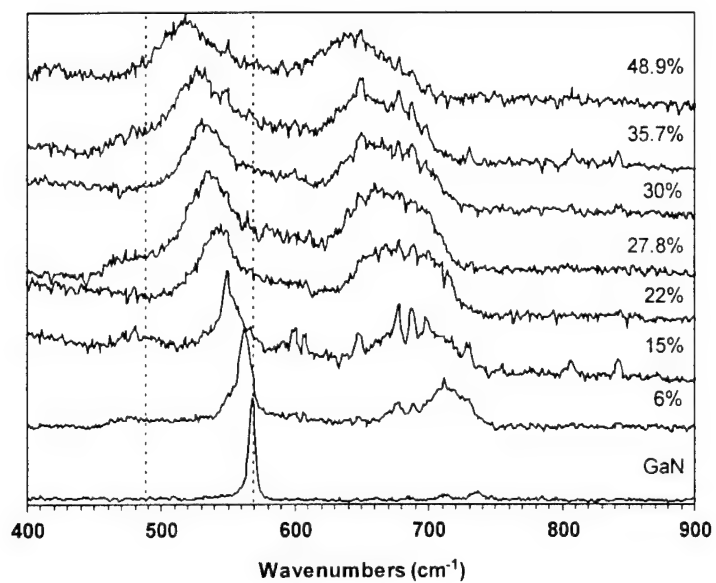


Figure 1

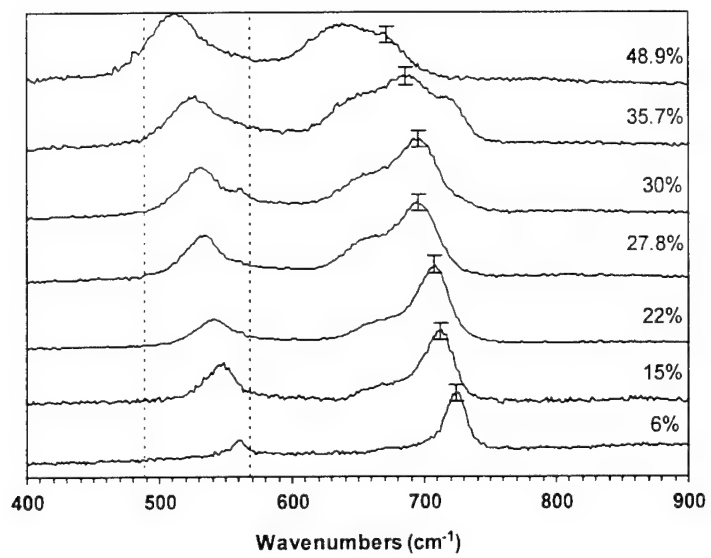


Figure 2

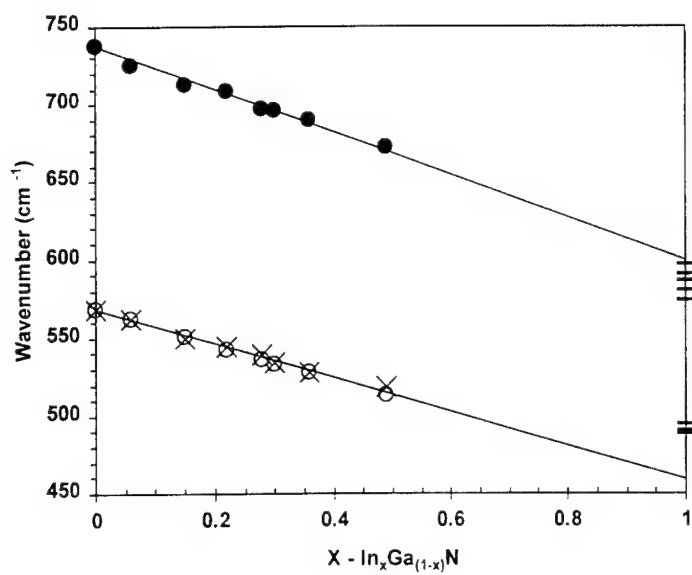


Figure 3

RAMAN ANALYSIS OF PHONON LIFETIMES IN AlN AND GaN OF WURTZITE STRUCTURE

Leah Bergman, Dimitri Alexson, Patrick L. Murphy, and Robert. J. Nemanich
Department of Physics, North Carolina State University, Raleigh, NC 27695-8202

Mitra Dutta, and Michael A. Stroscio

U. S. Army Research Office, P. O. Box 12211, Research Triangle Park, NC 27709-2211

Cengiz Balkas, Hyumin Shin, and Robert F. Davis

Department of Materials and Science Engineering, North Carolina State University, Raleigh, NC
27695

ABSTRACT

Raman analyses of the lifetimes of phonons in GaN and AlN crystallites of wurtzite structure are presented. In order to ensure the accuracy of the measurement of the phonon lifetimes, an experimental procedure to eliminate the broadening due to the finite slit width was performed. The lifetime analyses indicate that the phonon lifetimes in AlN as well as in GaN fall into two main time regimes: a relatively long time of the E_2^1 mode and much shorter times of the E_2^2 , $E1(TO)$, and $A1(TO)$ modes. The lifetimes of the E_2^1 , E_2^2 , $E1(TO)$, $A1(TO)$, and $A1(LO)$ modes of a high quality AlN crystallite are 4.4 ps, 0.83 ps, 0.91 ps, 0.76 ps, and 0.45 ps, respectively. Moreover, the lifetime of the $A1(LO)$ mode found in this study is consistent with the current phonon-decay model of that mode in wurtzite structure materials. The lifetimes of E_2^1 , E_2^2 , $E1(TO)$, and $A1(TO)$ of a GaN crystallite were found to be 10.1 ps, 1.4 ps, 0.95 ps, and 0.46 ps, respectively. The $A1(LO)$ mode in the GaN was not observed and its absence is attributed to the plasmon damping. The lifetime shortening due to impurities was also studied; the lifetimes of the Raman modes of an AlN crystallite which contains about two orders of magnitude more Si and C impurities relative to the concentration of the high quality crystallite were found to be 50 % shorter.

PACS Nos.: 63.20.-e, 63.20.Kr, 78.30.-j, 78.30.Fs

I. INTRODUCTION

The realization of device fabrication using AlN, GaN, and their alloy systems as the constituent materials, has led to numerous investigations concerning growth as well as analytical techniques to study and improve these wide-bandgap family semiconductors [1]. Raman spectroscopy has proven useful in analyzing the properties of wide-bandgap materials; it reveals information about sample quality as well as phonon interactions and dynamics [2-10].

One crucial aspect impacting device performance is phonon interaction with free carriers. In general the interactions can degrade the viability of the device; however, recent studies have demonstrated that the phonon interactions may be utilized to engineer certain laser devices [11-12]. The phonon lifetimes are important in both these effects, and one principal way of measuring these lifetimes is via Raman spectroscopy. It has been demonstrated previously that phonon lifetimes and the factors affecting them can be calculated from the Raman linewidth. Among the materials which have been analyzed via their Raman linewidth are diamond, Si, c-BN, GaAs, and InP [13-17].

In general, the theory of a spectral lineshape of a signal in a dispersive medium predicts the lineshape to be Lorentzian and the linewidth, a parameter describing the damping effect, to be inversely proportional to the lifetime of the signal [18]. For the case of a Raman signal of an ideal harmonic crystal, the lineshape is expected to be infinitesimally narrow; however, experiments have demonstrated that the Raman linewidths of most materials exhibit a finite width indicative of the presence of decay channels which shorten the phonons lifetimes [19-21]. One fundamental lifetime shortening mechanism in semiconductors with of diamond structure has been established to occur via the anharmonic interaction [20]. In this mechanism, the Raman phonons decay into other phonons that conserve momentum and energy. Moreover, in semiconductors containing impurities and defects it has been found that the these imperfections affect the Raman linewidth; thus, the contribution of the impurity shortening lifetime mechanism has to be taken into account [21-22].

In this paper, we present the study of the room-temperature lifetimes of the Raman phonons in AlN and GaN materials. The Raman modes investigated in the study are the E_2^1 , E_2^2 , $E1(TO)$, $A1(LO)$, and $A1(LO)$ modes. The $A1(LO)$ mode of the GaN crystallite was not observed in the Raman spectra and its absence is attributed to the high free carrier concentration

of that crystallite; the free carriers form plasmon-waves which interact and in turn damp the LO phonons [2, 7]. However, due to the insulating properties of the AlN, the A1(LO) mode was observed in the spectra of the crystallites. For AlN and GaN crystallites we found that the phonons can be separated into two time regimes: a long lifetime range of the E_2^1 phonon, and a much shorter lifetime range which characterizes phonons including the E_2^2 , E1(TO), and the A1(TO) modes. Moreover, the A1(LO) phonon of the AlN was found to have the shortest value among the AlN modes. In addition, we investigated two AlN crystallites which differ in their impurity-concentration and found that the phonon lifetimes were correlated with the impurity concentrations. Also, we studied the E_2^2 phonon lifetime of high quality GaN film at room temperature and at 10 K. Our results indicate that the phonon lifetime of the film is similar to that of the crystallite; moreover, no significant difference between the lifetimes in the two temperature ranges has been observed.

The A1(LO) mode lifetime has been considered theoretically for wurtzite-based structures [23]; this model predicts a three-phonon anharmonic process in which the A1(LO) decays into an E1(TO) phonon and an LA phonon. Our experimental measurements of this lifetime are consistent with the predictions of the model.

II. EXPERIMENT

Single crystals of GaN and AlN were grown via the sublimation method described in detail in [24-26]. A short summary is outlined herein highlights the findings presented in these references which are relevant to our present studies. The GaN hexagonal crystallites are colorless and secondary ion mass spectroscopy (SIMS) indicated that the concentration of all impurities, with the exception of oxygen, were at background levels; the oxygen concentration was 3×10^{18} atoms/cm³. Moreover, photoluminescence and transmission spectroscopies indicated that the GaN crystallites were of high optical quality and no deep level impurities were present.

Two different qualities of hexagonal AlN crystallites were also grown via the sublimation method [24]: one type of crystallites was grown in the 2100-2250 °C temperature range, of blue color, and will be referred to as such in this paper. The other type of crystallites, that will be referred as the transparent crystallites, were grown in the 1950-2050 °C range. SIMS analysis confirmed that the transparent crystallites contain about two orders of magnitude less Si and C

impurities than the blue AlN. Oxygen impurity concentrations are similar in both samples. The Si and C impurities were incorporated into the crystals from the SiC seed substrates while the oxygen was incorporated from the growth-environment. The transmission electron microscopy (TEM) images of the AlN crystallites indicated that they are of high quality; no high angle boundaries, stacking faults, or twinned region were observed. In addition, X-ray diffraction indicated that the residual stress level in the crystallites is low. Fig. 1 depicts one of the transparent AlN crystallites.

The micro-Raman scattering experiments were carried out at room temperature utilizing the 514.5 nm line of the argon ion continuous laser, and the J-Y U1000 scanning double monochromator. The spot size of the laser on the samples was $\sim 2 \mu\text{m}$ in diameter. The experimental error of the Raman data is $\pm 0.2 \text{ cm}^{-1}$. The data were acquired in backscattering geometry from the a-face of the AlN and GaN crystallites for the observation the E_2^1 , E_2^2 , $E_1(\text{TO})$, and $A_1(\text{TO})$ modes, and from the c-face for the observation of the $A_1(\text{LO})$ mode. The cold temperature measurements were carried out at the macro-mode with a spot size $\sim 1 \text{ mm}$ in diameter. The error in the lifetime values, which is partially due to the experimental error and partially due to the lineshape data fit, was estimated to be $\pm 10\%$.

III. RESULTS AND DISCUSSION

In order to obtain the phonon lifetime via the Raman spectral linewidth, the linewidth has to be corrected for the contribution of the instrumental bandpass broadening. The following section describes the method used in this study to determine the actual phonon linewidth. The Raman spectra acquired at successive slit widths ranging from $400 \mu\text{m}$ down to $100 \mu\text{m}$; the measured linewidths, W_M , were plotted as functions of the slit width, W_S , and extrapolated to the zero-slit value, W_P , via the relation [27-28]:

$$W_M = \sqrt{W_P^2 + (W_S * 9.2 * 10^{-3})^2} \quad (1)$$

The second term in Equation 1 is the instrumental bandpass, i.e., the slit width multiplied by the monochromator linear dispersion, $9.2 * 10^{-3} \text{ cm}^{-1}/\mu\text{m}$. This method yields the actual phonon linewidth, W_P , from which the phonon lifetime may be calculated. However, Equation 1 is an approximation that can be used only when the lineshape of the instrument bandpass can be

approximated by a Gaussian and that of the phonon by a Lorentzian [27-28]. To check the bandpass characteristics of our Raman system, a spectrum of a high quality diamond crystal (first checked to be mostly Lorentzian at 100 μm slits and $W_P \sim 1.8 \text{ cm}^{-1}$) was acquired at a relatively open slit width of 600 μm in which case the dominance of the instrumental broadening component is expected. The lineshape was found to be mostly Gaussian of linewidth 5.5 cm^{-1} which can be attributed to instrumental broadening. Moreover, the lineshapes of the nitride crystals studied here exhibit mainly a Lorentzian component at the lower slit-values as depicted in Fig. 2. These experimental results validate the appropriateness of using Equation 1.

In general, the zero-slit Raman linewidth arises from a convolution of all broadening mechanisms which in turn are due to the lifetime shortening mechanisms occurring in a given crystal [21]. The two main mechanisms controlling the phonon lifetimes are the phonon anharmonic interactions in which a phonon decays into other phonons, and the phonon scattering at impurity or defect centers which is sometimes treated as a source of the inhomogeneous broadening. In the subsequent discussion, we present a study of lifetime shortening mechanisms in two types of AlN crystallites which differ mainly in their impurity contents. Figures 3 and 4 depict the Raman spectra along with the deconvoluted spectra of the AlN crystallites. The spectra presented in Fig. 3 were acquired from a transparent AlN crystallite while those in Fig. 4 are from a blue AlN crystallite. As was indicated in the previous discussion on experimental measurements, the blue crystallite contains about two orders of magnitude more Si and C impurities than the transparent AlN. In both spectra the $A_1(\text{TO})$, E_2^2 , and $E_1(\text{TO})$ Raman modes are at 608 cm^{-1} , 655 cm^{-1} , and 668 cm^{-1} , respectively. No peak shift difference between the two spectra which exceeds the experimental error of $\pm 0.2 \text{ cm}^{-1}$ is evident. Thus, both samples are similar in their high quality of crystallinity and low levels of residual stress state. Moreover, the impurities have no significant effect on the residual stress. Figure 5 depicts the E_2^1 Raman mode at 246 cm^{-1} for both crystallites, and Fig. 6 presents the spectra of the $A_1(\text{LO})$ mode at 890 cm^{-1} .

In order to calculate the phonons lifetime via the Raman linewidths, the linewidths were plotted as a function of the slit width and a curve fit was obtained via Equation 1. The results are presented in Fig. 7; the dots represent the data taken from the transparent AlN and the squares data from the blue crystallite. It is evident from the figure that the linewidths of all the Raman modes are strongly correlated with the impurity concentration. The values of the Raman

linewidths at zero slit width may be used to evaluate the phonons lifetime, τ , via the energy-time uncertainty relation [18],

$$\frac{\Delta E}{\hbar} = \frac{1}{\tau} \quad (2)$$

where ΔE is the Raman linewidth in units of cm^{-1} , and $\hbar = 5.3 \times 10^{-12} \text{ cm}^{-1}\cdot\text{sec}$. Table I summarizes the results: for each sample the zero slit linewidth is presented along with the calculated lifetime for each of the Raman modes. Two main conclusions can be drawn from the above results: the lifetimes are correlated with impurity concentration, and the E_2^1 mode of both samples has a significantly longer lifetime than those of the E_2^2 , $E1(\text{TO})$, $A1(\text{TO})$, and $A1(\text{LO})$ modes.

The first finding may be indicative of the existence of a phonon lifetime shortening mechanism via impurities and will be discussed next. One fundamental mechanism which affects phonon lifetimes in semiconductors is the anharmonic decay of a phonon into other Brillouin zone phonons such that the energy and momentum is conserved in the process [20]. However, other channels of phonon-decay are clearly possible especially in material containing impurities and defects [5, 21]. These crystal imperfections can destroy the translational symmetry of the crystal, and thus perturb the characteristic lifetimes of the propagating phonons. Our findings indicate that both channels for the phonon decay exist in the AlN crystallites; therefore, the measured lifetime, τ , in Equation 1 may be given by [18]:

$$\frac{1}{\tau} = \frac{1}{\tau_A} + \frac{1}{\tau_I} \quad (3)$$

where τ_A and τ_I are the characteristic decay times due to the crystal anharmonicity and impurity scattering, respectively. It is not a straightforward task to deconvolute the shortening mechanisms of the phonon lifetimes but the following approximate treatment gives an estimate for τ_I . Specifically, due to its high crystal-quality and relatively low impurity content, the measured phonon lifetimes of the transparent crystallite can be assumed to be controlled mainly by the anharmonic interaction and thus to be equal to the value of τ_A of each of the phonons. Using the values of τ_A as the characteristic anharmonic decay times of AlN, the decay times due to impurities in the blue crystallite can be calculated via Equation 3. This approximate method

yields values of τ_l of 3.7 ps, 0.89 ps, 1.27 ps, 0.72 ps, and 0.74 ps for the E_2^1 , E_2^2 , E1(TO), A1(TO), and A1(LO) modes, respectively.

The anharmonic decay of phonons has been studied extensively for zinc-blende semiconductors [20, 29-30] but has received considerably less attention for wurtzite structure materials such as $\text{Al}_x\text{Ga}_{1-x}\text{N}$ [23, 31]. Of special significance for the nitride-based wurtzite structures is the decay of the LO phonon modes which dominates in the polar-optical-phonon carrier interaction in many high speed optoelectronic devices [32-33]. The accepted model, known as Klemens' model, of LO phonon decay in cubic structure materials has been established to occur via the annihilation of the LO Raman phonon (of frequency ω_{LO}) and the creation of two LA phonons (each of frequency ω_{LA}) at the zone edge [20]. In this model, a special case of the three phonon process, energy conservation requires that $2\omega_{\text{LA}} = \omega_{\text{LO}}$. However, in AlN, due to the substantial mass difference between the Al and the N elements a large gap in the AlN phonon spectrum exists: the A1(LO) frequency at the Γ point is at $\sim 890 \text{ cm}^{-1}$ while the LA at zone edge has frequency $\sim 400 \text{ cm}^{-1}$ [34]. Accordingly the Klemens' channel is not applicable here since $2\omega_{\text{LA}} < \omega_{\text{LO}}$. A four-phonon interaction would permit the conservation of energy; however, this interaction would result in an unreasonably long lifetime on the order of two or three orders of magnitude longer than that predicted for the three phonon process [23]. To account for the lifetime of the LO in the wurtzite materials, a three-phonon model has been proposed recently in which the LO mode decays into a TO mode and an LA mode; a decay route which results in a more reasonable lifetime of a few picoseconds [23]. This model has been supported by time-resolved Raman measurements of the A1(LO) phonon lifetime in wurtzite GaN thin films [31]. Moreover, our experimental results for the A1(LO) lifetimes of the AlN crystallites (~ 0.5 ps) are in accord with the time scale of the three-phonon anharmonic process, if we include impurity scattering as an additional shortening mechanism.

In order to further investigate the relatively long lifetime of the E_2^1 mode, the Raman modes of GaN as well as ZnO crystals were analyzed. Figures 8 and 9 depict the Raman spectra of the GaN crystallite: the A1(TO), E1(TO), E_2^2 , and E_2^1 modes are at 530 cm^{-1} , 558 cm^{-1} , 567 cm^{-1} , and 142 cm^{-1} , respectively. The corresponding lifetimes computed via the previously-described method are summarized in Table I. Similar to the AlN lifetimes, the E_2^1 mode of the

GaN has a significantly longer lifetime than those of the E_2^2 , $E_1(\text{TO})$, and $A_1(\text{TO})$ modes. Figure 10 depicts the linewidth behavior of the E_2^1 and the E_2^2 modes of the ZnO, GaN, and the transparent AlN crystals; the zero slit lifetimes of the ZnO modes are presented in Table I. Our analyses indicate that the E_2^1 mode of the ZnO crystallite exhibits a relatively long lifetime as well. As was noted previously, the LO mode-lifetime in wurtzite structure has been considered [23]. However, the long lifetime of the E_2^1 mode in that structure is not unexpected in view of energy-conservation constraints, the densities of the final states, and the fact that the anharmonic coefficient has not been determined theoretically. The energy of the E_2^1 mode lies in the low energy regime of the wurtzite dispersion curves [34-35] and only the acoustical phonons are available as the final states of the decay process. Indeed at energies where the densities-of-states are appreciable for the final state phonons, the energies of these phonons are comparable with those of the E_2^1 mode; thus, it may be reasonable to expect that the matrix elements for energy-conserving decay processes multiplied by the corresponding densities-of-states be reduced, relative to the other modes. Such a reduced scattering rate would, of course, result in a longer lifetime of the mode. A full understanding of our measured value for the lifetime of the E_2^1 mode must await detailed theoretical calculations.

Lastly, we investigated the E_2^2 mode of GaN film. Fig. 11 depicts the Raman spectra of a 3 μm undoped GaN film grown on a SiC substrate with an AlN buffer layer and with a free carrier concentration $\sim 10^{16} \text{ cm}^{-3}$ [7]. The spectra were acquired in a backscattering geometry at room temperature (RT) and at 10 K; the slit width was set at 200 μm . The lineshape of both lines is a Lorentzian with a linewidth of 4 cm^{-1} and 3.2 cm^{-1} for the RT and the 10 K spectrum, respectively. Using Equations 1 and 2, the zero slit values and the lifetimes may be calculated. The RT and the 10 K lifetimes were found to be 2 ps and 1.5 ps, respectively. Our results indicate that the lifetime of the E_2^2 mode of the GaN film is similar to that of the crystallite (1.4 ps). Furthermore, no significant lifetime change occurs at 10 K. A weak and broad $A_1(\text{LO})$ Raman line from the film was observed in the spectra; however, due to the strong SiC Raman signal which appears in the same energy range, an accurate analysis of the $A_1(\text{LO})$ lifetime was not possible. The lifetime of the $A_1(\text{LO})$ mode was obtained previously [31] via time-resolved

Raman measurements; this reported lifetime was ~ 3 ps. This lifetime is of the same order-of-magnitude as the lifetimes reported here for the other phonons in the GaN crystallite; see Table I.

IV. CONCLUSIONS

The lifetimes of the Raman phonons of GaN and AlN were found to exhibit two time regimes: the long lifetime range for the E_2^1 phonons and the much shorter lifetime range for the E_2^2 , $E1(TO)$, and $A1(TO)$ phonons. The lifetime of the $A1(LO)$ mode of AlN crystallites were found to be the shortest among the modes studied here. The E_2^1 lifetime of high-quality and of relatively low-impurity-concentration AlN crystallite is 4.4 ps, which is about five times longer than that of the E_2^2 , $E1(TO)$, and $A1(TO)$ modes and about an order of magnitude longer than those of the $A1(LO)$ mode. The lifetime of the E_2^1 mode of the GaN crystallite is 10.1 ps, which is about ten times longer than those of the other modes. We also investigated two AlN crystallites differing in their impurity concentration and found that the phonon lifetimes were correlated with the impurity concentrations. The effect of the two order-of-magnitude increase in relative impurity concentration shortened the lifetime of the phonons by $\sim 50\%$. Additionally, we studied the E_2^2 phonon lifetime of a high-quality GaN film at room temperature and at 10 K. Our results indicate that the phonon lifetime of the film is similar to that of the crystallite; moreover, no significant difference between the lifetimes at the two temperature ranges was observed.

ACKNOWLEDGMENTS

We gratefully acknowledge the Army Research Office for supporting this study. Leah Bergman acknowledge, additionally, the National Research Council for supporting this research via the Research Associateship Award program. We have also benefitted from the ongoing collaboration with Professor Ki Wook Kim and his group in the Department of Electrical and Computer Engineering at the North Carolina State University.

Table I: The zero slit-width Raman linewidths and the corresponding phonon lifetimes of the AlN, GaN, and ZnO crystallites.

	AlN Transparent		AlN Blue		GaN		ZnO	
Raman Modes	Γ (cm^{-1})	τ 10^{-12} sec	Γ (cm^{-1})	τ 10^{-12} sec	Γ (cm^{-1})	τ 10^{-12} sec	Γ (cm^{-1})	τ 10^{-12} sec
E_2^1	1.2	4.4	2.6	2.0	0.5	10.1	0.9	5.9
E_2^2	6.4	0.83	12.4	0.43	3.9	1.4	5.9	0.9
E1(TO)	5.8	0.91	10.0	0.53	5.6	0.95		
A1(TO)	7.0	0.76	14.4	0.37	11.6	0.46		
A1(LO)	11.9	0.45	18.9	0.28				

REFERENCES

1. *Properties of Group III Nitrides*, Edited by J.H. Edgar (INSPEC, London 1994).
2. T. Kozawa, T. Kachi, H. Kano, Y. Taga, M. Hashimoto, N. Koide, and K. Manabe. *J. Appl. Phys.* **75**, 1098 (1994).
3. L. Bergman, and R.J. Nemanich, *Annu. Rev. Mater. Sci.* **26**, 551 (1996).
4. C. A. Arguello, D.L. Rousseau, and S.P.S. Porto, *Phys. Rev.* **181**, 1351 (1969).
5. J.M. Zhang, T. Ruf, M. Cardona, O. Ambacher, M. Stutzmann, J.M. Wagner, and F. Bechstedt, *Phys. Rev.* **B56**, 14399 (1997).
6. L. Bergman, M.D. Bremser, W. G. Perry, R. F. Davis, M. Dutta, and R. J. Nemanich. *Appl. Phys. Lett.* **71**, 2157 (1997).
7. L. Bergman, M.D. Bremser, J.A. Christman, S.W. King, R.F. Davis, and R.J. Nemanich. *Mat. Res. Soc. Proc.* Vol.449, P. 725 1996.
8. F. Demangeot, J. Groenen, J. Frandon, M.A. Renucci, O. Briot, S. Clur, and R.L. Aulombard, *Appl. Phys. Lett.* **72**, 2674 (1998).
9. S. Murugkar, R. Merlin, A. Botchkarev, A. Salvador, and H. Morkoc, *J. Appl. Phys.* **77**, 6042 (1995).
10. C. Wetzel, E.E. Haller, H. Amano, and I. Akasaki, *Appl. Phys. Lett.* **68**, 2547 (1996).
11. M.A. Stroschio, *J. Appl. Phys.* **80**, 6864 (1996); H.B. Teng, J.P. Sun, G.I. Haddad, M.A. Stroschio, SiGi Yu, and K.W. Kim, *J. Appl. Phys.* **84**, 2155 (1998).
12. M.V. Kisin, V.B. Gorfinkel, M.A. Stroschio, G. Belenky, and S. Luryi, *J. Appl. Phys.* **82**, 2031 (1997).
13. L. Bergman, and R.J. Nemanich, *J. of Appl. Phys.* **78**, 6709 (1995).
14. E.S. Zouboulis, and M. Grimsditch, *Phys. Rev.* **B43**, 12490 (1991).
15. H. Herchen, and M.A. Cappelli, *Phys. Rev.* **B47**, 14193 (1993).
16. T.R. Hart, R.L. Aggarwal, and B. Lax, *Phys. Rev.* **B1**, 638 (1970).
17. E.T.M. Kernohan, R.T. Phillips, B.H. Bairamov, D.A. Ritchie, and M.Y. Simmons, *Sol. stat. commu.* **100**, 263 (1996).
18. B. Di Bartolo, *Optical Interactions in Solids*, (John Wiley & Sons, New York, 1968).
19. J. Menendez, and M. Cardona, *Phys. Rev.* **B29**, 2051 (1984).

20. P.G. Klemens, Phys. Rev. **148**, 845 (1966).
21. A.A. Maradudin. *Solid State Physics, Advances in Research and Applications*, P. 273, Vol. 18, Edited by E. Seitz, and D. Turnbull, (Academic Press, New York, 1966).
22. L.E. McNeil, M. Grimsditch, and R.H. French, J. Am. Ceram. Soc. **76**, 1132 (1993).
23. B.K. Ridley, J. Phys: Condens. Matter. **8**, L511, (1996).
24. C.M. Balkas, Z. Sitar, T. Zheleva, L. Bergman, R.J. Nemanich, and R.F. Davis. J. Crys. Growth **179**, 363 (1997).
25. C.M. Balkas, Z. Sitar, L. Bergman, I.K. Shmagin, J.F. Muth, R. Kolbas, R.J. Nemanich, and R.F. Davis, to be published in J. Crys. Growth, (1998).
26. C.M. Balkas, Z. Sitar, T. Zheleva, L. Bergman, I.K. Shmagin, J.F. Muth, R. Kolbas, R.J. Nemanich, and R.F. Davis, Mat. Res. Soc. Proc. Vol. 449, P. 41, 1997.
27. H. Bernstein, and G. Allen, J. Opt. Soc. Am. **45**, 237 (1955).
28. E.E. Whiting, J. Quant. Spectrosc. Radiat. Transfer. **8**, 1379 (1968).
29. A. Debernardi, Phys. Rev. **B57**, 12847 (1998).
30. D. J. Ecsedy, and P.G. Klemens, Phys. Rev. **B15**, 5957 (1977).
31. K.T. Tsen, D.K. Ferry, A. Botchkarev, B. Sverdlov, A. Salvador, and H. Morkoc, Appl. Phys. Lett. **72**, 2132 (1998).
32. B.C. Lee, K.W. Kim, M. Dutta, and M.A. Stroscio, Phys. Rev. **B56**, 997 (1997).
33. B.C. Lee, K.W. Kim, M.A. Stroscio, and M. Dutta, Phys. Rev. **B58**, 4860 (1998).
34. J.C. Nipko, and C.K. Loong, Phys. Rev. **B57**, 10550 (1998).
35. A.W. Hewat, Solid Stat. Commun. **8**, 187 (1970).

FIGURE CAPTIONS

Fig. 1. A micrograph of the transparent AlN crystallite; size $\sim 500 \times 50 \mu\text{m}$.

Fig. 2. The Raman spectrum (at $100 \mu\text{m}$ slit width) of the A1(TO) mode of the AlN crystallite. The line and the dashed line are the Lorentzian and the Gaussian fits to the data, respectively.

Fig. 3. The Raman spectra and the curve fit to the spectra of the transparent AlN crystallite (upper figure). The deconvoluted spectra is presented in the lower figure.

Fig. 4. The Raman spectra and the curve fit to the spectra of the blue AlN crystallite (upper figure). The deconvoluted spectra is presented in the lower figure.

Fig. 5. The Raman spectra of the E_2^1 mode of the transparent AlN (lower spectrum), and of the blue crystallite.

Fig. 6. The Raman spectra of the A1(LO) mode of the transparent AlN (lower spectrum) and of the blue crystallite.

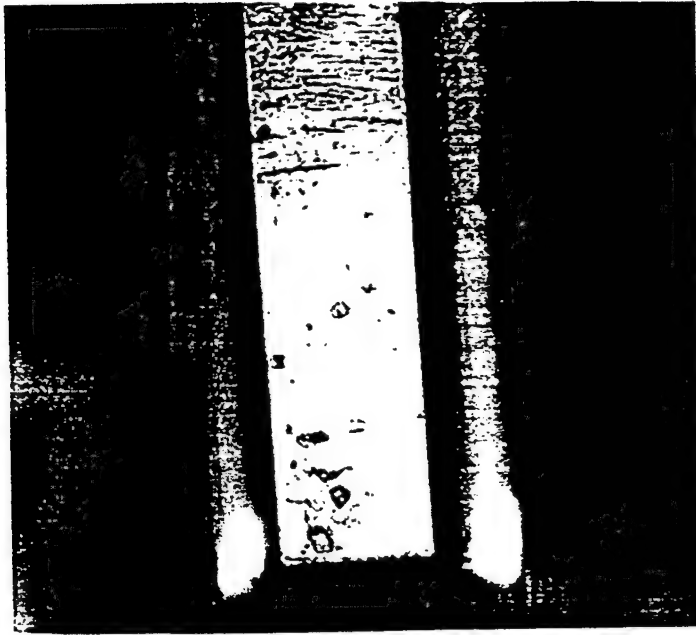
Fig. 7. The linewidth of the Raman mode as a function of the slit width. The squares represent the data of the blue AlN, and the dots of the transparent AlN. The lines are the fits to the data using Eq. 1.

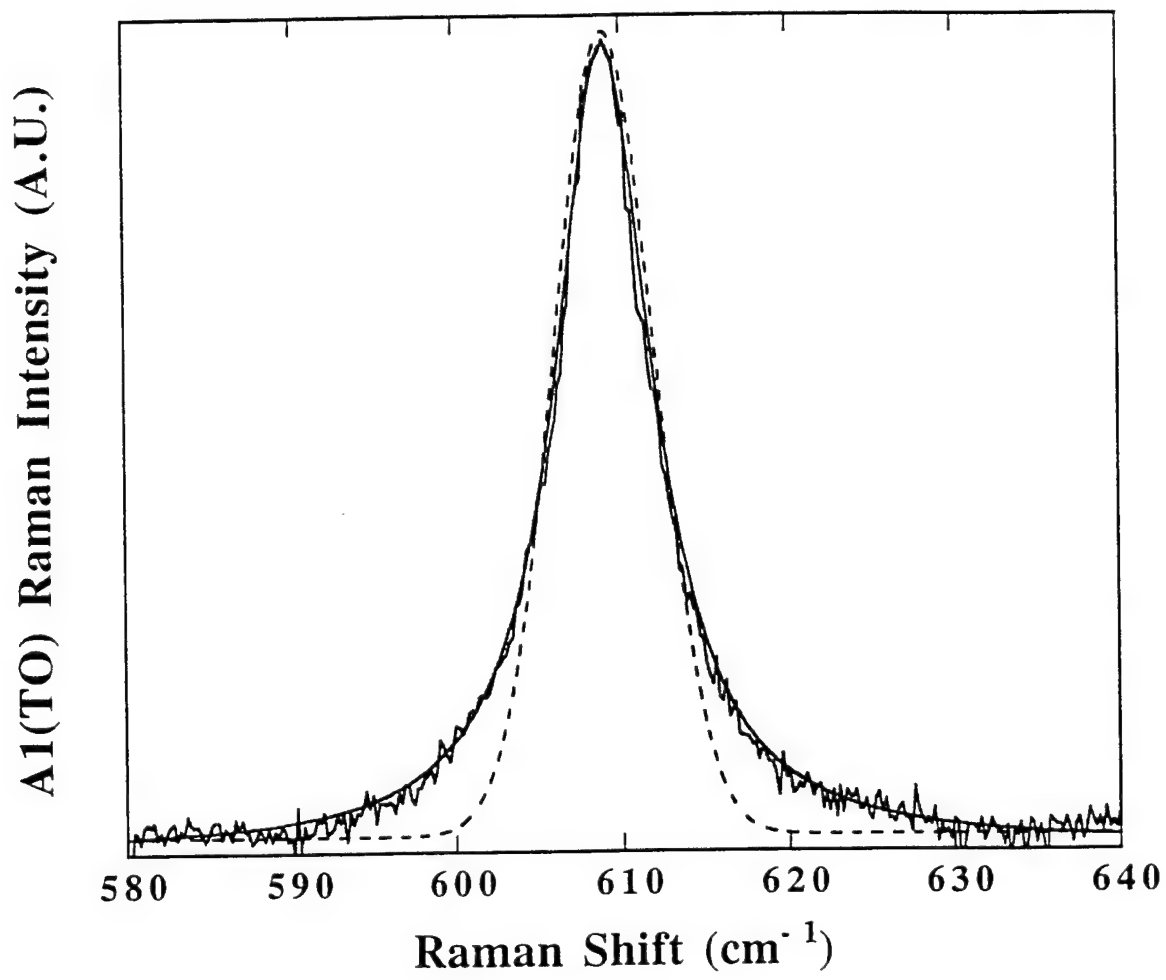
Fig. 8. The Raman spectra, the curve fit, and the deconvolution spectra of the GaN crystallite.

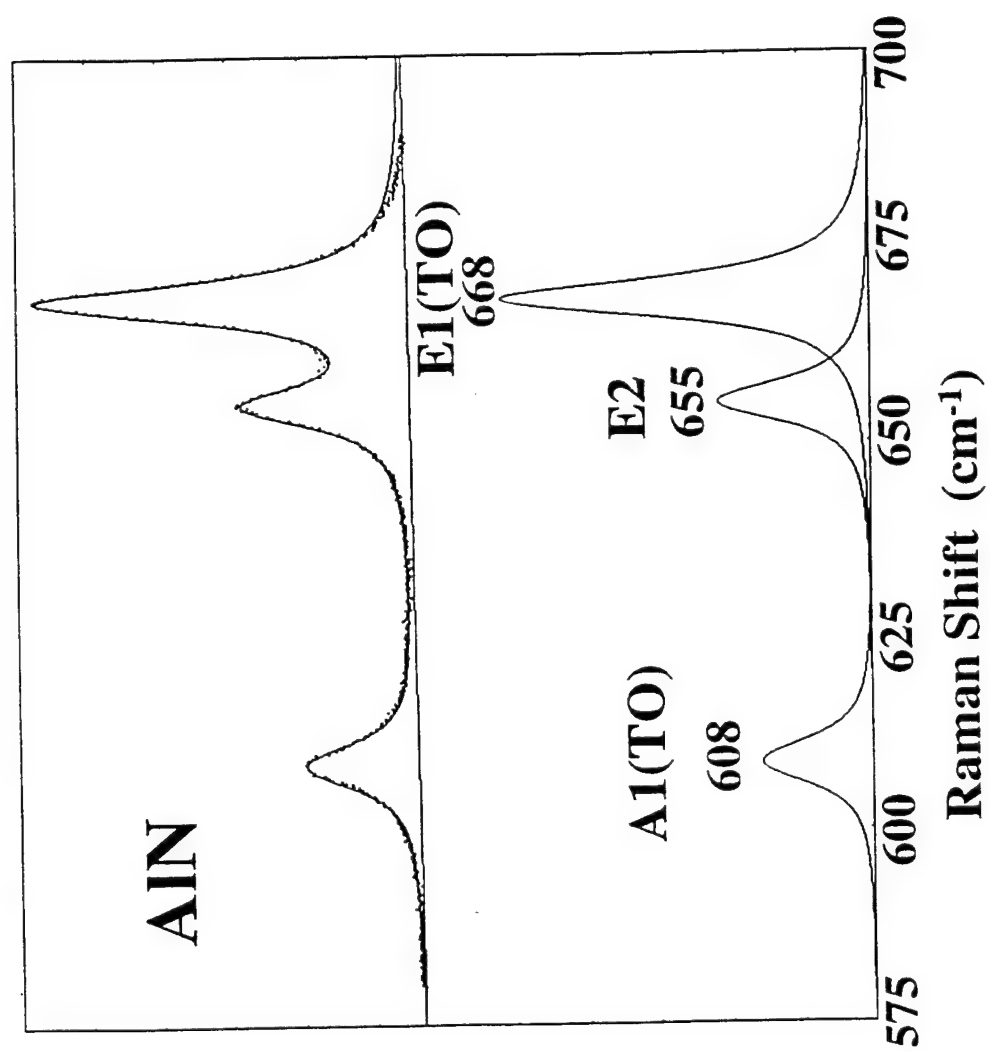
Fig. 9. The Raman spectra of the E_2^1 mode of the GaN crystallite.

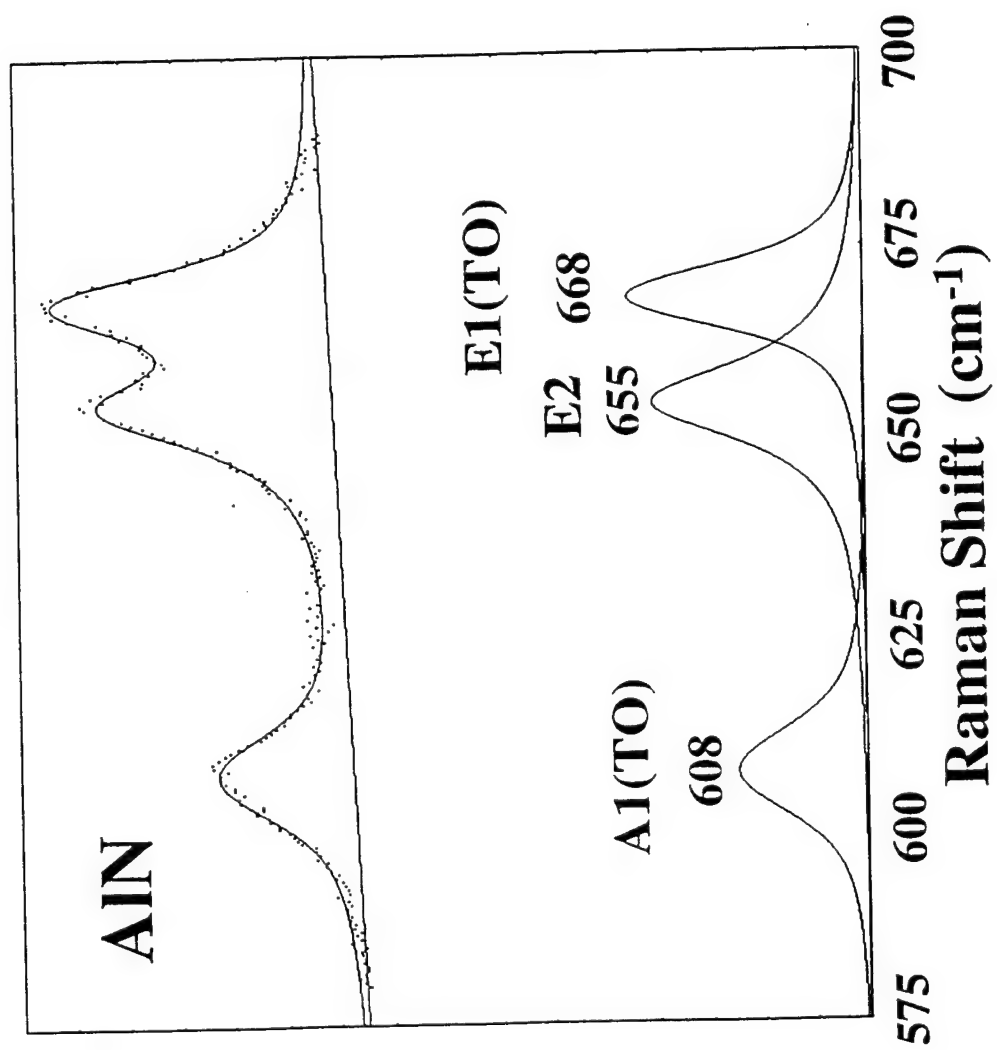
Fig. 10. The E_2^1 modes (lower curves) and the E_2^2 modes (upper curves) of the blue AlN (squares), ZnO (circles), and GaN (diamonds) as a function of the slit width.

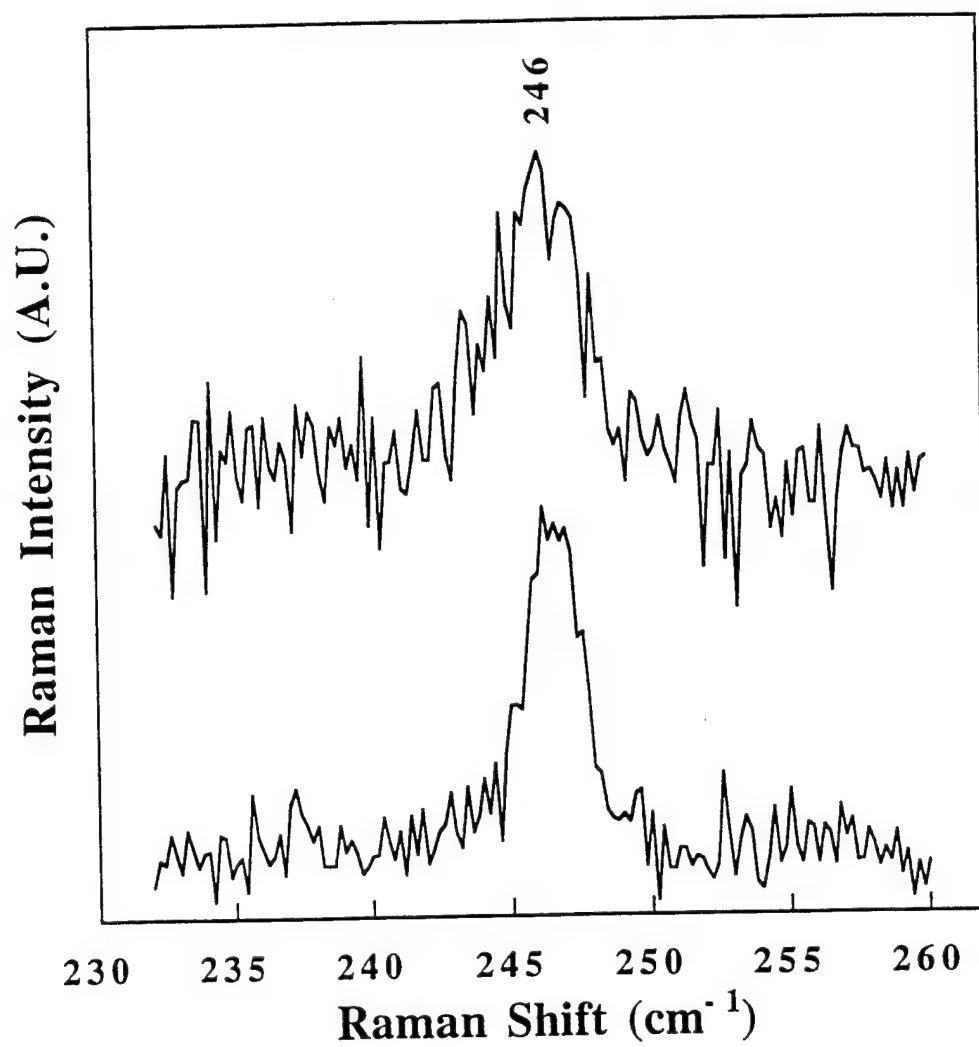
Fig. 11. The spectra ($200 \mu\text{m}$ slit width) of E_2^2 modes of GaN film at room temperature and at 10 K. The dashed line represents the Lorentzian fits to the data.

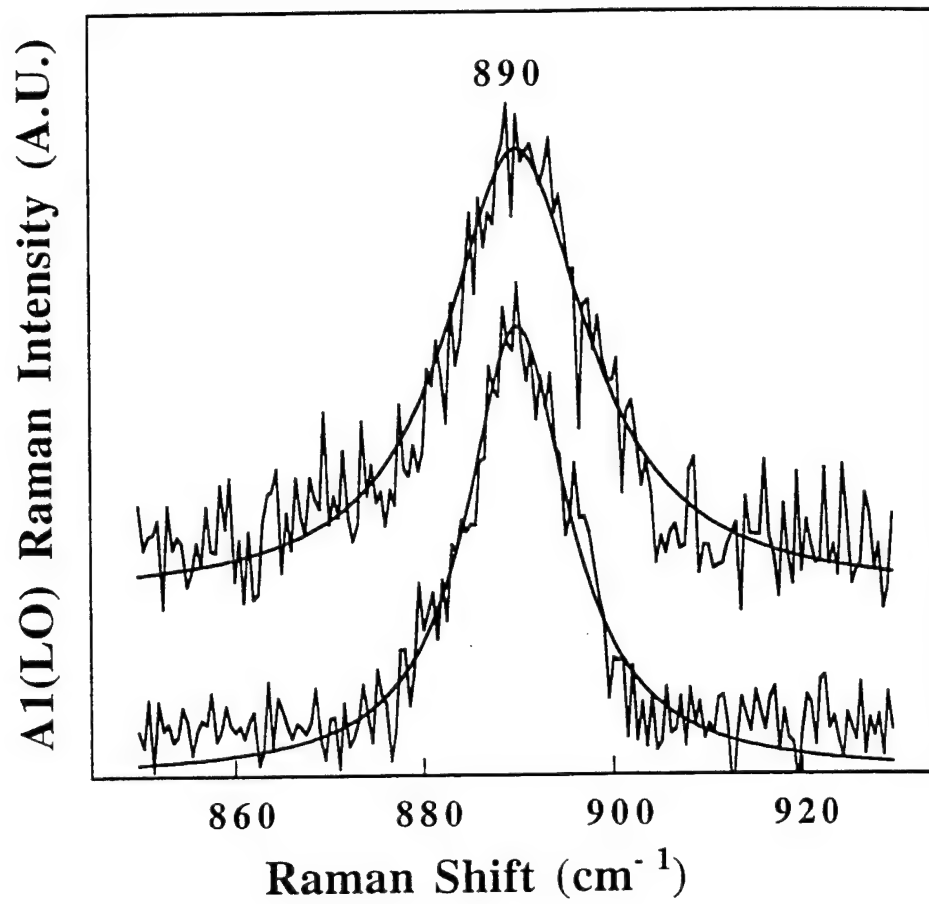


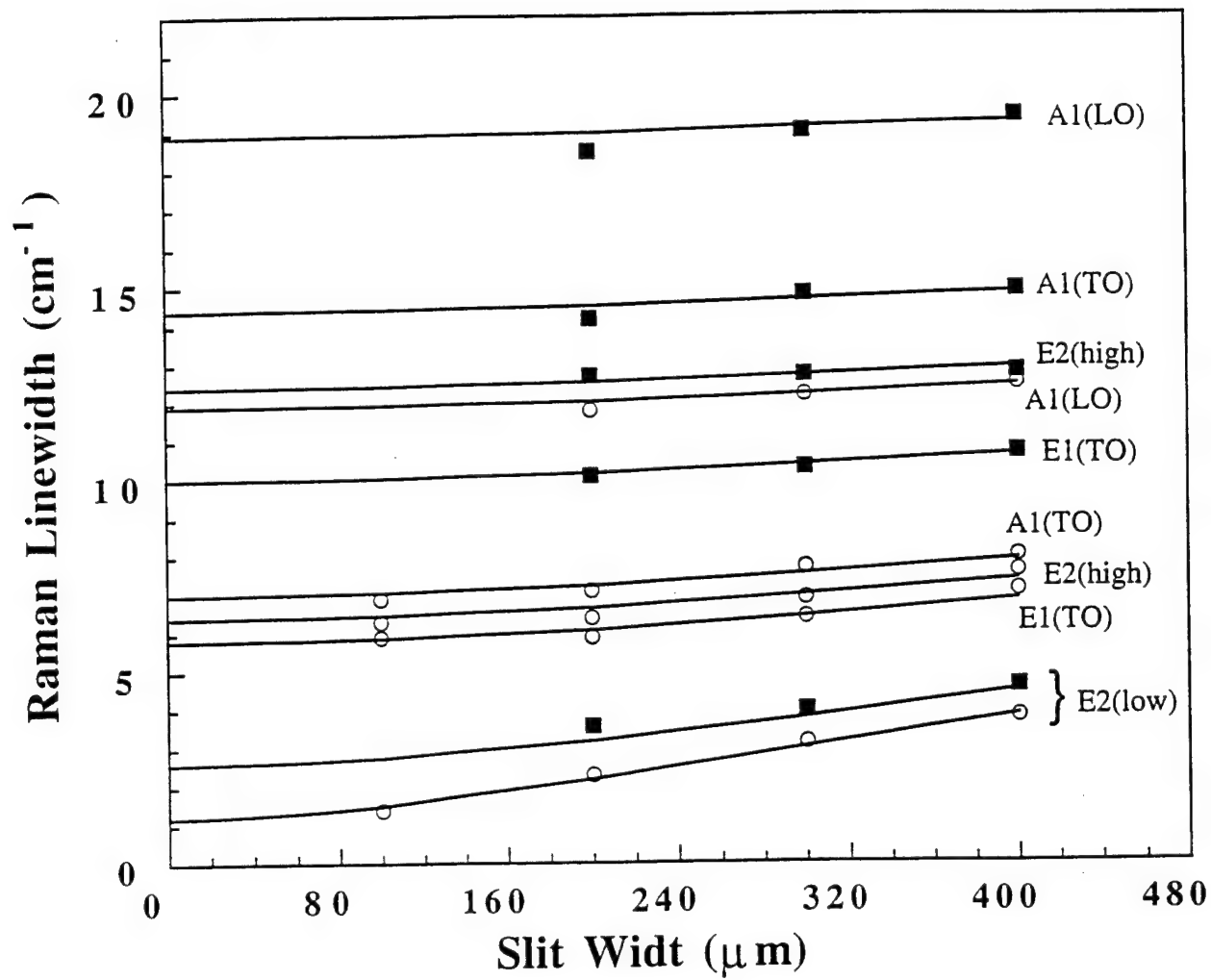


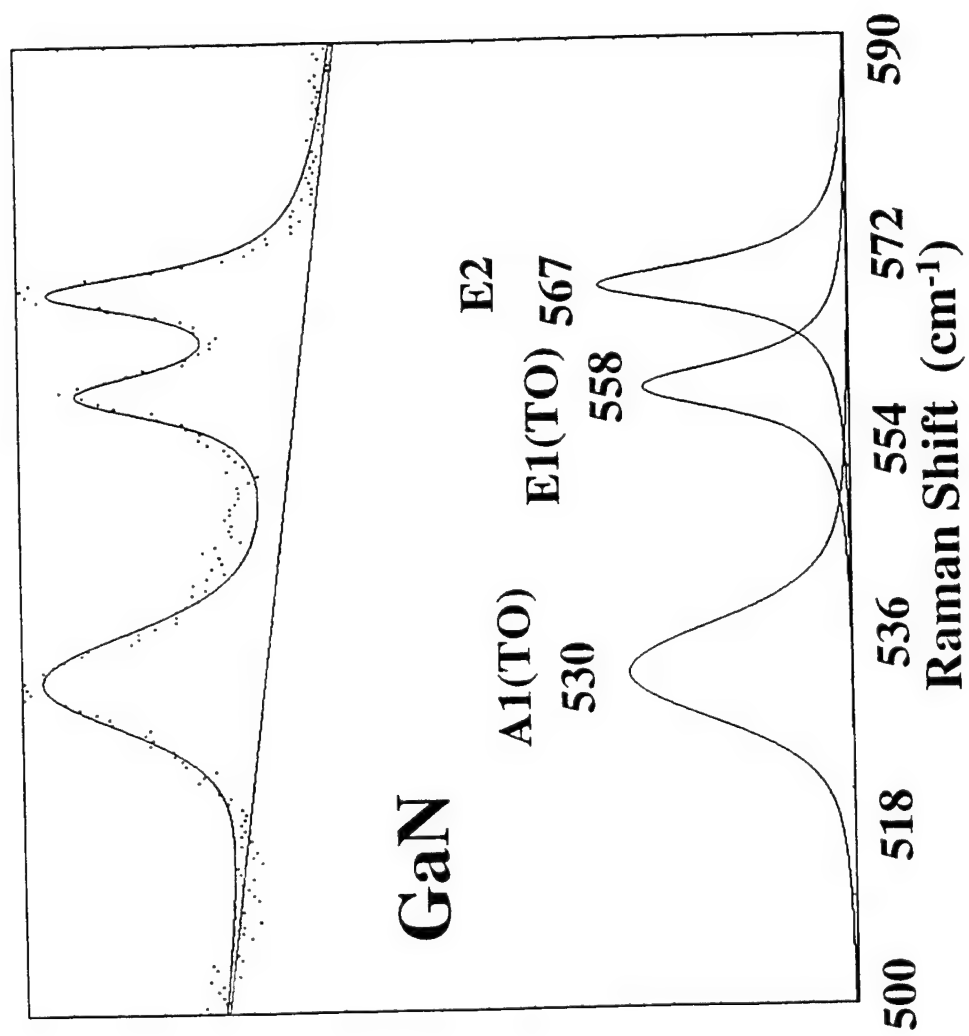


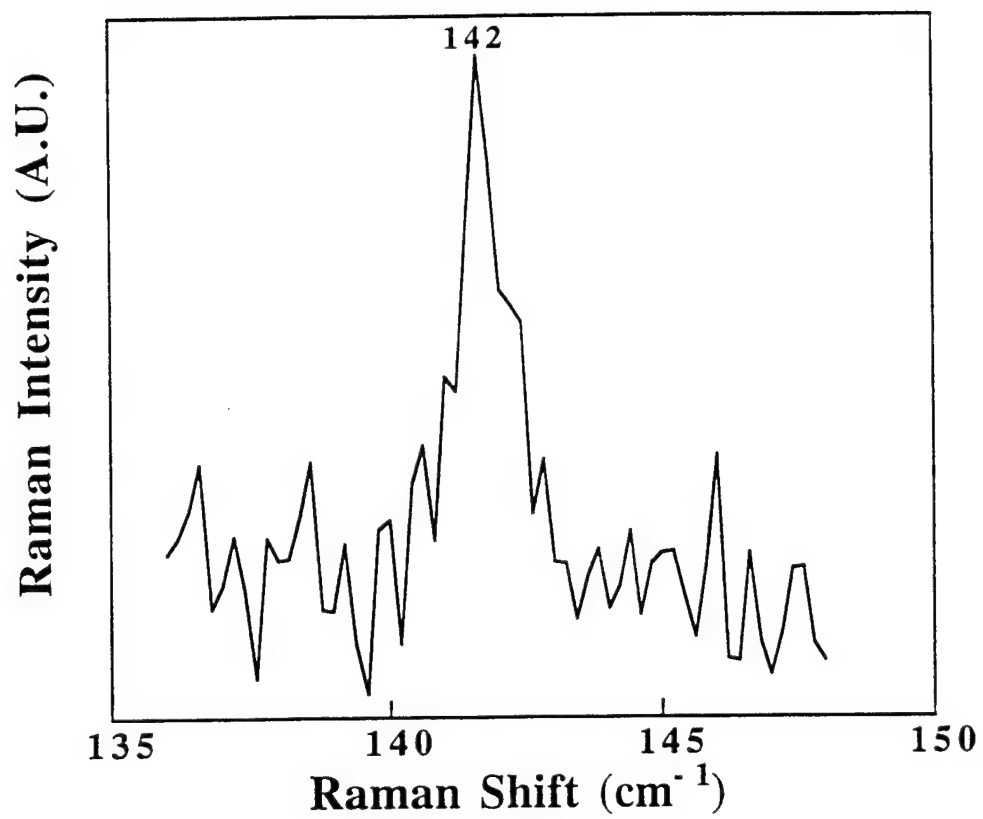


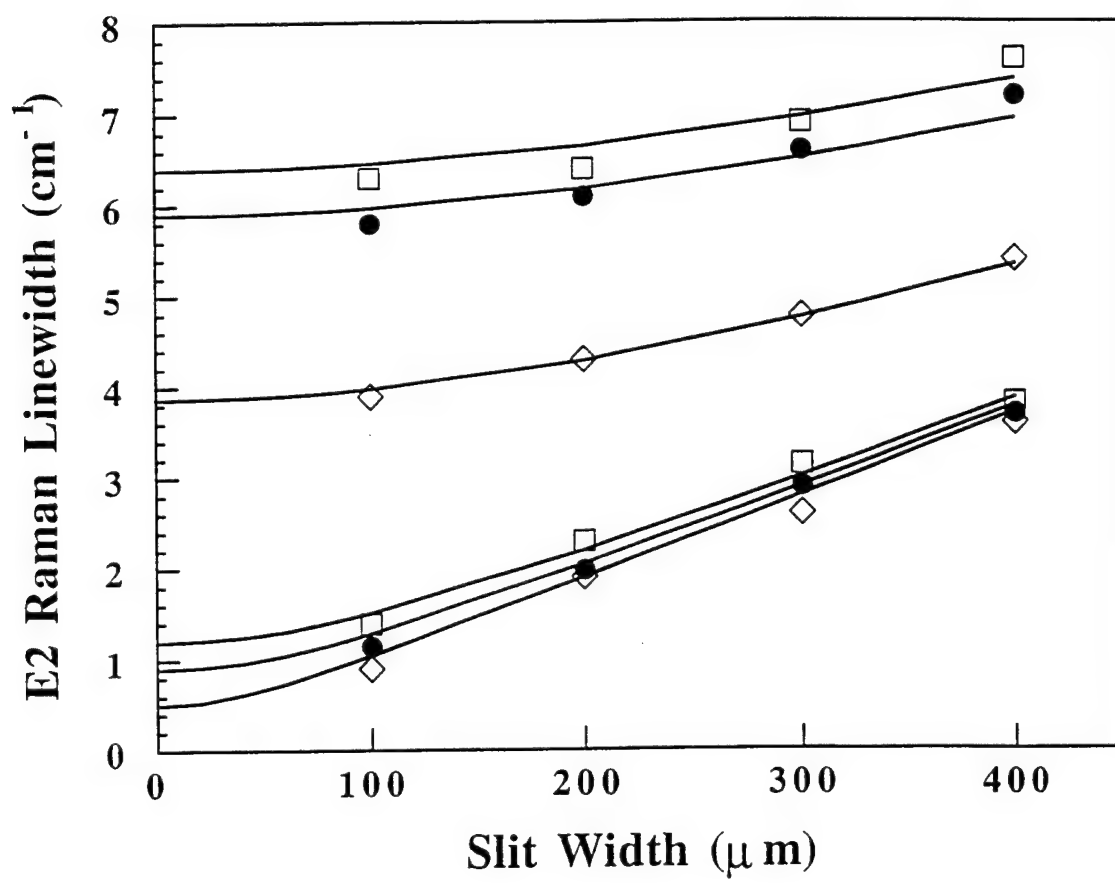


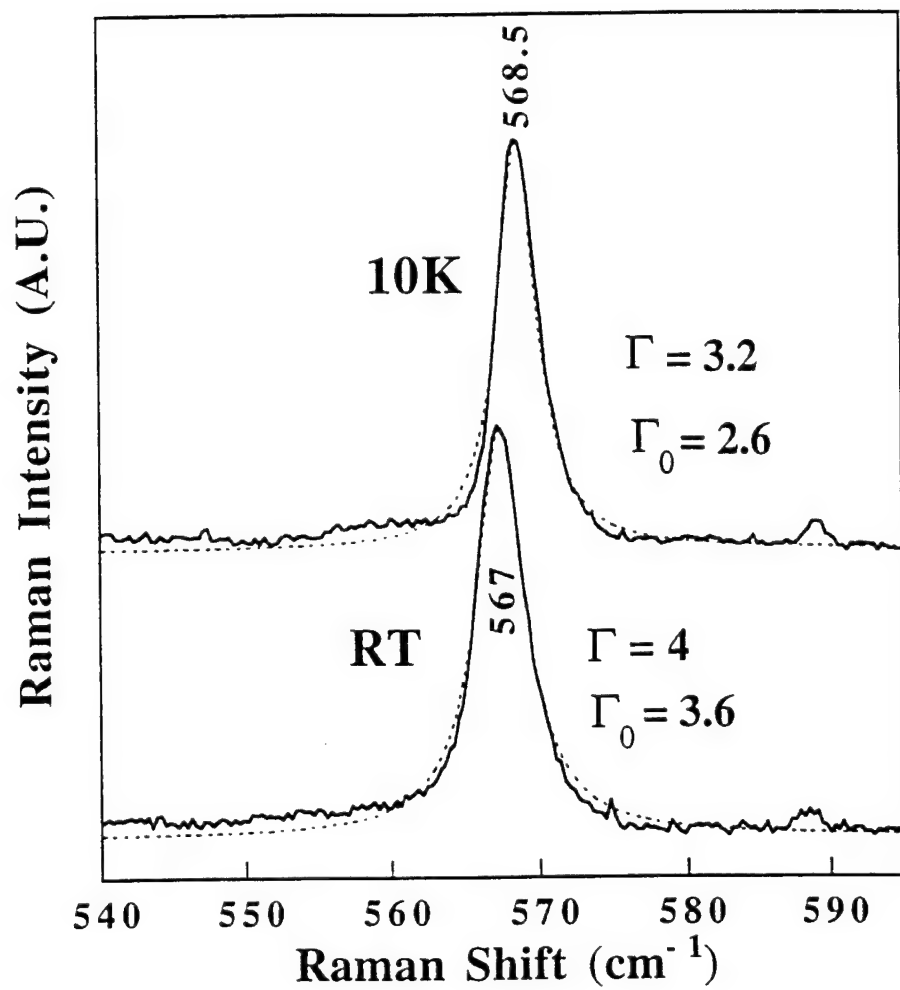












RAMAN ANALYSIS OF $\text{Al}_x\text{Ga}_{1-x}\text{N}$ FILMS

LEAH BERGMAN, MITRA DUTTA*, MICHAEL D. BREMSER**, OK-HYUN NAM**, WILLIAM G. PERRY**, DIMITRI ALEXSON, ROBERT F. DAVIS**, CENGIZ M. BALKAS**, and ROBERT J. NEMANICH.

Department of Physics, North Carolina State University, Raleigh, NC 27695-8202..

*US Army Research Office, Research Triangle Park, NC 27709-12211.

**Department of Materials Science and Engineering, North Carolina State University, Raleigh, NC 27695.

ABSTRACT

Raman analysis of the E2 mode of $\text{Al}_x\text{Ga}_{1-x}\text{N}$ in the composition range $0 \leq x \leq 1$ is presented. The lineshape was observed to exhibit a significant asymmetry and broadening toward the high energy range. The spatial correlation model is discussed, and is shown to account for the lineshape. The model calculations also indicate the lack of a long-range order in the CVD (chemical vapor deposition) alloys. These results were confirmed by X-ray scattering: the relative intensity of the superlattice line was found to be negligible. The line broadening of the E2 mode was found to exhibit a maximum at a composition $x \sim 0.5$ indicative of a random disordered alloy system. The stress state of the alloys was found to be tensile and was attributed to the difference in the thermal expansion coefficients of the SiC substrate and the film.

INTRODUCTION

Raman spectroscopy has been proven in the past to be a powerful method in studying alloy systems among which are $\text{Al}_x\text{Ga}_{1-x}\text{As}$, $\text{In}_x\text{Ga}_{1-x}\text{As}$, and many more [1-2]. Raman scattering from a perfect crystal, which consists of a lattice with translational symmetry, involves phonons with wavevector $q \approx 0$ near the Brillouin zone (BZ) center [3]. The alloying may destroy the configurational translational symmetry, and the phonons of $q \approx 0$ may be allowed to participate in the Raman scattering. As a result the Raman lineshape changes, and an investigation of the line characteristics may yield valuable information on the microstructure state of the alloy.

In this paper we present observations and analytical study of an asymmetric E2 Raman lineshape of $\text{Al}_x\text{Ga}_{1-x}\text{N}$ films. The asymmetry of the line is shown to agree with the spatial correlation model which is based on the relaxation of the $q \approx 0$ selection rules due to the alloying. The calculations indicated that the $\text{Al}_x\text{Ga}_{1-x}\text{N}$ lattice lacks a long range order, a result which was confirmed by X-ray diffraction: the superlattice diffraction line was found to exhibit a very weak relative intensity. Moreover, the functional behavior of the E2 linewidth with respect to the composition x in the range 0 - 1 indicated a random distribution of the alloy constituents with maximum disorder at composition $x \sim 0.5$.

In general, stress may be analyzed via the Raman peak position. However, the peak position of the alloy depends on the convoluted effects of the stress, the relaxation of the $q \approx 0$ selection rules, and the mode-type. These effects are functions of the composition; the stress is also a function of the lattice constants and the thermal expansion coefficients of the film-substrate system. Thus, in a sample of known spatially uniform composition, and with structural defects due to stress, the stress-type may be analyzed by acquiring spectra at a defect and at a defect-free region. Our analysis using this approach indicates that the AlGa_N alloys are under tensile stress. The stress is suggested to be due to the difference in thermal expansion coefficients of the film and the SiC substrate.

EXPERIMENT

Raman spectra were acquired in a backscattering geometry in which the E2 is an allowed Raman mode from the c-face of the Wurtzite structure [4]. In the experiments the 488 nm line of an Ar^+ ion laser was utilized and the data were acquired at sample temperatures of 300K and 10K. The data for the lineshape investigation were acquired in a macro mode of laser spot size ~ 2 mm;

for the stress measurements the micro mode of spot size $\sim 3 \mu\text{m}$ was utilized. The experimental error in the linewidth and peak position measurements is $\pm 1.5 \text{ cm}^{-1}$ and 0.5 cm^{-1} respectively. The $\text{Al}_x\text{Ga}_{1-x}\text{N}$ films were grown via the organometallic chemical vapor deposition (OMCVD) method at $\sim 1100^\circ\text{C}$ on $6\text{H-SiC}(0001)$ substrates with a 100 nm AlN buffer layer. The thickness of the films is $\sim 2 \mu\text{m}$ and the composition, x , which was determined via Rutherford backscattering (RBS), energy dispersive X-ray (EDX), and Auger spectroscopy, is: 0.06, 0.12, 0.22, 0.32, and 0.70. The Raman data points for $x=0$ and $x=1$ were obtained from GaN film and AlN crystallite respectively.

RESULTS AND DISCUSSION

The Configurational Disorder in AlGaIn Films

Figure 1 shows the room-temperature Raman spectra of the E2 line from $\text{Al}_x\text{Ga}_{1-x}\text{N}$ films of compositions 0.06, 0.12, 0.22, and 0.70, which exhibit linewidths Γ of 8, 13, 16, and 19 cm^{-1} respectively. As depicted in the figure, the spectral lineshape for films of $x>0.06$ exhibit asymmetric broadening and a peak shift toward higher frequency. Possible line broadening mechanisms applicable to alloys include thermal broadening, activation of a symmetry forbidden zone-center ($q=0$) mode which lies in the same frequency range as the investigated line, and broadening due to activation of a collection of modes of wavevectors $q \geq 0$. The last two broadening mechanisms result from the elimination of the translational symmetry of the lattice due to alloying.

To investigate the thermal contribution to the line broadening, Raman spectra were acquired at $T=10\text{K}$, and no significant change was observed between the shapes and linewidths of the room and cold temperature spectra. Thus the linewidth in our sample is not strongly affected by temperature. The only effect of the low temperature is the shifting of the peak position by $\sim 2 \text{ cm}^{-1}$ toward higher frequency, which was also previously observed in GaN films [5] and crystals [6] and was attributed there to the thermal contraction of the bonding.

The second possible mechanism is the activation of a $q=0$ symmetry forbidden mode which might be convoluted with the E2 line and cause the asymmetric broadening. However, the only mode in the frequency range of the E2 line that is forbidden in the back-scattering geometry is the $\text{A}_1(\text{TO})$ mode of GaN at $\sim 560 \text{ cm}^{-1}$ which lies at a lower frequency.

A more plausible mechanism to account for the high frequency asymmetric linewidth in our Raman spectra is the spatial correlation model, also known as the confinement model. The model was developed to explain the asymmetry line in BN [7] and Si [8] and has been successfully applied to quantify the lineshape behavior of $\text{Ga}_{1-x}\text{Al}_x\text{As}$ and $\text{Ga}_{1-x}\text{In}_x\text{As}$ alloy systems [1]. The foundation of the model lies in attributing the relaxation of the $q=0$ Raman selection rules to the phonon confinement in a finite domain of size L . The size of L in an alloy system may be viewed as the average size of the ordered domains which are embedded in the configurational-disordered matrix. According to the model, as L gets smaller, the range of wavevectors Δq becomes larger: a wider range of frequencies are allowed to participate in the Raman scattering, and as a result the Raman lineshape exhibits a change. The lineshape-change depends on the phonon dispersion curve $\omega(q)$; for a curve of negative slope the line asymmetry is toward lower frequencies and for a positive slope the asymmetry is toward higher frequencies. The peak position also shifts accordingly. However, the position is a function of the stress and the alloy-mode as well: an alloy can be categorized as being a one- or two- mode type [9] and the behavior of the peak position depends on the type. The deconvolution of the peak position is left to a future investigation; at present we address merely the origin of the asymmetric lineshape and line broadening.

The Raman intensity $I(\omega)$ for the spatial correlation model may be expressed as [1, 7-8]

$$I(\omega) \propto \int \exp\left(\frac{-q^2 L^2}{4}\right) \times \frac{d^3 q}{[\omega - \omega(q)]^2 + \left(\frac{\Gamma_0}{2}\right)^2} \quad (1)$$

where q is in units of $2\pi/a$, a is the lattice constant, and Γ_0 is the linewidth of the material of composition $x=0$ which is GaN in this study. Our GaN films exhibit linewidths in the range of

3-5 cm^{-1} depending on the film quality. For the calculations we used the upper range value to account for the stress in the alloy which was inferred from the appearance of cracks in the films. In the calculation we assumed a spherical correlation domain and BZ.

To evaluate Equation 1 we fitted the phonon dispersion curves, which have been calculated by Azuhata et al [10], in the vicinity of BZ center. In their calculations the E2 mode along the Δ direction exhibits a doubly degenerate behavior and is a weak function of q , thus having no effect on the line broadening mechanism. In contrast, the E2 curves along the Σ and T directions both split into a lower and an upper branch, where the former is a decreasing function of q and the latter is an increasing function; these curves are expected to influence the Raman lineshape. Our calculations of Eq. 1 best concur with the phonon dispersion curve of the form: $\omega(q) = A + Bq^2$ (in units of cm^{-1} and with $A=568$ and $B=100$) which is the approximated behavior of the upper branch of the Σ and T curves in the vicinity of the zone center. However, when we included the contribution to the lineshape arising from the lower branches of the dispersion curves the fit was not ideal. Similar behavior has been previously observed in the calculation of BN lineshape [7]. The reason for the dominance affect of the upper branches in our calculations is under investigation.

The calculated lines and the Raman data for samples of composition 0.12 and 0.22 are presented in Figure 1. As depicted in the figure the asymmetric Raman data concur with the spatial correlation model, where the small deviation $\sim 560 \text{ cm}^{-1}$ may be attributed to the activated $A_1(\text{LO})$ mode. The ordered domain size, L , was determined from our calculations to be $\sim 2.5 - 3.5 \text{ nm}$; a relatively small value suggesting the lack of a long range order in the alloy system. In order to further investigate this hypothesis a film of composition $x=0.22$ was characterized by XRD: the scan is presented in Figure 2. The figure shows the diffraction peak of the (0002) planes of the AlGa_xN (superimposed is also the SiC substrate peak) and the inset presents the weak (0001) diffraction peak. The (0001) is a forbidden reflection in the WZ structure and appears as a superlattice line only when lattice ordering exists [11]; the intensity ratio (0001)/(0002) is a measure of the extent of the order [12]. Al_xGa_{1-x}N films which were grown by molecular beam epitaxy have been reported by Korakakis et al [11] to exhibit a long range order; the intensity ratio of their XRD lines is ~ 0.05 in contrast to our much smaller intensity ratio of ~ 0.002 . Thus the XRD confirms the Raman analysis, indicating that the alloys in this study do not exhibit significant long range ordering. More insight into the alloy micro-structure may be obtained from the Raman linewidth behavior. Figure 3 presents the Raman linewidth of the E2 mode as a function of the composition. The linewidth behavior follows a pattern which exhibits a maximum at composition $x \sim 0.5$, a value at which a maximum disorder should be expected in a random system. Thus our data suggest that the distribution of the alloy constituents for the most part is random.

The Stress State of the AlGa_xN Films

The morphology of our AlGa_xN films consists of uniformly distributed crack density which is indicative of the high stress state present in the films. In general, stress may be analyzed via the shifting of the Raman peak position. However, as mentioned the Raman peak position of the alloy depends on the combined effects of the stress, the relaxation of the $q \equiv 0$ selection rules, and the mode-type. All these effects are functions of the composition; the stress, however, is also a function of the lattice constants and the thermal expansion coefficients of the film-substrate system.

In order to determine the stress-type in the alloy we took advantage of the film morphology: Micro-Raman spectra were acquired at a crack region, where the film is relatively relaxed, and at a region remote from the crack, where the film is strained. Figure 4 shows characteristic spectra of the relaxed and strained regions. The linewidth of both spectra is $\sim 16 \text{ cm}^{-1}$ implying that no significant spatial variation of composition, x , occurs across the film. Since the composition is similar in the relaxed and the strained regions, the Raman peak position is influenced mainly by the stress effects due to the film-substrate thermal and lattice mismatch. As can be observed in the figure, the peak position of the strained region exhibits a shift of $\sim 3 \text{ cm}^{-1}$ towards lower frequencies relative to the peak of the relaxed region suggesting that the original stress state of the film (before relaxation via cracking occurs) is tensile.

A source of the tensile stress in the alloys may be the difference in the thermal expansion coefficients, α , of the film, the buffer-layer, and the substrate at the elevated temperature (1400 K)

at which our films were grown. The α 's of GaN and SiC at this temperature range have not yet been measured. However, at ~ 750 K the thermal expansion coefficients along the a axis (α_a) and c axis (α_c) have been measured [13]; for GaN, $\alpha_a=6.2$ and $\alpha_c=6.1$, and for SiC $\alpha_a=4.2$ and $\alpha_c=4.0$, where α is in units of 10^{-6} K^{-1} . The average thermal expansion coefficients of AlN at 750 K and 1200 K have been reported to be 5.8 and $6.2 \times 10^{-6} \text{ K}^{-1}$ respectively [14]. The smaller value of the SiC thermal coefficient relative to that of the alloy constituents thus may be the cause of the tensile stress in our films. To acquire further insight into this issue, the Raman spectra of AlN film, grown under similar conditions as the alloys, was compared to that of AlN crystallite. The spectra are presented in Figure 5 (the spectrum of the crystallite was acquired with a backscattering geometry from the a-face for which the E1(TO) is an allowed mode as well). As can be seen in the figure, the AlN Raman peak of the film exhibits a tensile shift of $\sim 4 \text{ cm}^{-1}$ relative to the peak position 656 cm^{-1} of the crystal. A result suggestive of the presence of stress in the film due to the different coefficients of thermal expansion..

CONCLUSIONS

The asymmetric behavior of the E2 Raman lineshape of $\text{Al}_x\text{Ga}_{1-x}\text{N}$ alloys was attributed to the activation of phonons of $q \geq 0$ arising from the disordered state of the alloys. The line broadening of the E2 Raman mode exhibits a maximum at composition $x \sim 0.5$ which is consistent with a random distributed system. X-ray diffraction supports these findings: the superlattice relative line-intensity is weak. The alloy exhibits tensile stress which is suggested to be due to interfacial thermal mismatch.

ACKNOWLEDGMENTS

We gratefully acknowledge the National Research Council, the Army Research Office, and the Office of Naval Research for supporting this research.

REFERENCES

1. P. Parayanthal, and F.H. Pollak, Phys. Rev. Lett. **52**, 1822 (1984).
2. L. Bergman, M.D. Bremser, W.G. Perry, R.F. Davis, M. Dutta, and R.J. Nemanich, Appl. Phys. Lett. **71**, 2157 (1997).
3. Topics in Applied Physics-Light Scattering in Solids I, Edited by M. Cardona, (Springer-Verlag, New York, 1983).
4. C. A. Arguello, D.L. Rousseau, and S.P.S. Porto, Phys. Rev. **181**, 1351 (1969).
5. L. Bergman, M.D. Bremser, J.A. Christman, S.W. King, R.F. Davis, and R.J. Nemanich, Mat. Res. Soc. Symp. Proc. **449**, 725 (1997).
6. D.D. Manchon, A.S. Baker, P.J. Dean, and R.B. Zetterstorm, Sol. Stat. Commu. **8**, 1227 (1970).
7. R.J. Nemanich, S.A. Solin, and R.M. Martin, Phys. Rev. **B23**, 6348 (1981).
8. P.M. Fauchet, and I.H. Campbell, Critical Reviews in Solid State and Materials Science **14**, S79 (1988).
9. K. Hayashi, K. Itoh, N. Sawaki, and I. Akasaki, Sol. Stat. Commu. **77**, 115 (1991).
10. T. Azuhata, T. Matsunaga, K. Shimada, K. Yoshida, T. Sota, K. Suzuki, and S. Nakamura, Physica **B219/220**, 493 (1996).
11. D. Korakakis, H.M. Ng, K.F. Ludwig Jr., and T.D. Moustakas, Mat. Res. Soc. Symp. Proc. **449**, 233 (1997).
12. B.D. Cullity, Elements of X-Ray Diffraction, (Addison-Wesley, Menlo Park, 1978).
13. M. Leszczynski, T. Suski, P. Perlin, H. Teisseyre, I. Grzegory, M. Bockowski, J. Jun, S. Porowski, and J. Major, J. Phys. D: Appl. Phys. **28**, A149 (1995).
14. G.A. Slack and S.F. Bartram, J. Appl. Phys. **46**, 89 (1975).

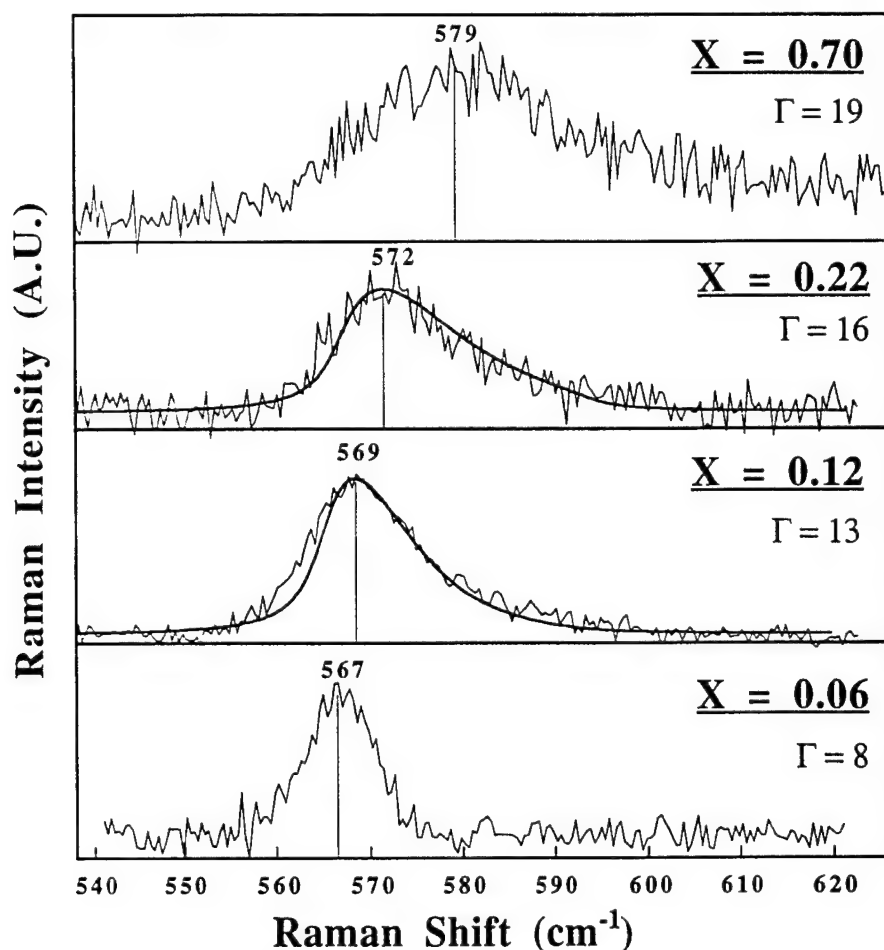


FIG. 1. The Raman spectra of the E2 mode of films of various composition x . The solid lines were calculated from the spatial correlation model (Eq. 1).

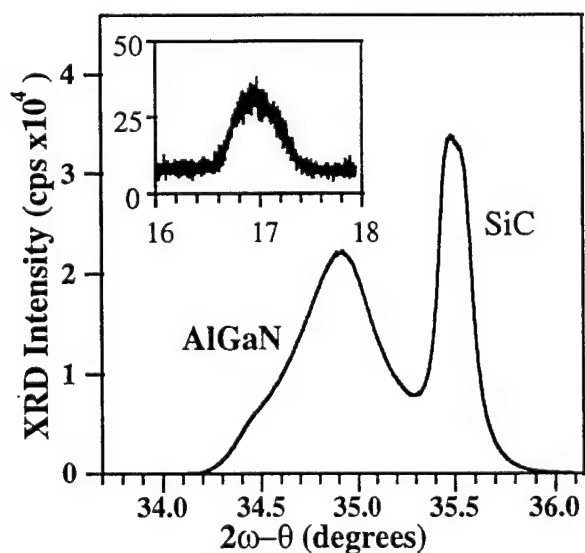


FIG. 2. The (0002) x-ray diffraction of film of $x=0.22$. The inset shows the very weak (0001) superlattice line.

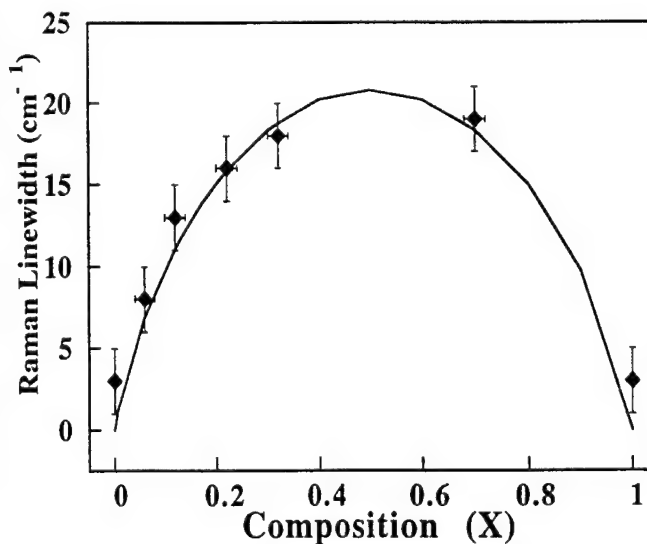


FIG. 3. The E2 Raman linewidth as a function of composition x .

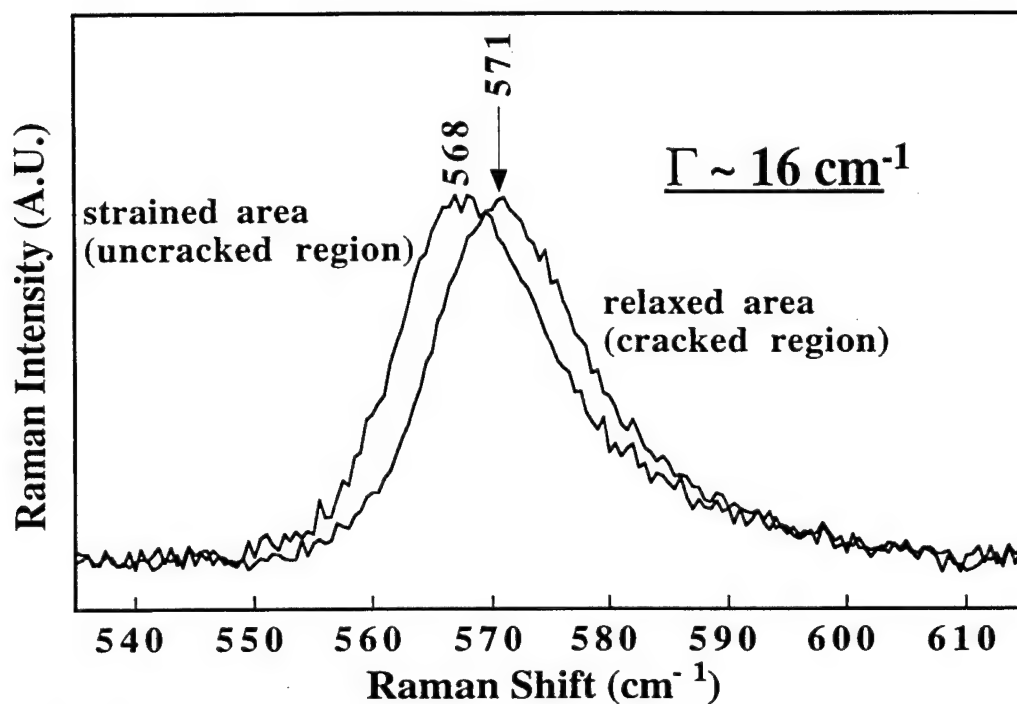


FIG. 4. The Raman spectra of the E2 mode acquired at a relaxed and at a strained region of AlGaN film of composition $x=0.22$.

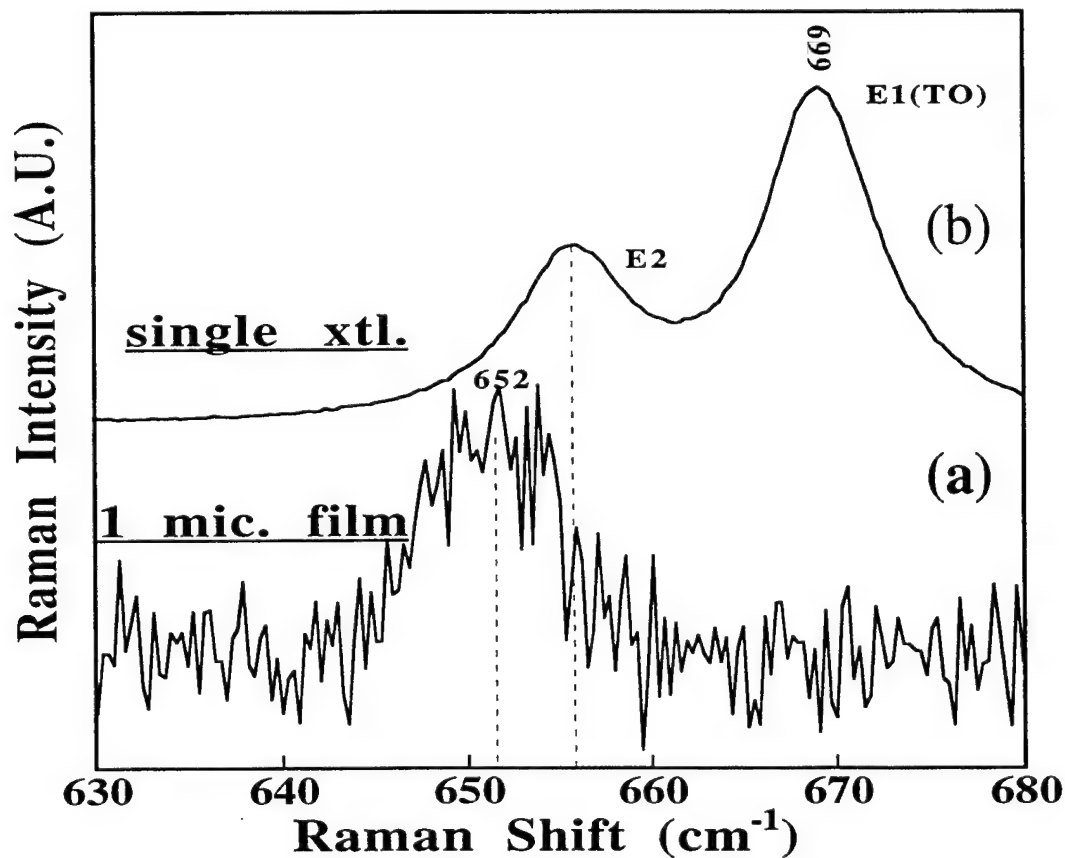


FIG. 5. Raman spectra of (a) AlN film grown on SiC substrate and (b) AlN crystal.

Raman Analysis of the Configurational Disorder in $\text{Al}_x\text{Ga}_{1-x}\text{N}$ films

Leah Bergman, Michael D. Bremser^{a)}, William G. Perry^{a)}, Robert F. Davis^{a)}, Mitra Dutta^{b)}, and Robert J. Nemanich.

Department of Physics, North Carolina State University, Raleigh, NC 27695-8202.

ABSTRACT

Raman analysis of the E2 mode of $\text{Al}_x\text{Ga}_{1-x}\text{N}$ in the composition range $0 \leq x \leq 1$ is presented. The lineshape was observed to exhibit a significant asymmetry and broadening toward the high energy range. The spatial correlation model is discussed, and is shown to account for the lineshape. The model calculations also indicate the lack of a long-range order in the chemical vapor deposition (CVD) alloys. These results were confirmed by X-ray scattering: the relative intensity of the superlattice line was found to be negligible. The line broadening of the E2 mode was found to exhibit a maximum at a composition $x \cong 0.5$ indicative of a random disordered alloy system.

^{a)}Department of Materials Science and Engineering, North Carolina State University, Raleigh, NC 27695.

^{b)}US Army Research Office, Research Triangle Park, NC 27709-12211.

The realization of achieving high quality $\text{Al}_x\text{Ga}_{1-x}\text{N}$ films has prompted intensive investigation concerning device fabrication and material and device properties. Raman spectroscopy has been proven in the past to be a powerful method in studying alloy systems among which are $\text{Al}_x\text{Ga}_{1-x}\text{As}$, $\text{In}_x\text{Ga}_{1-x}\text{As}$, $\text{Ca}_x\text{Sr}_{1-x}\text{F}_2$, $\text{ZnS}_{1-x}\text{Se}_x$, and many more [1-5]. Raman scattering from a perfect crystal, which consists of a lattice with translational symmetry, involves phonons with wavevector $q \approx 0$ near the Brillouin zone (BZ) center [6]. The alloying may destroy the configurational translational symmetry, and the phonons of $q \approx 0$ may be allowed to participate in the Raman scattering. As a result the Raman lineshape changes, and an investigation of the line characteristics may yield valuable information on the microstructure state of the alloy.

In this Letter we present for the first time observations and analytical study of an asymmetric E2 Raman lineshape of $\text{Al}_x\text{Ga}_{1-x}\text{N}$ films. The asymmetry of the line is shown to agree with the spatial correlation model which is based on the relaxation of the $q \approx 0$ selection rules due to the alloying. The calculations indicated that the $\text{Al}_x\text{Ga}_{1-x}\text{N}$ lattice lacks a long range order, a result which was confirmed by X-ray diffraction (XRD): the superlattice diffraction line was found to exhibit a very weak relative intensity. Moreover, the functional behavior of the E2 linewidth with respect to the composition x in the range 0 - 1 indicated a random distribution of the alloy constituents with maximum disorder at composition $x \approx 0.5$.

Raman spectra were acquired in a backscattering geometry in which the E2 and the A1(LO) are the allowed Raman modes from the c-face of the Wurtzite (WZ) structure [7]. Unlike the non-polar E2 mode, the A1(LO) mode possesses an electric field which interacts with that produced by the free carrier waves known as plasmons. For samples with a sufficiently high free carrier concentration, this phonon-plasmon interaction affects the A1(LO) Raman lineshape significantly and results in a Raman signal with very weak intensity [8]. The free carrier concentration in the samples studied here, as measured via the Hall effect, is relatively high (on the order of $5 \times 10^{17}/\text{cm}^3$) and as a result the A1(LO) mode is not detectable in the Raman spectra. The lack of the electric field interaction makes the E2 mode ideal for the present study. Future investigations may address the lineshape of the A1(LO) mode.

In the experiments the 488 nm line of an Ar⁺ ion laser was utilized and the data were acquired at sample temperatures of 300K and at 10K. The experimental error in the linewidth and peak position measurements is $\pm 1.5 \text{ cm}^{-1}$ and 0.5 cm^{-1} respectively. The Al_xGa_{1-x}N films were grown via the organometallic chemical vapor deposition (OMCVD) method at $\sim 1100^\circ\text{C}$ on 6H-SiC(0001) substrates with a 1000 \AA AlN buffer layer [9]. The thickness of the films is $\sim 2 \mu\text{m}$ and the composition, x , which was determined via Rutherford backscattering (RBS), energy dispersive X-ray (EDX), and Auger spectroscopy, is: 0.06, 0.12, 0.22, 0.32, and 0.70. The data points for $x=0$ and $x=1$ were obtained from GaN film and AlN crystallite [10] respectively.

Figure 1 shows the room-temperature Raman spectra of the E2 line from Al_xGa_{1-x}N films of compositions 0.06, 0.12, 0.22, and 0.70, which exhibit linewidths of 8, 13, 16, and 19 cm^{-1} respectively. As depicted in the figure, the spectral lineshape for films of $x>0.06$ exhibit asymmetric broadening and a peak shift toward higher frequency. Possible line broadening mechanisms applicable to alloys include thermal broadening, activation of a symmetry forbidden zone-center ($q\equiv 0$) mode which lies in the same frequency range as the investigated line, and broadening due to activation of a collective of modes of wavevectors $q\geq 0$. The last two broadening mechanisms result from the elimination of the translational symmetry of the lattice due to alloying.

To investigate the thermal contribution to the line broadening, Raman spectra were acquired at $T=10\text{K}$, and no significant change was observed between the shapes and linewidths of the room and cold temperature spectra. Thus the linewidth in our sample is not strongly affected by temperature. The only effect of the low temperature is the shifting of the peak position by $\sim 2 \text{ cm}^{-1}$ toward the high frequency, which was also previously observed in GaN films [8] and crystals [11] and was attributed there to the thermal contraction of the bonding.

The second possible mechanism is the activation of a $q\equiv 0$ symmetry forbidden mode which might be convoluted with the E2 line and cause the asymmetric broadening. However, the only mode in the frequency range of the E2 line that is forbidden in the back-scattering geometry is the A1(TO) mode of GaN at $\sim 560 \text{ cm}^{-1}$ [7] which lies at a lower frequency.

A more plausible mechanism to account for the high frequency asymmetric linewidth in our Raman spectra is the spatial correlation model, also known as the confinement model. The model was developed to explain the asymmetry line in BN [12] and Si [13] and has been successfully applied to quantify the lineshape behavior of $\text{Ga}_{1-x}\text{Al}_x\text{As}$ and $\text{Ga}_{1-x}\text{In}_x\text{As}$ alloy systems [1]. The foundation of the model lies in the wavevector uncertainty: $\Delta q = 2\pi/L$ where Δq is the phonon wavevector range, L is a spatial dimension into which the phonon is confined, and q is related to the Raman frequency ω via the phonon dispersion relation $\omega(q)$. The size of L in an alloy system may be viewed as the average size of the ordered domains which are embedded in the configurational-disordered matrix. According to the model, as L gets smaller Δq becomes larger: a wider range of frequencies are allowed to participate in the Raman scattering, and as a result the Raman lineshape exhibits a change. The lineshape-change depends on the phonon dispersion curve $\omega(q)$; for a curve of negative slope the line asymmetry is toward lower frequencies and for a positive slope the asymmetry is toward higher frequencies. The peak position also shifts accordingly. However, the position is a function of the alloy-mode as well: an alloy can be categorized as being a one- or two- mode type [14-15] and the behavior of the peak position depends on the type. The deconvolution of the peak position is left to a future investigation; at present we address merely the origin of the asymmetric lineshape and line broadening.

The Raman intensity $I(\omega)$ for the spatial correlation model may be expressed as [1, 12-13]

$$I(\omega) \propto \int \exp\left(\frac{-q^2 L^2}{4}\right) \times \frac{d^3 q}{[\omega - \omega(q)]^2 + \left(\frac{\Gamma_0}{2}\right)^2} \quad (1)$$

where q is in units of $2\pi/a$, a is the lattice constant, and Γ_0 is the linewidth of the material of composition $x=0$ which is GaN in this study. Our GaN films exhibit linewidth in the range 3 - 5 cm^{-1} depending on the film quality [8]. For the calculations we used the upper range value to account for the stress in the alloy which was inferred from the appearance of cracks in the films. In the calculation we assumed a spherical correlation domain and BZ.

To evaluate Equation 1 we fitted the phonon dispersion curves, which have been calculated by Azuhata et al [16], in the vicinity of BZ center. In their calculations the E2 mode along the Δ direction exhibits a doubly degenerate behavior and is a weak function of q , thus having no effect on the line broadening mechanism. In contrast, the E2 curves along the Σ and T directions both split into a lower and an upper branch, where the former is a decreasing function of q and the latter is an increasing function; these curves are expected to influence the Raman lineshape. Our calculations of Eq. 1 best concur with the phonon dispersion curve of the form: $\omega(q) = A + Bq^2$ (in units of cm^{-1} and with $A=568$ and $B=100$) which is the approximated behavior of the upper branch of the Σ and T curves in the vicinity of the zone center. However, when we included the contribution to the lineshape arising from the lower branches of the dispersion curves the fit was not ideal. Similar behavior has been previously observed in the calculation of BN lineshape [12]. The reason for the dominance affect of the upper branches in our calculations is under investigation.

The calculated lines and the Raman data for samples of composition 0.12 and 0.22 are presented in Figure 1. As depicted in the figure the asymmetric Raman data concur with the spatial correlation model, where the small deviation $\sim 560 \text{ cm}^{-1}$ may be attributed to the activated $A_1(\text{LO})$ mode. The ordered domain size, L , was determined from our calculations to be $\sim 25 - 35 \text{ \AA}$; a relatively small value suggesting the lack of a long range order in the alloy system. In order to further investigate this hypothesis a film of composition $x=0.22$ was characterized by XRD: the scan is presented in Figure 2. The figure shows the diffraction peak of the (0002) planes of the AlGa_N (superimposed is also the SiC substrate peak) and the inset presents the weak (0001) diffraction peak. The (0001) is a forbidden reflection in the WZ structure and appears as a superlattice line only when lattice ordering exists [17]; the intensity ratio (0001)/(0002) is a measure of the extent of the order [18]. Al_xGa_{1-x}N films which were grown by molecular beam epitaxy have been reported by Korakakis et al [17] to exhibit a long range order; the intensity ratio of their XRD lines is ~ 0.05 in contrast to our much smaller intensity ratio of ~ 0.002 . Thus the

XRD confirms the Raman analysis, indicating that the alloys in this study do not exhibit significant long range ordering.

More insight into the alloy micro-structure may be obtained from the Raman linewidth behavior. Figure 3 presents the Raman linewidth of the E2 mode as a function of the composition. The linewidth behavior follows a pattern which exhibits a maximum at composition $x \approx 0.5$, a value at which a maximum disorder should be expected in a random system. The solid line in the figure was calculated (in arbitrary units) using the relation for the entropy of mixing which is a measure of the configurational disorder in a random alloy [19]. Thus our data suggest that the distribution of the alloy constituents for the most part is random. The issue of randomness in $A_xB_{1-x}C$ alloys has been previously addressed and it was suggested that the anions, C, are periodically distributed in their sub-lattice sites while the cations, A and B, are randomly distributed in the other sub-lattice [2, 20]. However, achieving an ordered alloy in some families of ternary tetrahedral semiconductors has been demonstrated to be a function of the growth temperature [20]; the conditions for the ordered state in the $Al_xGa_{1-x}N$ system have yet to be explored.

To conclude, the asymmetric behavior of the E2 Raman linewidth of $Al_xGa_{1-x}N$ alloys was attributed to the activation of phonons of $q \geq 0$ arising from the disordered state of the alloys. X-ray diffraction supports the finding; the superlattice relative line-intensity is weak. The line broadening of the E2 Raman mode exhibits a maximum at composition $x \approx 0.5$ which is consistent with a random distributed system.

ACKNOWLEDGMENTS

We acknowledge the National Research Council, the Army Research Office, and the Office of Naval Research for supporting this research.

REFERENCES

1. P. Parayanthal, and F.H. Pollak, Phys. Rev. Lett. **52**, 1822 (1984).
2. I. Sela, V.V. Gridin, R. Beserman, R. Sarfaty, D. Fekete, and H. Morkoc, J. Appl. Phys. **63**, 966 (1988).
3. R.K. Chang, B. Lacina, and P.S. Pershan, Phys. Rev. Lett. **17**, 755 (1966).
4. B. Jusserand, and J. Sapriei, Phys. Rev. **B24**, 7194 (1981).
5. O. Brafman, I.F. Chang, G. Lengyel, and S.S. Mitra, Phys. Rev. Lett. **19**, 1120 (1967).
6. *Topics in Applied Physics-Light Scattering in Solids I*, Edited by M. Cardona, (Springer-Verlag, New York, 1983).
7. C. A. Arguello, D.L. Rousseau, and S.P.S. Porto, Phys. Rev. **181**, 1351 (1969).
8. L. Bergman, M.D. Bremser, J.A. Christman, S.W. King, R.F. Davis, and R.J. Nemanich, Mat. Res. Soc. Symp. Proc. **449**, 725 (1997).
9. M.D. Bremser, W.G. Perry, N.V. Edwards, T. Zheleva, N. Parkin, D.E. Aspnes, and R.F. Davis, Mat. Res. Soc. Symp. Proc. **395**, 195 (1995).
10. C.M. Balkas, Z. Sitar, T. Zheleva, L. Bergman, I.K. Shmagin, J.F. Muth, R. Kolbas, R.J. Nemanich, and R.F. Davis, Mat. Res. Soc. Symp. Proc. **449**, 41 (1997).
11. D.D. Manchon, A.S. Baker, P.J. Dean, and R.B. Zetterstorm, Sol. Stat. Commu. **8**, 1227 (1970).
12. R.J. Nemanich, S.A. Solin, and R.M. Martin, Phys. Rev. **B23**, 6348 (1981).
13. P.M. Fauchet, and I.H. Campbell, Critical Reviews in Solid State and Materials Science **14**, S79 (1988).
14. K. Hayashi, K. Itoh, N. Sawaki, and I. Akasaki, Sol. Stat. Commu. **77**, 115 (1991).
15. L. Bergman, and R.J. Nemanich, Annu. Rev. Mater. Sci. **26**, 551 (1996), (and references within).
16. T. Azuhata, T. Matsunaga, K. Shimada, K. Yoshida, T. Sota, K. Suzuki, and S. Nakamura, Physica **B219/220**, 493 (1996).

17. D. Korakakis, H.M. Ng, K.F. Ludwig Jr., and T.D. Moustakas, Mat. Res. Soc. Symp. Proc. **449**, 233 (1997).
18. B.D. Cullity, *Elements of X-Ray Diffraction*, (Addison-Wesley, Menlo Park, 1978).
19. D. Gaskell, *Introduction to Metallurgical Thermodynamics*, (Hemisphere Publishing Corporation, New York, 1981).
20. A. Zunger, Appl. Phys. Lett. **50**, 164 (1987).

FIGURE CAPTIONS

Figure 1. The RT Raman spectra of the E2 mode of $\text{Al}_x\text{Ga}_{1-x}\text{N}$ films of composition $x=0.06$, 0.12, 0.22 and 0.70. The respective linewidths are: 8, 13, 16, and 19 cm^{-1} , and peak positions at: 567, 569, 572, 579 cm^{-1} . The solid lines superimposed on the spectra of films: $x=0.12$ and 0.22 were calculated from the spatial correlation model presented in Eq. 1.

Figure 2. The (0002) X-ray diffraction of $\text{Al}_{0.22}\text{Ga}_{0.78}\text{N}$; the scan displays the SiC substrate peak. The inset to the figure shows the very weak (0001) superlattice line.

Figure 3. The E2 Raman linewidth as a function of composition (dots). The solid line is obtained from calculations of the entropy of mixing of an alloy system (in arbitrary units).

